

Modelling point defects and laser-induced defect processes in CsBr/Cu photocathodes

Matthew Thomas Egan Halliday

A dissertation submitted in partial fulfillment
of the requirements for the degree of
Doctor of Philosophy
of
University College London.

Department of Physics
University College London

March 15, 2016

I, Matthew Thomas Egan Halliday, confirm that the work presented in this thesis is my own. Where information has been derived from other sources, I confirm that this has been indicated in the work.

Abstract

This thesis presents calculations of defects in CsBr, models of photodesorption from CsBr films grown on insulating and metal substrates and work functions shift phenomena in CsBr/Cu films as modelled using density functional theory (DFT) methods. These results offer new insights into the mechanisms of activation and degradation of CsBr/Cu photocathodes.

The geometry, electronic structure, diffusion characteristics and optical properties of vacancies, interstitials, trapped holes and self-trapped excitons in bulk CsBr and at CsBr surfaces have been modelled. The calculated migration barriers and optical absorption spectra have been compared with experimental measurements.

A model of hyperthermal and thermal desorption is presented in order to explain the laser-induced Br desorption from α -CsBr(110) and β -CsBr(100) surfaces grown on LiF and KBr substrates. Hyperthermal desorption results from surface exciton relaxation. Excitons created in the bulk can separate into F-H pairs, and the subsequent diffusion of H-centres to the surface is responsible for thermal desorption.

The model of laser-induced Br desorption is extended to β -CsBr(100)/Cu. Experimental data is explained by a model of trapping at the surface of electrons photoemitted from the metal substrate, leading to an attenuation of surface exciton energies. The electron trapping characteristics of low-coordinated sites at the surface are analysed, including corner, kink, and divacancy sites. A model of cation desorption via Franck-Hertz excitation of F-centres is presented. The quenching of divacancy diffusion by trapped electrons results in a dramatically different surface evolution of irradiated CsBr/LiF and CsBr/Cu.

Finally, the shift of the work function of Cu after the application of CsBr films is examined, and the mechanisms by which this takes place. Particular attention is paid to the creation of vacancies and vacancy aggregates at the CsBr/Cu interface as the source of the phenomenon of photocathode “activation”.

Acknowledgements

I would like to thank Prof Alexander Shluger for his guidance, as well as Prof Wayne Hess, Dr Matthew Watkins, Dr Matthew Wolf for their assistance and many illuminating discussions. I would like to thank my parents for their patience and support, as well as Rebecca Tamas for support, patience and absorbing the emotional freight that has accompanied work on this study.

List of Publications

The following publications have been derived from work presented in this thesis:

1. M. T. E. Halliday, A. G. Joly, W. P. Hess, P. V. Sushko, A. L. Shluger, "Mechanisms of Photodesorption of Br atoms from CsBr Surfaces", *J. Phys. Chem. C*, **117**, 13502 (2013).
2. M. T. E. Halliday, W. P. Hess, A. L. Shluger, "Structure and properties of electronic and hole centres in CsBr from theoretical calculations", *J. Phys. Condens. Matter*, **27**, 245501 (2015).
3. M. T. E. Halliday, A. G. Joly, W. P. Hess, A. L. Shluger, "Photoinduced Br desorption from CsBr thin films grown on Cu(100)", *J. Phys. Chem. C*, **119**, 24036 (2015)
4. M. T. E. Halliday, W. P. Hess, A. L. Shluger "A mechanism of Cu work function reduction in CsBr/Cu photocathodes", *Phys. Chem. Chem. Phys.*, **18**, 7427 (2016).

Contents

1	Introduction	20
1.1	Photocathodes	20
1.2	Aims of this thesis	24
1.3	Overview of Thesis	26
2	Methodology	28
2.1	Electronic Structure Methodology	29
2.1.1	The Born-Oppenheimer Approximation	29
2.1.2	Hartree-Fock Methods	30
2.1.3	Density Functional Theory	33
2.1.4	Hybrid Functionals	37
2.1.5	Basis Sets and Pseudopotentials	39
2.1.6	Auxiliary Density Matrix Methods	40
2.1.7	Time-Dependent Density Functional Theory	42
2.1.8	Semi-empirical Dispersion Correction	45
2.2	Nudged Elastic Band Methods	46
2.3	Defect Models	47
2.3.1	Periodic Boundary Conditions	47
2.3.2	Embedded Cluster Methods	48
3	Modelling bulk CsBr and CsBr surfaces	53
3.1	Introduction	53
3.2	Results	55
3.2.1	Modelling Bulk CsBr	55
3.2.2	Van der Waals Forces	59
3.2.3	Topology of CsBr Grown on LiF, KBr and Cu Substrates	61
3.3	Discussion	63

4	Theoretical Modelling of Point Defects in CsBr	64
4.1	Introduction	64
4.2	Modelling Bulk α -CsBr: Embedded Cluster Approach	66
4.3	Defects in CsBr: Geometry	68
4.3.1	F-centres	68
4.3.2	V_k -centres	71
4.3.3	H- and I-centres	73
4.3.4	Self-trapped Exciton	73
4.4	Defects in CsBr: Migration	75
4.4.1	F-centres	76
4.4.2	V_k -centres	77
4.4.3	H- and I-centres	77
4.5	Defects in CsBr: Optical Properties	78
4.5.1	F-centres	78
4.5.2	V_k -centres	80
4.5.3	H- and I-centres	80
4.6	Discussion	81
5	Thermal and Hyperthermal Desorption from α-CsBr(110) and β-CsBr(100) Surfaces	86
5.1	Introduction	86
5.2	Experimental Methodology and Results	88
5.3	Methodology	92
5.4	Results	94
5.4.1	Hyperthermal Desorption	94
5.4.2	Thermal Desorption	99
5.5	Discussion	102
6	Desorption from CsBr/Cu films: Trapped Electrons, Holes and Excitons	104
6.1	Introduction	104
6.2	Experimental Methodology and Results	105
6.3	Methodology	109
6.4	Results	111

6.4.1	Excitons at the $\beta(100)$ Surface	113
6.4.2	Cation Desorption and the Franck-Hertz Effect	115
6.4.3	Alternative Br Desorption Pathways	117
6.4.4	Excitons and Charge at the $\beta(100)$ Surface	118
6.4.5	Electron Trapping Sites at $\beta(100)$ Surface	120
6.4.6	Evolution of the Irradiated $\beta(100)$ Surface	126
6.5	Discussion	127
7	CsBr films and their effect on the work function of Cu	132
7.1	Introduction	132
7.2	Experimental Background	134
7.3	Methodology	136
7.4	Results	138
7.4.1	CsBr Films and Reduction the Cu Work Function	138
7.4.2	CsBr Films of Partial Coverage	142
7.4.3	Mechanisms of Laser Activation	144
7.5	Discussion	153
8	General Conclusions	157
	Bibliography	160

List of Figures

1.1	An illustration on the nanoscale of the structural and point defects which will be present in CsBr/Cu photocathodes during operation, and points of interaction of incoming photons.	25
2.1	Regions 1, 2A and 2B of the embedding scheme.	49
2.2	The variation of on-site electrostatic potential on the anions as a function of distance from the centre of the nanocluster, for nanoclusters with eliminated moments up unto $l = 2, 3$ and 4 . $l = 1$ corresponds to the dipole moments, $l = 2$ to the quadrupole moments and so on. The nanocluster is constructed with $(2k + 1)^3$ unit cells.	51
3.1	A schematic of the ground state and excited state potential energy surfaces. The exciton energy, E_{ex} , and luminescence energy, E_L , are both estimated as vertical transitions (i.e. instantaneous) from one potential energy surface to the other.	57
3.2	AFM images of (a) 15 \AA films showing island type growth, containing both rectangular terraces and stripe-like formation running in the (110) direction and (b) 150 \AA films homogenously stripe-like terraces in the (110) direction. Images taken from Ref[1]. Copyright of Elsevier. . . .	62
3.3	The phase diagram of the CsBr film as a function of the substrate temperature during the growth. Figure taken from Ref[2]. Copyright of IoP.	62
4.1	The CsCl-type structure and NaCl-type structures, α - and β -CsBr, respectively.	65

- 4.2 The partitioning of the nanocluster into different regions and the $\text{Cs}_{32}\text{Br}_{31}$ cluster with interface ions. Note that the relatively small radius of the interface cations is drawn to aid the eye rather than to reflect physical difference in ionic radius. 67
- 4.3 The $\text{Cs}_{32}\text{Br}_{31}$ and $\text{Cs}_{40}\text{Br}_{38}$ clusters shown from all non-identical projections. The figure above depicts the x-y and x-z (which is identical to the y-z) planes of the $\text{Cs}_{32}\text{Br}_{31}$ cluster. The figure below depicts the x-y, x-z, and y-z planes of the $\text{Cs}_{40}\text{Br}_{38}$ cluster. Note that the anions and cations are sitting in mutually exclusive planes. Anions are depicted in red, cations in blue. 69
- 4.4 A plot of the spin density distribution of an F^0 -centre. The isosurface is set to a value of 0.001. The arrows on the diagram indicate movement direction of the ions in the case of an F^- centre, where the length of the arrow is approximately proportional to the magnitude of displacement. For the F^+ -centre directions of displacement are reversed. Br anions are depicted in red, and Cs cations in blue. 70
- 4.5 The local geometry of (a) the V_k - (b) H- and (c) I-centres. The magnitude of displacement is proportional to the length of the arrows. Cs cations are depicted in blue, Br anions in red, and the defect Br anions in yellow. Note the figure displays two vertical planes containing Br anions, and a single plane containing Cs cations bisecting the two anionic planes. 72
- 4.6 The spin density (isosurface = 0.001) of an off-centre triplet exciton. The spin density increases from red to blue. The proto F-centre is on the right, with the lobes of the hole orbital visible on the adjacent proto H-centre. The Br anions are depicted in red, and the Cs cations in blue. Note the figure displays two vertical planes containing Br anions, and a single plane containing Cs cations bisecting the two anionic planes. . . 74
- 4.7 The local geometry of a) the F-centre, b) the V_k -centre, c) the H-centre and d) the I-centre at the the highest energy point along the diffusion trajectory (barrier point). The ions in yellow are those of the defect, with all other Br anions depicted in red, and the Cs cations in blue. . . . 76

- 4.8 The positions of the calculated one-electron (DFT) energy levels involved in the primary optical transitions associated with the peak in the optical absorption spectrum of each defect. The dashed lines indicate semi-localised states confined to the clusters as opposed to the idealised VBM and CBM of the infinite crystal. 78
- 4.9 The σ_g - σ_u transition of the H-centre electron, responsible for the largest peak in the H-centre optical absorption spectrum. The yellow and blue iso-surfaces represent positive and negative value of the wavefunction, respectively. The Br anions are depicted in red, and the Cs cations in blue. 80
- 4.10 The calculated optical absorption spectra for the clusters containing each defect. In the case of the F^- , F^+ , H- and I-centres, the 50 lowest energy optically allowed transitions have been calculated, up unto a maximum of 6.5 eV. In the case of the F^0 -centre, the 100 lowest energy transitions have been calculated. For the V_k -centre, the 150 lowest energy transitions have been calculated, as the peak in the experimental absorption spectrum of CsBr assigned to the defect at 3.23 eV, of σ polarisation, corresponded to the 128th lowest energy transition. 82
- 4.11 The optical absorption spectrum of liquid helium temperature CsBr after (a) 8 min of X-ray irradiation and (b) 1 min of X-ray irradiation. The red ticks on the x-axis mark the positions of the maxima of absorption for the defects as calculated in this study. Copyright of Elsevier, 1971[3]. 83
- 5.1 Experimental schematic of the apparatus for the desorption experiments conducted at Pacific Northwest National Laboratory (PNNL). . . 89
- 5.2 The distributions of the desorbed $Br(^2P_{3/2})$ atoms following 6.4 eV laser emission showing (a) the laser delay between pulse and probe and (b) the kinetic energy. The hyperthermal kinetic energy distributions peak at 0.33 and 0.27 eV on the KBr(100) and LiF(100) surfaces, respectively. The lines in the part (b) display Gaussian fits to the data. . 90

- 5.3 The distributions of the desorbed $\text{Br}(^2\text{P}_{3/2})$ atoms following 7.9 eV laser emission showing (a) the laser delay between pulse and probe and (b) the kinetic energy. The hyperthermal kinetic energy distributions peak at 0.34 and 0.25 eV on the $\text{KBr}(100)$ and $\text{LiF}(100)$ surfaces, respectively. The lines in the part (b) display Gaussian fits to the data. 91
- 5.4 Spin density iso-surfaces of the exciton on the $\alpha(110)$ surface. The orbital of the electron component is depicted in (a), with an iso-surface value of $0.001|e|$, and that of the hole component in (b), with an iso-surface value of $0.003|e|$. Note that the two plots are oriented towards the surface from mutually orthogonal directions. The cations are represented by large blue spheres, and the anions by smaller red spheres. 96
- 5.5 Two stages in the hyperthermal desorption process. Spin-density plots corresponding to (a) a surface triplet exciton localised on a surface Br site and (b) a surface F-centre and a desorbing neutral Br atom. 98
- 5.6 The mechanism by which interstitial Br atoms created by the relaxation of an exciton can transform into adsorbed Br atoms on the surface. In (a) the H-centre is in the second layer, where it feels a force in the direction of the surface. In (b) an anion has moved close to the second layer anion lattice position and the partner anion is displacing a surface anion from its lattice site. In (c) The H-centre is now in the surface layer and reorienting towards a lattice and adsorbed Br atom arrangement. Cations are depicted in blue, and anions in red. 100
- 5.7 A profile of a portion of the unit cells containing the defects, depicting (a) A Br atom adsorbed above a Br lattice site, and (b) an off-centre exciton arrangement at the surface. The spin density is displayed in yellow, and corresponds to an iso-surface of 0.001, with all Br anions depicted in red, and cations in blue. 101
- 6.1 Preliminary results of the velocity distribution of neutral $\text{Br}(^2\text{P}_{3/2})$ atoms after 4.7 eV irradiation of KBr/LiF and KBr/Cu films. Image provided courtesy of Prof. Wayne Hess and Dr. Alan Joly. 106

- 6.2 The velocity distributions of emitted neutral Br($^2P_{3/2}$) atoms after 4.7 eV irradiation of CsBr/Cu films of various thicknesses (see key). Image provided courtesy of Prof. Wayne Hess and Dr. Alan Joly. 107
- 6.3 Kinetic energy distribution functions for Br-atom emission from 77 nm-thick KBr films deposited on LiF (red circles) and a 12 nm-thick KBr film deposited on Cu (blue squares) and a 72 nm-thick KBr film deposited on Cu (green triangles) following 4.7 eV laser excitation. The nominal film thickness does not appreciably change the recorded kinetic energy distribution function. 108
- 6.4 AFM images of electron-irradiated KBr. On the left characteristic monatomic pits are clearly visible. On the right are displayed atomic resolution of various surface features, along with a schematic interpretation of the atomic structure. Copyright of Elsevier[4]. 109
- 6.5 a) A quadrant of Regions 1 and 2A and b) a cross-section of the two regions. Anions and cations in Region 1 are coloured red and blue, and in Region 2A yellow and green, respectively. Interface cations have been coloured black. The numbered anions indicate where charges have been modelled, with the consequent desorption energy in Table 6.2. Labels 6 and 7 index anions in the bulk. 110
- 6.6 Photons incident to CsBr/Cu, and the three distinct ways they can directly or indirectly contribute to the emitted Br($^2P_{3/2}$) distribution. Photons may, as (1), interact with surface sites creating excitons, may as (2), penetrate the films and induce photoemission of electrons from the Cu substrate, or as (3), create a hole at a surface site. 112
- 6.7 The exciton on the $\beta(100)$ surface. The charge density isosurfaces (value = 0.01) of the electron from (a) above and (b) adjacent to the surface, and the hole (c) above and (d) adjacent to the surface. Anions are depicted in red, and cations in blue. 114
- 6.8 The adiabatic potential energy surface (APES) of the Cs atom in perpendicular to the surface from (a) a terrace site (b) a site adjacent to an F-centre and (c) a site adjacent to an F* centre. 116

- 6.9 A schematic of the potential energy surfaces with and without an electron (above and below, respectively). 121
- 6.10 The iso-surfaces of the HOMO of (a) an F-centre (b) an F^- -centre (c) a divacancy and (d) a divacancy with a trapped electron. The geometric relaxation is given with respect to the defectless surface for (c), and with respect to the neutral defects (i.e. (a) and (c), respectively) for (b) and (d), with the length of the arrow corresponding approximately to the magnitude of displacement in the directions indicated. 123
- 6.11 The HOMO iso-surface = 0.001 for the trivacancy and quadvacancy with trapped electrons, where displacements are given with respect to the relaxed ionic coordinates in the neutral state. The length of the arrows are approximately proportional to the displacements. 124
- 6.12 Geometries of the clusters used in order to model low-coordinated sites. In (a) a nanocorner sites has been modelled, such that one side of the Region 1 cube is displayed on the right. Parts (b), (c) and (d) are step, kink and internal corner sites respectively. On the left is depicted the top layer of the terrace with the additional ions on top. On the right is displayed the additional ions only, from directly above the surface. . . . 125
- 6.13 The geometry of (a) an electron trapped at a nanocorner and (b) an electron trapped at a kink site. The spin density iso-surfaces have been included, where the surfaces correspond to values of 0.001 and 0.003 for the nanocorner and kink sites, respectively. Displacements are given with respect to the geometry of the uncharged structural defects. . . . 126
- 6.14 The geometry of (a) a divacancy (b) the barrier point to divacancy migration and the geometry and spin density diagram of (c) a divacancy with an electron (d) a divacancy with an electron at the barrier point. Anions are depicted in red, and cations in blue. Spin density iso-surfaces of a value of 0.001 are also shown in the negatively charged cases. 128

- 6.15 Desorption following irradiation of CsBr films on insulating and metal substrates (below and above, respectively.), including a snapshot of the morphology of the surface during irradiation, and resultant Br kinetic energy distributions. 129
- 7.1 The variation of the logarithm of QE with time during irradiation with 4.66 eV light. The quantum efficiency of bare Cu is included for reference. Copyright of AIP publishing[5]. 135
- 7.2 Relative depletion of Cs and Br after LA for films of various thicknesses. Copyright of AIP publishing[5]. 135
- 7.3 The 1D-averaged electrostatic potential across the CsBr(2ML)/Cu slab, where z denotes the displacement in the z -direction and the electrostatic potential is on the y -axis given in units of Hartrees per the charge of an electron. The work function is estimated as the difference in the potential at the minimum and maximum values of z 138
- 7.4 The calculated DOS for the Cu(100) surface is displayed on the left, with the experimental XPS density of states inset on the right. Copyright of Elsevier[6]. 139
- 7.5 The unit cell of CsBr(2ML)/Cu(100). The Cs ions are depicted in blue, Br ions in red, and Cu ions in green. 140
- 7.6 The variation of the work function shift for 4ML films as a function of interfacial separation. 141
- 7.7 The geometry of 24-, 40- and 72-atom 2ML clusters of β -CsBr, from top descending, corresponding to coverages of 21%, 36% and 75%, respectively. 143
- 7.8 The local geometry of an anion vacancy at the interface, with the nearest neighbour displacements, where the length of the arrow is approximately proportional to the magnitude of displacement. Anions are red, cations blue, and the Cu ions depicted in green. 146
- 7.9 All unique combinations of two F-centres at the interface in the unit cell. F-centres have been modelled at site 1 and 2, 3 and 4. 147

- 7.10 The local geometry of a) a cation vacancy and b) a divacancy at the interface, with the nearest neighbour displacements, where the length of the arrow is approximately proportional to the magnitude of displacement. 149
- 7.11 The diffusion of a divacancy. The top of the figure shows a) the initial b) saddle point and c) final state towards motion via Cs motion. The bottom shows a) the initial b) saddle point and c) final state via Br motion. Anions are depicted in red, and cations in blue. 150
- 7.12 The geometry of relaxed 4ML CsBr clusters of 21% and 75% coverage on the Cu(100) surface. 152
- 7.13 The proposed mechanism corresponding to laser activation of the photocathode. 155

List of Tables

3.1	The lattice parameter(a_0) and band gap of CsBr in CRYSTAL09 as calculated by each functional. The number given in brackets after the functional name indicates the fraction of HF exchange energy.	56
3.2	The lattice parameter and band gap of CsBr in CP2K as calculated by each functional. The number given in brackets after the functional name indicates the fraction of HF exchange energy.	56
3.3	The calculated lattice parameter of both α - and β -CsBr with the D2 and D3 descriptions, and the calculated values in the absence of any dispersion correction.	60
3.4	The effect of including dispersion forces on the cohesive energy of both α - and β -CsBr.	60
4.1	The total displacements of the nearest neighbour Br anions (A) and Cs cations (B) with respect to their perfect lattice sites as a result of F-centre formation. Directions of displacements are indicated in Figure 4.4. The positions of the defects states within the band gap are given with respect to the CBM.	71
4.2	The displacements of the nearest neighbour Cs cations and Br anions with respect to their perfect lattice sites as a result of the defects. The direction of displacements are indicated in Figure 4.5. The label r_e refers to the intermolecular separation of the Br_2^- molecular ion, or the Br_3^- ions in the case of the I-centre, and a_0 to the lattice parameter. . . .	72
4.3	The calculated energies of optical absorption peaks (OA_{calc}), experimental absorption peaks (OA_{exp}) and migration barriers (E_a) associated with the primary defects.	79

5.1	The calculated and experimental values of various properties in both α - and β -CsBr in the CRYSTAL09 model. a_0 denotes the lattice parameter; E_g the band gap; E_{VB} the valence band width; E_{coh} the cohesive energy; and ϵ_∞ the high-frequency dielectric constant.	93
5.2	The calculated and experimental values for the EA and IPs of a Br atom using the pseudopotentials and basis sets used throughout the study and the B3LYP functional with varying amounts of HF exchange energy. . .	94
5.3	The calculated exciton energies, surface F-centre formation energies, and maximum kinetic energies for both surfaces. All energies are given in eV.	98
6.1	The calculated energy available for desorption from the $\alpha(110)$ and $\beta(100)$ surfaces for each model.	114
6.2	The energy available for hyperthermally desorbing Br atoms (E_{des}) in the presence of negative charges placed at the positions indicated in Fig. 6.5, and the corresponding distances between the charges and excitons (r).	119
6.3	The results for the calculated EA, IP and ΔE of each trapping site, where a positive number for ΔE indicates that the system with an extra electron is of lower energy than without the electron. The energies are defined in Figure 6.9.	121
6.4	The calculated EA and IP of the unrelaxed and relaxed geometries for the low-coordinated clusters, and the difference in height of the potential wells with and without an electron.	124
7.1	The change in the work function as a function of thickness of CsBr film, where d represents the interfacial separation and $\Delta\phi$ the reduction of the work function in eV.	140
7.2	The change in the work function as a function of thickness of CsBr film with the inclusion of van der Waals forces, where d represents the interfacial separation, and $\Delta\phi$ the reduction of the work function. . . .	141

- 7.3 The change in the work function as a function of CsBr cluster size and molecular layers. All energies are in eV. The work function of bare Cu is calculated as 4.53 eV. 144
- 7.4 The calculated formation energy (E_{Form}) of an F-centre in different layers of the deposited CsBr, where 1 represents the layer at the interface, 2 the 2nd layer from the interface and so forth, with the corresponding shift of the work function ($\Delta\phi$). Formation energies have been calculated with reference to a Br atom, as specified in the text. All energies are in eV. 145
- 7.5 The calculated formation energy (E_{Form}) of a pair of F-centres, where the positions are indicated in Figure 7.9, with position 1 always a vacant site. The corresponding shift of the work function ($\Delta\phi$) is in the column on the right. 147
- 7.6 The formation energies (E_{Form}) of F-centres at positions at the interface, and their corresponding change in the work function ($\Delta\phi$) with respect to the bare Cu(100) surface. All energies are in eV. 153

Chapter 1

Introduction

1.1 Photocathodes

Photocathodes are negatively-charged electrodes constructed of photosensitive compounds that emit electrons when exposed to electromagnetic radiation. They have applications ranging from components in solar cells[7], as scintillators used in particle accelerators or radiation detectors[8] and in medical diagnosis[9]. Photocathodes function on the principle of the photoelectric effect, where photons incident on a surface induce electron emission, the discovery of which established one of the key pieces of evidence of the particle-like behaviour of light[10], laying the foundations of modern quantum theory.

In addition to their employment as photon detectors, photocathodes are also used as a source of electrons. Of particular significance to the research undertaken in this thesis is their function in particle accelerators such as at the Stanford Linear Accelerator (SLAC), where electrons are accelerated up to energies of 50 GeV before colliding with a stationary target, so as to create exotic particles and probe the frontiers of particle physics. Research at SLAC has led to the discovery of the quark structure of nature[11, 12], the discovery of the tau lepton[13] and the charm quark[14].

Bremsstrahlung radiation is emitted as a byproduct of the acceleration of charged particles moving in an electric or magnetic field. Although initially regarded as undesirable in particle accelerators, due to loss of energy from accelerating particles, synchrotron radiation, radiation resulting from radial acceleration, has been identified as a source of light with many useful properties, such as containing a broad spectrum of wavelengths, being highly collimated and being of very high intensity. These properties

led to the foundation of particle accelerators whose sole purpose was to provide synchrotron radiation for secondary research purposes. By modulating the electron density of the bunch accelerating in the synchrotron, coherent light can be achieved, such that they are referred to as free electron lasers (FELs).

In the present day FELs produce high intensity tunable sources of light of wavelengths ranging from microwaves to X-rays. They have applications in many diverse fields, including the imaging of single-molecule thick proteins[15], neurosurgery[16], and the creation of nanomaterials for use in quantum computers[17]. At the time of writing, the Linac Coherent Light Source (LCLS) at SLAC is the worlds most powerful X-ray FEL, which manages to achieve a brightness approximately 10^9 times larger than traditional synchrotron sources, with a time-resolution on the femtosecond level[18]. FEL X-ray light sources require electron injectors with a high repetition rate, high brightness, low emittance and long lifetime. Their development is a key challenge and high priority in the accelerator community. In particular, a more efficient and robust electron source would greatly decrease the energy costs of such facilities, and reduce the operational downtime while degraded photocathodes are replaced.

Photocathodes have the advantage over thermal cathodes of generating a low emittance, short pulse beam and having a relatively high QE[19]. The photocathode currently in operation at the LCLS radio frequency gun is constructed of copper. Copper has the advantages of being both robust and emitting electrons with small momentum perpendicular to the beam direction. Despite this, the quantum efficiency (QE), a measure of electrons ejected per incident photon, is very small. Various different materials have been proposed as a suitable replacement of copper, in both the LCLS and in other XFELs.

Among suggested candidates are the family of negative electron affinity (NEA) photocathodes, composed of semiconductor materials constructed of various combinations of III-IV-V elements, many of which have been previously used as photon detectors, due to their wide range of electromagnetic sensitivity. In particular GaN has been investigated[20, 21, 22], as well as InGaAs[23, 24] and GaAs[25, 26, 27]. All have very high QE, in particular GaN which has been shown to have a QE of $\geq 50\%$ in the high UV range[28], and low thermal emittance, but their fragility and poor projected lifetimes, both due to degradation after irradiation and high reactivity when in contact

with the atmosphere, has limited further research into these materials for heavy use such as at the LCLS. The NEA photocathodes lack the robustness of the original Cu photocathode.

Other candidate photocathodes are made of compound semiconductors in combination with caesium, such as GaAs:Cs[29], Cs₂Te [30, 31, 32], Cs-K-Te[33, 34], CsSb[35], Cs₃Sb[36] and K₂CsSb[37]. These materials have a high sensitivity to low wavelengths, making them a particularly favourable choice from a low energy cost perspective. The use of Cs is motivated by the fact that Cs has the lowest work function and ionisation potential of any naturally occurring element (2.14 eV)[38], however pure Cs is highly reactive and prone to contamination. The low affinity of the valence 6s electron encourages donation of the electron to the metal, creating a dipole across the surface which lowers the work function of the compound material[39, 40]. The common weakness of all these potential candidates is their relatively quick degeneration and limited lifetime with respect to, for example, bare Cu, and their reactivity with oxygen, moisture and other atmospheric contaminants[41].

Alkali halide film coatings applied to Cu have been proposed in order to remedy the deficiencies of existing photocathodes, acting as a protective layer from both radiation and the atmosphere. An effective coating film must be both sufficiently thick and chemically stable in order to perform its protective function, and have sufficiently good electron and photon transport properties such that interference with electron photoemission is minimised. Early experiments with 150 Å thick NaI films coating Cs₃Sb photocathodes found that the films provided considerable protection against oxygen and dry air, although the decrease in quantum efficiency (QE) was of the order of 10-20[42].

Subsequent studies testing various different alkali halide films identified the caesium halides, in particular CsBr and CsI, as the most promising candidates for coating materials, due to both their protective characteristics and minor negative impact on QE[43, 44]. Absolute values of QE of around 6% (from an uncoated value of around 30%) have been achieved for CsBr/K-Cs-Sb photocathodes which show greatly improved protection under oxygen pressures of 150 Torr[45].

A study examining protective 280 Å thick CsBr films covering K-Cs-Sb photocathodes has hypothesized that the minimal reduction in QE may be partially explained

as a consequence of small lattice mismatch between the two compounds leading to a clean polycrystalline film[46]. It has been suggested that caesium halide films in general form cleaner films with larger crystals than other alkali halides grown by molecular beam epitaxial techniques. Where STM and AFM images of NaI, CsI and CsBr films grown on an inert CaF_2 substrate are available, the caesium halide films are cleaner than NaI[47], leading to less penetration of water into the films which ultimately hinders the transport properties and consequently QE of photocathodes.

As the effectiveness of CsBr films as a protective layer has become established, further research has observed that the films may counter-intuitively lead to an *increase* in QE when coating particularly favourable substrate photocathode materials. When CsBr is deposited on Cr, the QE is observed to decrease but to a considerably lesser extent than expected for 15 nm films[48]. These results have been partially explained by the posited existence of intra-band-gap absorption sites (IBASs) which have a fluorescence signature at 3.8 eV[49]. Although it has been suggested that these IBASs are due to the presence of colour centres (vacancies with or without electrons), there remains little experimental or theoretical evidence to substantiate this claim. CsBr/GaN films have been shown to have a photoyield four times larger again than CsBr/Cr films[50], although their utility is limited due to the rise in temperature as a consequence of efficient photon absorption. CsBr/Nb films can lead to increases of the order of 800 times with respect to that of bare Nb[51], although again their fragility precludes their uses in XFELs.

CsBr/Cu films have been measured to increase the QE of photocathodes with respect to bare Cu by factors of up to 50[52]. As well as an initial step change in QE observed after film deposition, a further increase in QE is observed after a period of irradiation[53, 54, 55, 56]. Studies into the efficacy of such photocathodes confirm their robustness with respect to the atmosphere[57] and measure sufficiently small transverse emittance[58]. CsBr/Cu films have emerged as the prime candidate for next-generation photocathodes in XFELs such as the LCLS, due to being both more efficient in harvesting electrons as a function of laser fluence and having a longer operational lifetime and effective resistance to atmospheric contaminants.

Despite much evidence testifying to the advantages of CsBr/Cu photocathodes over those constructed from bare Cu, the fundamental mechanisms behind the increase

in QE remain unknown. So-called IBAS states have been suggested as playing a major role in photoemission although their nature remains speculative. In particular, the origin of the increase in QE after a so-called “activation” period of irradiation remains unknown. Tentative suggestions that the phenomenon is a consequence of defect behaviour have been made, although the long “activation” period (of the order of hours) would suggest that laser activation of photocathodes occurs due to complex processes. Finally how and to what extent CsBr and CsBr/Cu materials degrade after UV irradiation also remains unknown, although degradation has been observed and the introduction of CsBr films has been initially motivated by its radiation hardness.

Calculations of defects in bulk CsBr, excitation and irradiation of CsBr surfaces and defects in the compound CsBr/Cu systems can provide insight into the mechanisms by which radiation alters CsBr, how defects may be created, how defects will behave in the material, how CsBr/Cu films may degrade, and how exactly CsBr films counter-intuitively greatly increase the QE of Cu photocathodes. The research contained in this thesis has been conducted in order to provide answers to these questions, and improve scientific understanding of the functioning and evolution of photocathodes so as to inform their design.

1.2 Aims of this thesis

The aim of this thesis is to illuminate how CsBr films evolve and degrade under laser irradiation of various photon energies, on both insulating and metal substrates, and to examine the mechanisms by which CsBr films reduce the work function of bulk Cu, in order to add to scientific understanding of CsBr/Cu photocathodes.

Cu Photocathodes coated with thin CsBr films can function with relatively low energy photons which reduce the cost of their operation. The large increases in QE of Cu photocathodes with CsBr thin films is well documented, although the reasons for the improved efficiency remains poorly understood.

The range of reactions of photons incident on CsBr/Cu photocathodes is illustrated in Figure 1.1. Defects will be created in the bulk, on the CsBr surface and at the CsBr/Cu interface during irradiation. We also expect desorption of surface atoms by analogy with rocksalt alkali halides, although how a metal substrate effects atomic desorption is unclear. How exactly photoemitted electrons will interact with defects in

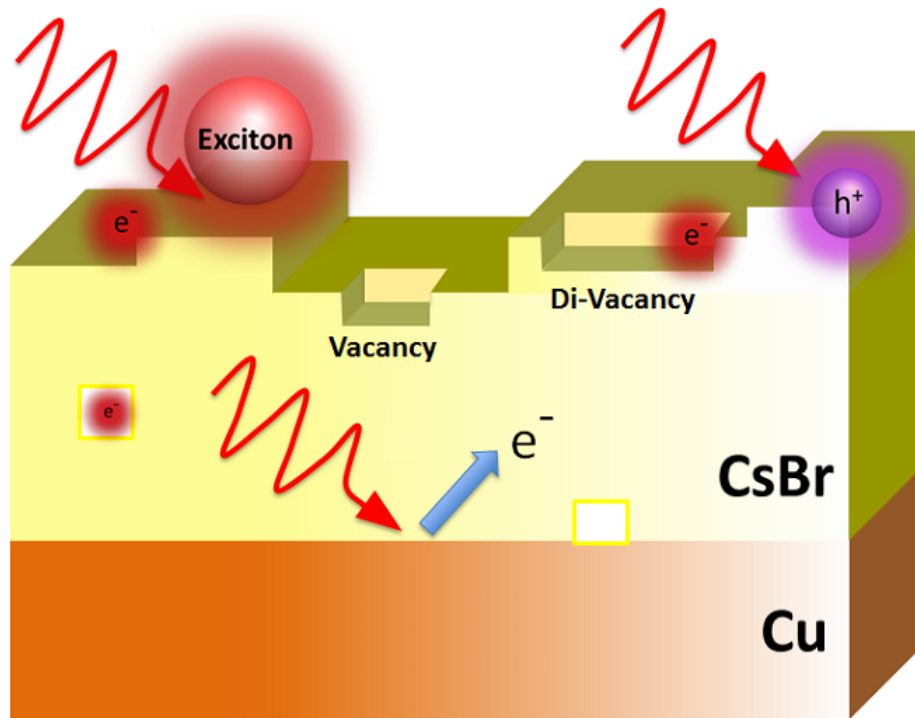


Figure 1.1: An illustration on the nanoscale of the structural and point defects which will be present in CsBr/Cu photocathodes during operation, and points of interaction of incoming photons.

the bulk and at the surface also remains unknown.

Calculations in this thesis go to some length to increasing scientific understanding of these phenomena. Point defects, including excitons, have been modelled in bulk CsBr. Models of desorption induced by 7.9 and 6.4 eV photons of the rocksalt alkali halides have been extended to the structurally different CsBr grown on insulating LiF and KBr substrates. This model is then extended to CsBr grown on a Cu substrate, where the metal is found to substantially alter both the desorption behaviour and the structural evolution of the film. A model of Cs desorption mediated by photoemitted electrons is outlined. Finally, the effect of CsBr films on the work function of Cu is examined, and a model explaining so-called laser activation in photocathodes by the creation and accretion of Br vacancies and divacancies at the interface is outlined. The theoretical work in this thesis has been conducted in parallel with experimental collaborators and sponsors at Pacific Northwest National Laboratory (PNNL), who are in turn funded by the US Department of Energy in order to conduct research towards the design of next-generation photocathodes. The following section outlines in detail the contents of each chapter of this thesis.

1.3 Overview of Thesis

Chapter 2 outlines the theoretical methods employed in this thesis, in particular density functional theory (DFT) from first principles, hybrid functionals and time-dependent DFT. One aim of this thesis is to examine the accuracy of these methods and critically assess their descriptions of the physical behaviour of the models by comparison with experimental measurements.

Chapter 3 compares and contrasts calculations from three different models of bulk α -CsBr in order to determine the effects on calculated properties of using different functionals, basis sets and the use of either periodic boundary conditions or embedding cluster methods. In particular, the effects of increasing the proportion of HF exchange in the standard formulation of functionals such as B3LYP and PBE0 is examined. The second half of the chapter reviews the experimental literature of MBE-grown CsBr films in order to make predictions of the structure and quality of CsBr films grown on the LiF(100), KBr(100) and Cu(100) surfaces.

Chapter 4 contains a summary of the geometry, electronic structure, diffusion behaviour and optical properties of the primary defects of CsBr, including vacancies, interstitials, trapped holes and excitons. Where available calculations have been compared with experiment, in particular the experimental optical absorption spectrum of X-ray irradiated CsBr is compared with calculated defect spectra. The aim of this chapter is to provide a summary of the basic characteristics of these defects both as a reference and as a preliminary step towards understanding the properties of these defects at surfaces and in thin films.

Chapter 5 contains calculations of the α -CsBr(110) and β (100) surfaces, and models excitons and vacancies at these surfaces. The aim of this chapter is to provide an insight into experimental results of Br desorption from CsBr films grown on LiF and KBr and irradiated with 6.4 and 7.9 eV UV radiation, and gain an understanding of the mechanisms of degradation of CsBr films grown on insulating substrates under UV irradiation. Mechanisms corresponding to experimentally observed “thermal” and “hyperthermal” desorption have been proposed.

Chapter 6 extends the calculations of Chapter 5 to UV irradiation of CsBr/Cu films, and explains the desorption distribution of Br atoms from CsBr/Cu films with a model of electron trapping at the surface, providing calculations of excitons in the

presence of charge and electrons trapped at low-coordinated sites to support the model. Also provided is a model of cation desorption via the Franck-Hertz effect. The aim of this chapter is to explain the experimentally observed change in the desorbed Br distribution, and to consequently gain understanding of how the evolution of CsBr films is affected by the presence of the metal.

Chapter 7 aims to gain insight into how the deposition of CsBr films affects the work function of the underlying Cu substrate, as a function of film thickness and coverage, and how van der Waals forces and defects at and around the interface affect the work function. A model of F-centre and divacancy aggregation is presented in order to explain how the QE of photocathodes increases after a prolonged period of irradiation, and how the atomic structure of the film is modified during operational function of photocathodes.

Finally, we critically assess the conclusions of the thesis with respect to the degree to which the aims have been fulfilled, and how the calculations contained herein can add to understanding of the efficacy of CsBr/Cu photocathodes, and explain their characteristics. A brief survey of future directions for research is outlined.

Chapter 2

Methodology

The aim of the following Chapter is to summarise the theoretical approaches used in this thesis to model point defects in crystalline materials with electronic structure methods, with particular attention to the various approaches to tackling the problem of solving the many-electron wavefunction.

Although quantum mechanics specifies how a Hamiltonian can be constructed for an atomic system, that is, a collection of protons and electrons, and yields explicit equations for the wavefunction of the system, these equations are in general not algebraically soluble. Moreover, solid state systems of interest typically contain thousands of particles, resulting in thousands of simultaneous equations of motion. As a result, a series of approximations have been applied in this thesis in order to make calculations of the electronic structure tractable.

The chapter begins by outlining the Born-Oppenheimer approximation[59], which is followed by brief descriptions of the fundamentals of Hartree-Fock theory and Density Functional Theory (DFT). Section 2.1.4 introduces hybrid functionals and is followed by a description of pseudopotentials and basis sets. Auxiliary Density Matrix Methods (ADMM), which have been used for some calculations in Chapters 6 and 7, are briefly described. Section 2.1.7 introduces Time-Dependent DFT (TD-DFT), an extension to DFT used to describe excited states. Section 2.1.8 describes semi-empirical corrections which are additively included in some DFT calculations in Chapters 6 and 7 in order to include a description of dispersion forces, followed by an outline of Nudged Elastic Band (NEB) methods, which have been used to estimate the barriers to migration of some defects. Finally, models which employ periodic boundary conditions and embedded cluster methods are introduced. Both approaches have been used to conduct

calculations in this thesis.

2.1 Electronic Structure Methodology

2.1.1 The Born-Oppenheimer Approximation

The problem of electronic structure methods begins with attempts to solve the non-relativistic time-independent Schrödinger equation:

$$\hat{H}|\Psi\rangle = E|\Psi\rangle, \quad (2.1)$$

where H is the Hamiltonian operator for a system of electrons and nuclei with position vectors r_i and R_A , respectively.

This Hamiltonian consists of five operators, which can be expressed as:

$$\hat{H} = (\hat{T}_n + \hat{T}_e + \hat{U}_{en} + \hat{U}_{ee} + \hat{U}_{nn}), \quad (2.2)$$

where the T and U refer to kinetic energy and potential energy, respectively, and the labels e and n indicate electronic and nuclear coordinates and their derivatives, respectively. The first and second terms are the kinetic energy of the atomic nuclei and electrons, respectively. The third term represents the attractive Coulombic interaction between electrons and nuclei, and the fourth and fifth terms the mutual interactions between the electrons and nuclei, respectively.

The Born-Oppenheimer approximation begins with the observation that electrons have a mass three orders of magnitude smaller than the nuclei. As such one can make the approximation that the electrons moving in a potential created by a nuclei are moving so much faster than the nuclei that the nuclei essentially remain fixed with respect to electronic motion, this is the so-called “clamped-nuclei” approximation. The total wavefunction can then be separated into electronic (Ψ_e) and nuclear (Ψ_n) components,

$$\Psi(\mathbf{r}, \mathbf{R}) \approx \Psi(\mathbf{r}; \mathbf{R}) = \Psi_e(\mathbf{r}; \mathbf{R})\Psi_n(\mathbf{R}), \quad (2.3)$$

where \mathbf{r} and \mathbf{R} refer to the coordinates of the electrons and nuclei, respectively, such that the electrons only depend parametrically on the nuclear coordinates (i.e. not explicitly), as they are conceived as responding to nuclei motion instantaneously, and

as the electrons have such a comparatively small mass, the following approximation is valid:

$$\hat{T}_n \Psi \approx \Psi_e(\hat{T}_n \Psi_n). \quad (2.4)$$

These approximations allow for a decoupling of the electronic and nucleonic wavefunctions, as:

$$(\hat{T}_e + \hat{U}_{ee} + \hat{U}_{en})\Psi_e(\mathbf{r}; \mathbf{R}) = E_e(\mathbf{R})\Psi_e(\mathbf{r}; \mathbf{R}) \quad (2.5)$$

$$(\hat{T}_n + \hat{U}_{nn} + E_e(\mathbf{R}))\Psi_n(\mathbf{R}) = E\Psi_n(\mathbf{R}). \quad (2.6)$$

The now separated electronic equation can be solved to get the energy of the electrons, $E_e(\mathbf{R})$, which depends on fixed nuclear coordinates.

Once the electronic solution has been found, attention can be turned to the nuclear equation, and $E_e(\mathbf{R})$ functions as the potential energy surface within which the nuclei move. As the electrons are much faster than the nuclei, the motion of the electrons can be approximated by a time-averaged charge distribution, such that the nuclei are conceived as moving in an electric field created by this smeared-out distribution. This is the so-called ‘‘mean-field’’ approximation. Thus the nuclear equation can be solved by incorporating the potential energy obtained from the solution of the electronic problem into the nuclear Hamiltonian.

In general, the quantum mechanical behaviour of the electrons is more significant than that of the nuclei in solids, and the solution of the electronic problem is of primary concern for the research undertaken in this thesis.

2.1.2 Hartree-Fock Methods

Hartree-Fock (HF) theory[60] is founded on the need to solve the Schrödinger equation for molecules which can involve a very large number of electrons. Although initially developed for molecules, it has been used successfully to describe the electronic structure of solids, and, with the advent of hybrid functionals, calculations using HF methods are routinely used in materials modelling research. For the sake of simplicity and brevity only restricted HF (RHF) theory shall be discussed here, (where there are

no unpaired orbitals), but all important results derived here also apply for unrestricted HF (UHF) calculations.

The first approximation in HF theory is that the electronic wavefunction can be approximated as the product of single-electron functions (orbitals), each of which do not explicitly depend on the motion of the other electrons. As electrons are fermions, the wavefunction describing them must be antisymmetric by the Pauli exclusion principle. One simple way to construct a wavefunction that satisfies such a condition is by using a Slater determinant[61], which is defined for a set of N electrons as:

$$\Psi_{\text{SD}}(\mathbf{x}_1, \mathbf{x}_2, \dots, \mathbf{x}_N) = \frac{1}{N!} \begin{vmatrix} \psi_1(\mathbf{x}_1) & \psi_2(\mathbf{x}_1) & \cdots & \psi_N(\mathbf{x}_1) \\ \psi_1(\mathbf{x}_2) & \psi_2(\mathbf{x}_2) & \cdots & \psi_N(\mathbf{x}_2) \\ \vdots & \vdots & \ddots & \vdots \\ \psi_1(\mathbf{x}_N) & \psi_2(\mathbf{x}_N) & \cdots & \psi_N(\mathbf{x}_N) \end{vmatrix} \quad (2.7)$$

where ψ_i denotes a one-electron wavefunction for electron i , and $\mathbf{x}_j = (\mathbf{r}_j, \sigma_j)$ the space and spin coordinates of the j th electron. Any anti-symmetric wavefunction can be written in the form of a linear combination of Slater determinants. This functional form also satisfies the criterion of indistinguishability.

The Rayleigh-Ritz principle[62] states that any trial wavefunction, Ψ , that is inserted into the eigenvalue problem defined by a Hamiltonian has a higher energy than the ground state energy, (where equality is true in the case of the ground state wavefunction). That is,

$$E_0 \leq \frac{\langle \Psi | H | \Psi \rangle}{\langle \Psi | \Psi \rangle} \quad (2.8)$$

By choice of a set of one-electron orbitals, a Slater determinant as in equation 2.7 can be constructed, and the energy evaluated. By varying these orbitals the Rayleigh-Ritz principle gives a criterion for assessing whether a set of orbitals is a better or worse approximation to the true ground state wavefunction than another set. It is also known as the variational principle.

By describing the wavefunction, Ψ , as a Slater determinant constructed from one-electron orbitals, and asserting the condition of orthonormality of these one-electron

orbitals ($\langle \psi_i | \psi_j \rangle = \delta_{ij}$), the Schrödinger equation can be rewritten as a set of one-electron equations:

$$(\hat{h}_i + \sum_{i \neq j} J_j - \sum_{i \neq j} K_j) \psi_i = \epsilon_i \psi_i, \quad (2.9)$$

where \hat{h}_i is referred to as the one-electron operator, as it is simply the energy of a single electron moving in the Coulombic potential of the nuclei, i.e.

$$\hat{h}_i \psi_i(\mathbf{x}) = \left(-\frac{1}{2} \nabla_i^2 - \sum \frac{Z_A}{r_{iA}} \right) \psi_i(\mathbf{x}), \quad (2.10)$$

where \mathbf{x} denotes the space-spin coordinates, and J_j and K_j are referred to as the Coulomb (or Hartree) and Exchange operators, respectively, and are two-electron operators, as they involve two different one-electron wavefunctions and space-spin coordinates. They are defined as:

$$J_j \psi_i(\mathbf{x}) = \psi_i(\mathbf{x}) \int d\mathbf{x}' \frac{|\psi_j^2(\mathbf{x}')|}{|\mathbf{r} - \mathbf{r}'|}, \quad (2.11)$$

$$K_j \psi_i(\mathbf{x}) = \psi_j(\mathbf{x}) \int d\mathbf{x}' \frac{\psi_j^*(\mathbf{x}') \psi_i(\mathbf{x}')}{|\mathbf{r} - \mathbf{r}'|}, \quad (2.12)$$

The Coulomb operator, J , represents the repulsive Coulombic potential at a position x , due to the charge distribution of the electron occupying orbital j . Thus equation 2.11 represents the force experienced by an electron moving in an orbital i due to the mean field of the electron moving in orbital j . The Exchange operator, K , is less easily understood with classical analogy, and arises due to the requirement that the wavefunction be antisymmetric. It is named exchange as the spin orbitals ψ_i and ψ_j have been “exchanged” with respect to the Coulomb operator. In the case of unlike spin, the exchange operator disappears, however in the case of like spins it discourages electrons from being in proximity to each other, due to the antisymmetry requirement. As an aside we note that if we set i equal to j in equation 2.9, we get:

$$(J_i(\mathbf{x}) - K_i(\mathbf{x})) \psi_i(\mathbf{x}) = 0. \quad (2.13)$$

As such the restriction $i \neq j$ can be removed from equation 2.9, and the summation can run over all values of j . This will have considerable significance later in the context

of hybrid functionals.

By introducing basis functions (usually either plane waves or atom-centred Gaussian-type functions, discussed further in Section 2.1.5) the set of one-electron equations can be expanded in terms of these basis functions and solved iteratively.

By approximating the Hamiltonian as a single Slater Determinant of one-electron orbitals we implicitly assume the motion of each electron is uncorrelated with another, and each electron sees a time-averaged charge distribution of its neighbours, whereas in reality their motion is correlated, for example their mutual Coulombic repulsion means they try to avoid each other. This is neglected in standard HF theory. Moreover, calculations of solids using HF theory tend to overestimate the band gap of insulators and semiconductors. HF calculations also scale badly due to the non-locality of the exchange potential. These features all limit the accuracy and usefulness of these methods, although extensions to HF theory mean HF methods continue to be widely used.

HF methods have not been used to solve the electronic structure problem for calculations in this thesis, although HF theory has been used in order to calculate the exchange energy. Moreover, the language of HF theory, as well as many features, such as the use of one-electron orbitals and the variational approach, is common to DFT, which shall be discussed in more detail in the following section.

2.1.3 Density Functional Theory

The majority of calculations in this thesis have been conducted using Density Functional Theory[63]. DFT has overtaken HF theory to become the most common theory used to calculate the electronic structure in materials modelling research, although HF is still often used in conjunction with the many extensions, such as MP2[64], which seek to describe the correlation energy. DFT reframes the problem of calculating the electronic structure in terms of charge density rather than the electronic wavefunctions, much like its precursor Thomas-Fermi theory[65].

The theoretical foundations of DFT are the Hohenberg-Kohn theorems. The first theory states that it is impossible to have two external potentials acting on an electron, $V(\mathbf{r})$ and $V'(\mathbf{r})$, whose difference is not a constant, that give rise to the same ground state charge density, $n(\mathbf{r})$. The reverse is also the case: a given charge density has a

uniquely corresponding external potential $V(\mathbf{r})$, plus an arbitrary constant c . That is,

$$n(\mathbf{r}) = n'(\mathbf{r}) \iff V(\mathbf{r}) - V'(\mathbf{r}) = c, \quad (2.14)$$

This theorem therefore states that there is a one-to-one correspondence between the charge density and the potential of a system. As the ground state electron density uniquely determines the Hamiltonian of the system, it follows that all measurable properties of the system can be expressed as functionals of the charge density.

Now if we return to the electronic Schrödinger equation, (see above equation 2.5), we can simplify:

$$\begin{aligned} E[\Psi] &= \langle \Psi | \hat{T} + \hat{U}_{ee} + \hat{U}_{en} | \Psi \rangle \\ &= \langle \Psi | \hat{T} + \hat{U}_{ee} | \Psi \rangle + \langle \Psi | \hat{U}_{en} | \Psi \rangle \\ &= \langle \Psi | \hat{T} + \hat{U}_{ee} | \Psi \rangle + \int d\mathbf{r} U_{en}(\mathbf{r}) n(\mathbf{r}), \end{aligned} \quad (2.15)$$

where \hat{T} denotes the kinetic energy, \hat{U}_{ee} the potential energy due to the interaction between the electrons and $U_{en}(\mathbf{r})$ the external potential due to the nuclei. The second term is expressed in terms of the charge density, but it is not immediately clear how to express the first term in the same way. As the first Hohenberg-Kohn theorem asserts that all observables can be expressed as a functional of the electron density, it follows that there exists an expression for the first term in terms of a functional of the charge density, such that we can express the total energy as a function of the charge density:

$$E[n] = F[n] + \int d\mathbf{r} U_{en}(\mathbf{r}) n(\mathbf{r}), \quad (2.16)$$

where $F[n]$ is the unknown functional, and is independent of the external potential.

The second Hohenberg-Kohn theorem, here stated without proof, is the variational principle, equivalent to equation 2.8 employed in HF theory, but expressed in terms of the charge density instead of the wavefunction:

$$E_V[n_0] \leq E_V[n']. \quad (2.17)$$

The electron density which corresponds to an energy minimum therefore also

uniquely determines the ground state wavefunction. By varying the charge density according to the constraint that the system contains a fixed number of electrons, an energy minimum can be found and the problem can be solved.

In order to approximate the kinetic energy, practical DFT calculations usually introduce a construct; a set of non-interacting electrons that have a ground-state density equal to the real system. This is known as the Kohn-Sham system[66].

The wavefunction solutions to this system are Slater determinants. The kinetic energy of the real system can then be rewritten as:

$$T = T_{\text{KS}} + T_c, \quad (2.18)$$

the sum of the kinetic energy of the system of non-interacting electron, T_{KS} , and the remainder of the kinetic energy due to the correlative behaviour of the electrons in the real system, T_c . The (non-interacting) electron density can be written in terms of the so-called Kohn-Sham orbitals as:

$$n = \sum_i |\psi_i^2|, \quad (2.19)$$

where the Kohn-Sham orbitals are solutions to a set of one-electron Schrödinger equations moving in an effective Kohn-Sham potential V_{KS} , as:

$$\left(-\frac{\hbar^2}{2m}\nabla^2 + V_{\text{KS}}\right)\psi_i = \epsilon_i\psi_i, \quad (2.20)$$

where the Kohn-Sham potential is the derivative of the energy functional with respect to the charge density,

$$V_{\text{KS}} = \frac{\delta E[n]}{\delta n}. \quad (2.21)$$

The Kohn-Sham orbitals can be found by iterative search, analogously to the Hartree-Fock orbitals. The introduction of the Kohn-Sham orbitals allows reformulation of the Schrödinger equation of equation 2.15 as:

$$E[n] = T_{\text{KS}}[n] + G[n] + \int d\mathbf{r}V(\mathbf{r})n(\mathbf{r}), \quad (2.22)$$

where the introduction of the Kohn-Sham kinetic energy ($T_{\text{KS}}[n]$) allows for the unknowns to be confined to the new functional $G[n]$, defined as:

$$\begin{aligned} G[n] &= F[n] - T_{\text{KS}}[n] \\ &= E_H + E_{XC}. \end{aligned} \tag{2.23}$$

Here $G[n]$ is a functional comprising the energy of the system of electrons except the component due to kinetic energy of the non-interacting Kohn-Sham electrons, $T_{\text{KS}}[n]$, and is therefore the integral of the Kohn-Sham potential minus the potential due to kinetic energy of the Kohn-Sham electrons, with respect to the electron density, over all space. The Coulombic interaction of the electron density with itself is the Hartree energy, E_H , and the last term, E_{XC} , the exchange-correlation energy, contains all errors in approximations made during the introduction of Kohn-Sham orbitals, including the error in the kinetic energy of the electrons, and the exchange and correlation energy. Almost all DFT calculations use the introduction of Kohn-Sham orbitals to greatly simplify the problem, but the approaches taken towards calculating the E_{XC} are various, with many different methods having common currency. Which approximation is most suitable for a particular system is an area of ongoing research. In practice different functionals are often used to investigate different properties.

The simplest commonly used exchange-correlation functional is the so-called Local Density Approximation (LDA), where the exchange-correlation functional per electron for the homogenous electron gas (HEG) is used for the system of interest. It is known as the ‘‘local’’ density approximation, as the energy only depends on the density at each point in space. The LDA functional is defined as:

$$E_{XC}^{\text{LDA}}[n] = \int d\mathbf{r} n(\mathbf{r}) \epsilon_{XC}[n(\mathbf{r})]. \tag{2.24}$$

Although the approximation is crude, the functional allows reasonably accurate calculation of a number of properties. The exchange functional of the HEG can be expressed analytically, however the correlation must be estimated. This is commonly done by interpolating between the (known) high-density and low-density HEG limiting cases, or by other methods, e.g. Quantum Monte Carlo simulations[67, 68].

The functional has a tendency to overbind materials in the solid state, and consequently to underestimate lattice parameters[69] and give incorrect results for chemical properties such as phase stability. Moreover, calculations using LDA functionals have a tendency to underestimate the band gap, and even incorrectly predict metallic behaviour in some semiconductors[70].

A more sophisticated approach towards modelling the exchange-correlation functional is the Generalised Gradient Approximation (GGA). This includes the gradient of the electron density, i.e. the next term in the derivative expansion of the charge density. The exchange-correlation energy under the GGA description is thus defined:

$$E_{XC}^{GGA}[n] = \int dr n(\mathbf{r}) \epsilon_{XC}[n(\mathbf{r}), \nabla n(\mathbf{r})]. \quad (2.25)$$

As the GGA functional makes use of the gradient of the charge density, it is referred to as semi-local. Although the LDA functional is universal, the GGA functional can take many different forms. Some commonly used ones include Becke's formulation[71], which is empirically derived, and the PW91 functional[72], and its simplified version, the PBE functional[73], which is calculated from purely theoretical considerations. Although the GGA functional is usually an improvement on calculations using the LDA functional, calculations using GGA functionals have a tendency to underbind and, as in the LDA case, to underestimate the one-electron band gap by approximately 40%[70].

2.1.4 Hybrid Functionals

One major source of error in DFT calculations arises from the so-called “self-interaction error”, where the electron density spuriously feels a Coulombic repulsion from itself. The error is contained in the Hartree energy, subsumed into the functional $G[n]$ in equation 2.23,

$$E_H[n] = \frac{1}{2} \int d\mathbf{r}' \frac{n(\mathbf{r})n(\mathbf{r}')}{|\mathbf{r} - \mathbf{r}'|}. \quad (2.26)$$

The term for the Hartree energy, or electron-electron interaction, also appears in HF theory, however there is a felicitous cancellation of the Coulomb and Exchange terms for identical one-electron orbitals (see equation 2.13 and subsequent discussion).

This observation was a motivating factor in the use of hybrid functionals, which seek to supplement DFT calculations with some of the exact exchange of HF theory. This allows a considerably more accurate description of the band structure of solids, and in particular usually yields a more accurate band gap. The calculation of HF exact exchange however makes computation considerably more expensive.

Two different hybrid functionals have been used in this thesis, the B3LYP functional[71, 74, 75, 76], and the PBE0 functional[77, 78, 79]. The B3LYP functional combines the LDA and GGA descriptions of both the exchange and correlation forces, and the exact exchange as calculated in HF theory, in a formula empirically adjusted to give good results with respect to ionisation energies and similar properties in molecules. Although the parameters of the functional have been designed for molecular calculations, B3LYP is frequently used to describe materials in the solid state, as the functional typically calculates fundamental properties, such as the lattice parameter and band gap, to a high degree of accuracy. The B3LYP functional is defined:

$$E_{xc}^{B3LYP} = E_{xc}^{LDA} + a_0(E_x^{HF} - E_x^{LDA}) + a_x(E_x^{B88} - E_x^{LDA}) + a_c(E_c^{LYP} - E_c^{LDA}), \quad (2.27)$$

where the x and c subscripts designate exchange and correlation, respectively, and E_x^{B88} and E_c^{LYP} refer to Becke's formulation of the GGA exchange and the correlation as derived from Lee, Yang and Parr, respectively. In the standard formulations, the parameters have the values of $a_0 = 0.20$, $a_x = 0.72$ and $a_c = 0.81$. For this study the a_0 parameter has been raised to 0.325, further discussion and justification of which is in Chapter 3. The PBE0 functional, as its name suggests, is based on the PBE GGA semi-local functional, and combines some HF local exchange in the total exchange-correlation description, as:

$$E_{xc}^{PBE0} = bE_x^{HF} + (1 - b)E_x^{PBE} + E_c^{PBE}, \quad (2.28)$$

where the parameter b is normally defined as 0.25, although this has been increased to 0.375 for calculations in this study (see Chapters 6 and 7 and Chapter 3 for justification of the altered parameter value). B3LYP was chosen for most calculations as it has been frequently and successfully used to model alkali halides, despite being initially

formulated primarily for molecular calculations. The use of PBE0 was motivated by attempts to describe the CsBr/Cu system with a mixed PBE0/PBE description using the ADMM method (see below), however this was ultimately unsuccessful. Despite this, the use of different functionals which produce similar results strengthens our belief that both functionals provide an adequate description of the exchange-correlation forces for our purposes.

2.1.5 Basis Sets and Pseudopotentials

In most practical DFT calculations, the Kohn-Sham orbitals are expanded by a set of basis functions. For all DFT calculations in this thesis either Gaussian-type orbitals (GTOs) or a mixture of GTOs and plane waves have been used as basis functions. The Kohn-Sham orbitals can be expressed as a linear combination of atom-centred GTOs as:

$$\psi_i = \sum_j c_{ij} \phi_j, \quad (2.29)$$

where c_{ij} denotes the coefficient of the j th basis function used to represent the Kohn-Sham one-electron orbital i . This is referred to as the linear combination of atomic orbitals (LCAO) approximation. The Gaussian functions are defined as a product of independent angular and radial components,

$$g_{lmn}(\alpha, r) = Y_l^m(\theta, \phi) r^{n-1} \exp(-\alpha r^2), \quad (2.30)$$

where $Y_{lm}(\theta, \phi)$ are spherical harmonics, simultaneous eigenfunctions of both the square of the orbital angular momentum and the projection of the orbital angular momentum about the azimuthal axis, and α is a parameter fitted for a specific system. The GTOs do not form a complete basis which fully spans the vector space of the original Kohn-Sham orbitals, and as such, their use introduces another potential source of error. In practice, a large number of basis functions of different α can be used, and the sufficiency of the basis set is established by calculating fundamental properties for a particular system and assessing whether there remains a large error associated with the basis set. GTOs have the advantage of being easily analytically integrable, and are simple to multiply together, and are therefore a computationally efficient choice. As a

further complication, the GTOs are usually combined together to form a linear combination of contracted basis functions which more closely resemble the wavefunctions of electrons moving in a central potential, such as an atom, as:

$$\phi_j(r) = \sum_k d_{jk} g(\alpha_j). \quad (2.31)$$

The use of plane wave basis sets in models using periodic boundary conditions is discussed below in Section 2.2.1.

In order to further reduce the computational cost of calculations, pseudopotentials have been used throughout this study. Pseudopotentials are operators which are introduced to represent the core electrons of an ion in a solid. This is justified by the observation that it is normally the valence electrons which are involved in chemical bonding and define defect characteristics, and therefore the introduction of pseudopotentials to model the core electrons greatly reduces the number of basis functions needed in order to describe the electronic structure of a system. Further tests to determine the adequacy of a pseudopotential and basis combination are required to ensure that the pseudopotential correctly reproduces any relevant observable properties of a system.

2.1.6 Auxiliary Density Matrix Methods

Although hybrid functionals are a great improvement on either LDA or GGA DFT functionals in terms of accuracy of description, they remain computationally expensive. In practical DFT calculations, we employ the linear combination of atomic orbitals description, and describe orbitals in terms of basis sets, as outlined above. In this way, a system can be described by the occupation of these basis sets. That is, we describe the wavefunctions in terms of an atom-centred basis:

$$\psi_i(r) = \sum_a C^{ai} \phi_a(r), \quad (2.32)$$

such that we can define a density matrix in terms of the coefficients of the basis functions:

$$P^{ab} = \sum_i C^{ai} C^{bi}. \quad (2.33)$$

We can now write the Hartree-Fock exact exchange in terms of a density matrix and two-electron integrals:

$$E_x^{HF}[P] = \frac{1}{2} \sum_{cdab} P^{ad} P^{bc} (ab|cd), \quad (2.34)$$

where the two-electron integral is defined as:

$$(ab|cd) = \int \int \phi_a(\mathbf{r}_1) \phi_b(\mathbf{r}_1) g(|\mathbf{r}_2 - \mathbf{r}_1|) \phi_c(\mathbf{r}_2) \phi_d(\mathbf{r}_2) d\mathbf{r}_1 d\mathbf{r}_2, \quad (2.35)$$

and $g(\mathbf{r})$ represents the Coulombic interaction ($1/r$).

By inspection it can be seen that the calculation of the exact exchange scales as N^4 , where N is the number of primitive basis set functions employed in the calculation, $\phi_a(\mathbf{r})$. Thus the use of hybrid functionals with large basis sets becomes very expensive as the system size increases. The auxiliary density matrix method (ADMM)[80] ameliorates this weakness by the introduction of a density matrix, \hat{P} , such that $\hat{P} \approx P$, but the new matrix is much smaller in size, i.e. has a significantly smaller basis. Thus the original density matrix expressed in a large basis is approximated by a new density matrix which uses a much smaller basis. This essentially involves projecting the larger basis onto a smaller basis, which is necessarily approximate. The Hartree-Fock exchange energy can then be written :

$$\begin{aligned} E_x^{HF}[P] &= E_x^{HF}[\hat{P}] + (E_x^{HF}[P] - E_x^{HF}[\hat{P}]) \\ &\approx E_x^{HF}[\hat{P}] + (E_x^{DFT}[P] - E_x^{DFT}[\hat{P}]), \end{aligned} \quad (2.36)$$

such that the exact exchange can be approximated by calculating the exact exchange for the smaller density matrix, and by applying a correction based on the discrepancy between the GGA exchange as calculated for the full and reduced density matrices. The method has been successfully used to conduct calculations in, for example, large MgO/Ag systems which would otherwise be unfeasible[81, 82]. The ADMM method, as implemented in CP2K, has been employed for calculations in Chapters 6 and 7 of this thesis.

2.1.7 Time-Dependent Density Functional Theory

Time-dependent Functional Theory (TD-DFT) extends DFT to excited states. In order to calculate the optical response of defects, linear-response TD-DFT has been used extensively in Chapter 4. The foundations of TD-DFT are the Runge-Gross Theorems[83], which are analogous to the Hohenberg-Kohn theorems in standard DFT. The first Runge-Gross theorem states that the expectation value of any observable of the system is a functional of the time-dependent charge density, and of the initial state of the wavefunction at time zero. This mapping is also unique (or one-to-one). The second Runge-Gross theorem states that solutions to the time-dependent Schrödinger equation correspond to stationary points of the action,

$$A = \int_{t_0}^{t_1} \langle \Psi(t) | i \frac{\delta}{\delta t} - \hat{H} | \Psi(t) \rangle. \quad (2.37)$$

Once again, as in standard DFT, a system of non-interacting Kohn-Sham electrons is introduced, and the time-dependent Schrödinger equation for the Kohn-Sham system is solved in order to calculate observables of the real system,

$$\left(-\frac{\hbar^2}{2m} \nabla^2 + v_{\text{KS}}(\mathbf{r}, t) \right) \psi_i(\mathbf{r}, t) = i \frac{\delta \psi_i(\mathbf{r}, t)}{\delta t}. \quad (2.38)$$

Where the Kohn-Sham potential is defined as:

$$v_{\text{KS}}(\mathbf{r}, t) = v_{\text{ext}} + \int d\mathbf{r}' \frac{n(\mathbf{r}', t)}{|\mathbf{r} - \mathbf{r}'|} + v_{xc}(\mathbf{r}, t), \quad (2.39)$$

$v_{xc}(\mathbf{r}, t)$ is the exchange-correlation potential, which is unknown and now time-dependent. It is a functional of the density at all times, and of the initial state. The first step towards estimating this potential used in calculations herein is to use the adiabatic approximation[84], such that the potential acts instantaneously to a perturbation, and thus does not have dependence on the history of the charge density. The exchange-correlation potential can now be described as the derivative of the exchange-correlation action with respect to the charge density,

$$v_{xc}[n(\mathbf{r}; t)](\mathbf{r}, t) = \frac{\delta A_{xc}}{\delta n(\mathbf{r}; t)}. \quad (2.40)$$

The adiabatic approximation means that the exchange-correlation potential is a different expression for different t , and only has parametric dependence on t , i.e. for a particular point in time t , the charge density is a different function of \mathbf{r} . The term v_{ext} is the external potential acting on the electrons e.g. a laser. By considering a perturbation, one can take the first order term in an expansion around an external potential at a time t , and find the linear density-density response function, $\chi(\mathbf{r}, \mathbf{r}', t, t')$. By the first Runge-Gross theorem, it is sufficient to find the linear response function of the non-interacting Kohn-Sham system, $\chi_{\text{KS}}(\mathbf{r}, \mathbf{r}', t, t')$. By Fourier transforming into frequency space a function of the dynamic polarisability, $\alpha(\omega)$, of the finite system can be obtained, such that excitation energies are the poles of the response function. These can be transformed into Casida's equations[85], such that the problem is a coupled eigenvalue equation which can be written in matrix notation:

$$\begin{pmatrix} \mathbf{A} & \mathbf{B} \\ \mathbf{B}^* & \mathbf{A}^* \end{pmatrix} \begin{pmatrix} \mathbf{X} \\ \mathbf{Y} \end{pmatrix} = \omega \begin{pmatrix} -1 & 0 \\ 0 & 1 \end{pmatrix} \begin{pmatrix} \mathbf{X} \\ \mathbf{Y} \end{pmatrix}, \quad (2.41)$$

where \mathbf{X} and \mathbf{Y} are the eigenvectors consisting of the coefficients corresponding to the transitions between states. The oscillator strengths of each transition can be calculated from these. The elements of \mathbf{A} and \mathbf{B} are calculated as:

$$\begin{aligned} \mathbf{A}_{ia,jb} &= \delta_{ij} \delta_{ab} (\epsilon_a - \epsilon_i) + \mathbf{K}_{ia,jb}, \\ \mathbf{B}_{ia,jb} &= \mathbf{K}_{ia,bj}, \end{aligned} \quad (2.42)$$

where i, j and a, b refer to occupied and unoccupied orbitals, respectively, and $\mathbf{K}_{ia,jb}$ is the coupling matrix and is defined as:

$$\mathbf{K}_{ia,jb} = (ia|f_H|jb) + (ia|f_{xc}|jb), \quad (2.43)$$

where f_H and f_{xc} are the Hartree and exchange-correlation kernels, defined as:

$$\begin{aligned} f_H(\mathbf{r}, \mathbf{r}') &= \frac{1}{|\mathbf{r} - \mathbf{r}'|}, \\ f_{xc}[n](\mathbf{r}, \mathbf{r}') &= \frac{\delta v_{xc}[n](\mathbf{r})}{\delta n(\mathbf{r}')}. \end{aligned} \quad (2.44)$$

Attempts to improve the accuracy of TD-DFT calculations are usually centred on improving the approximate descriptions of the exchange-correlation kernel, f_{xc} , which is not known analytically and must be approximated. Analogously to the use of hybrid functionals in standard DFT, where they ameliorate the self-interaction error and improve the standard DFT description of the band structure of solids, hybrid functionals can be used in TD-DFT to improve the accuracy of calculated linear response. Also of use and applied here is the so-called Tamm-Dancoff Approximation[86], where $\mathbf{B} = 0$, such that equation 2.41 can be written in the simpler form:

$$\mathbf{A}\mathbf{X} = \omega_{\text{DFT}}\mathbf{X}, \quad (2.45)$$

The poles of polarisation can thus be calculated, and the relative oscillator strengths of the transitions, although the Tamm-Dancoff approximation means that we can no longer obtain the absolute values of the oscillator strengths. These calculations lead to a series of vertical lines of different height and infinitesimal width which constitute the polarisable response function:

$$A(\omega) = \sum_i f_i \delta(\Omega_i - \omega), \quad (2.46)$$

where ω is the angular frequency of an incident photon, δ is the Dirac delta function, and f_i and Ω are the relative oscillator strength and excitation frequency of the i th transition. By taking the convolution of the polarisability response function with a Gaussian function of specified width, these lines can be transformed into an absorption spectrum, where the convolution represents real broadening effects, which arise due to, for example, phonons in the sample and the inhomogeneity of the sample which contains structural and point defects, and the produced spectrum can then be compared to the experimentally observed spectrum, as:

$$A(\omega) = \sum_i \frac{f_i}{\sqrt{2\pi\sigma}} \exp\left(\frac{-\hbar^2(\Omega_i - \omega)^2}{2\sigma}\right). \quad (2.47)$$

The value for σ has been chosen so as to approximate the experimental peaks, and for calculations in Chapter 4, $\sigma = 0.1$ eV is used. The orbitals composing the transitions then offer insight into the nature of the underlying transition corresponding

to absorption peaks in the spectrum, especially when a transition from a particular one-electron orbital to another one-electron orbital contributes significantly more than any other transitions to a particular excitation.

2.1.8 Semi-empirical Dispersion Correction

DFT is a static theory in its standard formulation. This leads to a neglect of van der Waals forces, whereby instantaneous fluctuation of the electron density induces dipoles which gives rise to attractive forces between atoms. Although comparatively small with respect to, for example, electrostatic forces, van der Waals forces can be significant and lead to behaviour qualitatively different from that predicted by standard DFT calculations.

A number of different methods are available to account for the neglect of dispersion forces in standard DFT. Although there have been advances in new functionals which include terms which approximate van der Waals forces (e.g. see Refs.[87, 88, 89]) these approaches remain largely untested for metal-insulator systems. One of the most prevalent and durable strategies involves the inclusion of a new additive classical term in the calculation of the total energy. In particular, many calculations in this thesis have employed Grimme's semi-empirical dispersion correction (D2)[90]. The D2 dispersion correction is defined as:

$$E_{\text{disp}} = -S_6 \sum_{i=1}^{N-1} \sum_{j=i+1}^N \frac{C_6^{ij}}{R_{ij}^6} f_{\text{damp}}(R_{ij}), \quad (2.48)$$

where N is the number of atoms in the system, C_6^{ij} designates the dispersion coefficient for atom pair ij , R_{ij} is the interatomic distance and S_6 is a global scaling variable that is usually an (empirically) fixed value for a particular functional, for example 1.4 when used with BLYP and 0.7 using the PBE functional. The theory is most valid for ionic systems, for systems with some degree of covalency, results may be improved by introducing a coefficient C_8^{ij} which has inverse dependence on R^8 , and again for even higher powers. The D3 correction includes these extra terms. In ionic systems, where the instantaneous dipole interactions is significantly stronger than that of higher order multipoles, this remains a valid approximation. The damping term, f_{damp} , is

incorporated in order to avoid singularities for small values of R_{ij} , and is defined as:

$$f_{\text{damp}}(R_{ij}) = \frac{1}{1 + e^{-\alpha(R/R_0 - 1)}}, \quad (2.49)$$

where R_0 is the sum of the atomic van der Waals radii. Dispersion forces have been included in some calculations in Chapters 6 and 7 of this thesis, as calculations of the work function of the CsBr/Cu system are sensitive to the metal-insulator separation, and the inclusion of van der Waals forces can significantly alter this separation.

2.2 Nudged Elastic Band Methods

The Nudged Elastic Band (NEB) method is a technique used in order to find the transition state (TS) between two minima on an adiabatic potential energy surface (APES). The difference in energy along the minimum energy pathway (MEP) between the TS saddle point and one of the minima is the amount of energy required to transition from one state to another. The technique is therefore a common tool used in order to estimate the barrier to diffusion around the lattice for a particular defect, and has been employed for calculations in Chapter 7 of this thesis. In order to estimate the barrier the MEP must be identified, followed by the maximum energy along this pathway (i.e. the energy at the TS). The family of elastic band methods are all so-called as the MEP is found by constructing a set (typically 4 - 20) of images or replicas of the system between the initial and final states, and connecting them by springs. The springs enforce a continuity between the images. By minimising the elastic energy of the springs MEP can be found.

The ‘‘nudged’’ elastic band methods are slightly more elaborate; the parallel components of the true forces on each image is removed, and the perpendicular component of the spring forces are also subtracted from the calculation, such that the spring forces maintain an even degree of spacing between each image, and the images do not ‘slide-down’ the MEP, away from the points of chief interest (i.e. the maxima).

If there exists a set of $N + 1$ images, whose coordinates are denoted $[\mathbf{R}_0 - \mathbf{R}_N]$, where \mathbf{R}_0 and \mathbf{R}_N themselves are the coordinates of the initial and final states, respec-

tively, then the total force acting on an image is given by:

$$\mathbf{F}_i = \mathbf{F}_i^s|_{\parallel} - \nabla E(\mathbf{R}_i)|_{\perp}, \quad (2.50)$$

where the two components are the (parallel) spring force and the (perpendicular) true force.

A minimisation algorithm can then be used in order to move the images according to forces and find the MEP. Typically, none of the images correspond to the geometry of the TS, and further work must be done to extract an estimate of the maxima (i.e. barrier to diffusion) from the MEP.

The climbing image NEB method (CI-NEB) is a further modification which ensures one of the images “climbs” up the MEP to the transition state. This is enforced by identifying the image closest to the maxima after a few initial NEB iterations, and reversing the direction of the (parallel) spring force component acting on this image. The other images define the single degree of freedom along the MEP which the spring force-removed image may move, and thus finds the maximum. Therefore the CI-NEB method finds both the MEP and the TS without any additional computational cost with respect to the standard NEB method.

2.3 Defect Models

2.3.1 Periodic Boundary Conditions

Many of the calculations undertaken in this thesis involve the use of a model with periodic boundary conditions. The solutions to the Schrödinger equation in a periodic potential are Bloch functions, which have the form:

$$\Psi_{\mathbf{k}}(\mathbf{r}) = u_{\mathbf{k}}(\mathbf{r})e^{i\mathbf{k}\cdot\mathbf{r}}, \quad (2.51)$$

where $u_{\mathbf{k}}(\mathbf{r})$ has the period of the lattice, i.e. $u_{\mathbf{k}}(\mathbf{r}) = u_{\mathbf{k}}(\mathbf{r} + \mathbf{a})$ for a lattice vector \mathbf{a} , and \mathbf{k} is one of the set of allowed wavevectors determined by the symmetry of the system. Bloch’s theorem states that the one-electron eigenfunctions can be expressed as the product of a plane wave and a function with the periodicity of the lattice. These form a complete set of eigenfunctions. Due to the translational symmetry, it is sufficient

to calculate the eigenfunctions for values of \mathbf{k} that lie in the first Brillouin zone, which is the reciprocal lattice equivalent of the primitive unit cell, in order to describe any eigenstate of the electronic wavefunction.

We can expand the periodic function $u_{\mathbf{k}}(\mathbf{r})$ as a Fourier series, as:

$$u_{\mathbf{k}}(\mathbf{r}) = \sum_{\mathbf{G}} c_{j,\mathbf{G}} e^{i\mathbf{G}\cdot\mathbf{r}}, \quad (2.52)$$

where \mathbf{G} is a reciprocal lattice vector, and $c_{j,\mathbf{G}}$ are the expansion coefficients. Substituting this expansion into equation 2.51 gives an expression for the wavefunction in terms of a linear combination of plane waves:

$$\Psi_{\mathbf{k}}(\mathbf{r}) = \sum_{\mathbf{G}} c_{j,\mathbf{k}+\mathbf{G}} e^{i(\mathbf{k}+\mathbf{G})\cdot\mathbf{r}}. \quad (2.53)$$

As the energy of each wave is proportional to the square of the wavevector one can define a cutoff energy:

$$E_{\text{cut}} = \frac{1}{2} |\mathbf{G} + \mathbf{k}|^2. \quad (2.54)$$

As the kinetic energy of the plane waves becomes larger, at some point these must contribute less to the total wavefunction, and the coefficients must be very small, such that they may be neglected. In practice this cutoff is usually found by varying the cutoff value and examining the effect this has on calculated total energy.

Although \mathbf{k} essentially forms a continuum in the first Brillouin Zone due to the high density of points, it is smoothly-varying, and as such a particular point in \mathbf{k} -space has a similar value to other points close to it. The eigenfunction can then be estimated by summing over a finite number of \mathbf{k} -points sampled with a regular mesh in reciprocal space, the so-called Monkhorst-Pack[91] scheme. As the mesh becomes finer, the approximation of the sum to the integral over all space becomes more accurate.

2.3.2 Embedded Cluster Methods

As an alternative to models employing periodic boundary conditions, Chapters 4 and 6 have made use of mixed quantum mechanics/molecular mechanics (QM/MM) models, using the GUESS code[92].

The procedure begins by creating a nanocluster supplemented with auxiliary point

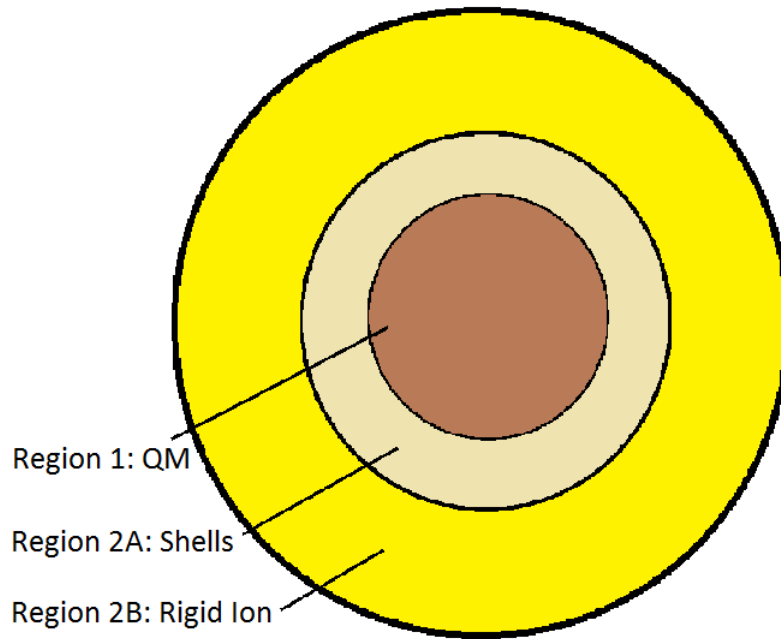


Figure 2.1: Regions 1, 2A and 2B of the embedding scheme.

charges, placed in positions such that the electrostatic field in the nanocluster resembles that of the infinite crystal. The system is then partitioned into three regions, as depicted in Figure 2.1. Region 1 consists of atoms modelled with fully *ab initio* QM techniques, with the electronic structure described using DFT. This is embedded within a polarisable region of classical shell model atoms, designated Region 2A, which is in turn embedded into a region of classical point ions, Region 2B. The atoms in Region 2A are able to move under the influence of forces, those in Region 2B are fixed. Certain cations from the interface between Regions 1 and 2A are designated “interface atoms”, and are modelled using large-core pseudopotentials. These act as to confine the electron density to Region 1, and mediate forces between Regions 1 and 2.

The nanocluster is created by creating a lattice of positive and negative ions and supplementing it with a skin of point charges which surround the nanocluster, such that in the central region of the cluster the electrostatic potential is equal to the Madelung potential of the infinite crystal plus an arbitrary constant. This has been achieved by constructing a unit cell with auxiliary point charges that are placed so as to negate the multipoles of the unit cell. The electrostatic potential of a finite cluster which is constructed from a unit cell with no quadrupole moment converges towards the Ewald potential of an infinite crystal plus a constant[93]. These charges can be placed in such a way that a nanocluster created from repetition of these unit cells cancel each other

out, leaving only a skin of point charges outside the nanocluster[93].

Nanoclusters of various sizes have been created from unit cells augmented with auxiliary charges so as to eliminate the quadrupole, octopole and sexadecapole moments, $l = 2, 3$ and 4 , respectively. The aim was to create a nanocluster which has the minimum number of atomic centres, that is, ions plus auxiliary charges, while still maintaining an on-site electrostatic potential on each ion sufficiently close to that of the infinite crystal. A large number of ions and auxiliary charges demands more computation in order to calculate the forces in the system, and is therefore undesirable. The variation of on-site electrostatic potential on the anions as a function of distance from the centre of the nanocluster, for nanoclusters with eliminated moments up unto $l = 2, 3$ and 4 , respectively, is depicted in Figure 2.2.

It is clear from the figure that the $l = 2$ and 3 cases, the nanoclusters are still converging to the electrostatic potential of the infinite crystal at the radii of nanocluster examined here, whereas when eliminating up to the $l = 4$ moment, the different sizes of nanocluster already seem to have converged to the Madelung potential. The nanocluster with 61 500 atomic centres, where moments up unto $l = 4$ have been eliminated, has been chosen to model CsBr defects in the bulk in this study (See Chapter 4). The graphs shows that the electrostatic potential varies by less than 1 meV at distances up to approximately 16 \AA from the centre of the nanocluster. Although technically forces are determined by the gradient of the electrostatic potential, rather than the absolute values of the on-site electrostatic potential, the potential generated by the auxiliary charges and nanocluster should be a relatively smooth, well-behaved function, such that examining the variation of the on-site potential should be a good guide towards the working accuracy of the simulated potential.

In Chapter 6, an embedded cluster model of the $\beta(100)$ surface has been examined. In the case of the $\beta(100)$ surface, the unit cell has no quadrupole moment, and therefore does not need as many point charges in order to reproduce a well-behaved approximation to the Madelung potential. For more details of these calculations see Chapter 6.

Forces between the atoms of Region 2 and other atoms have been modelled using

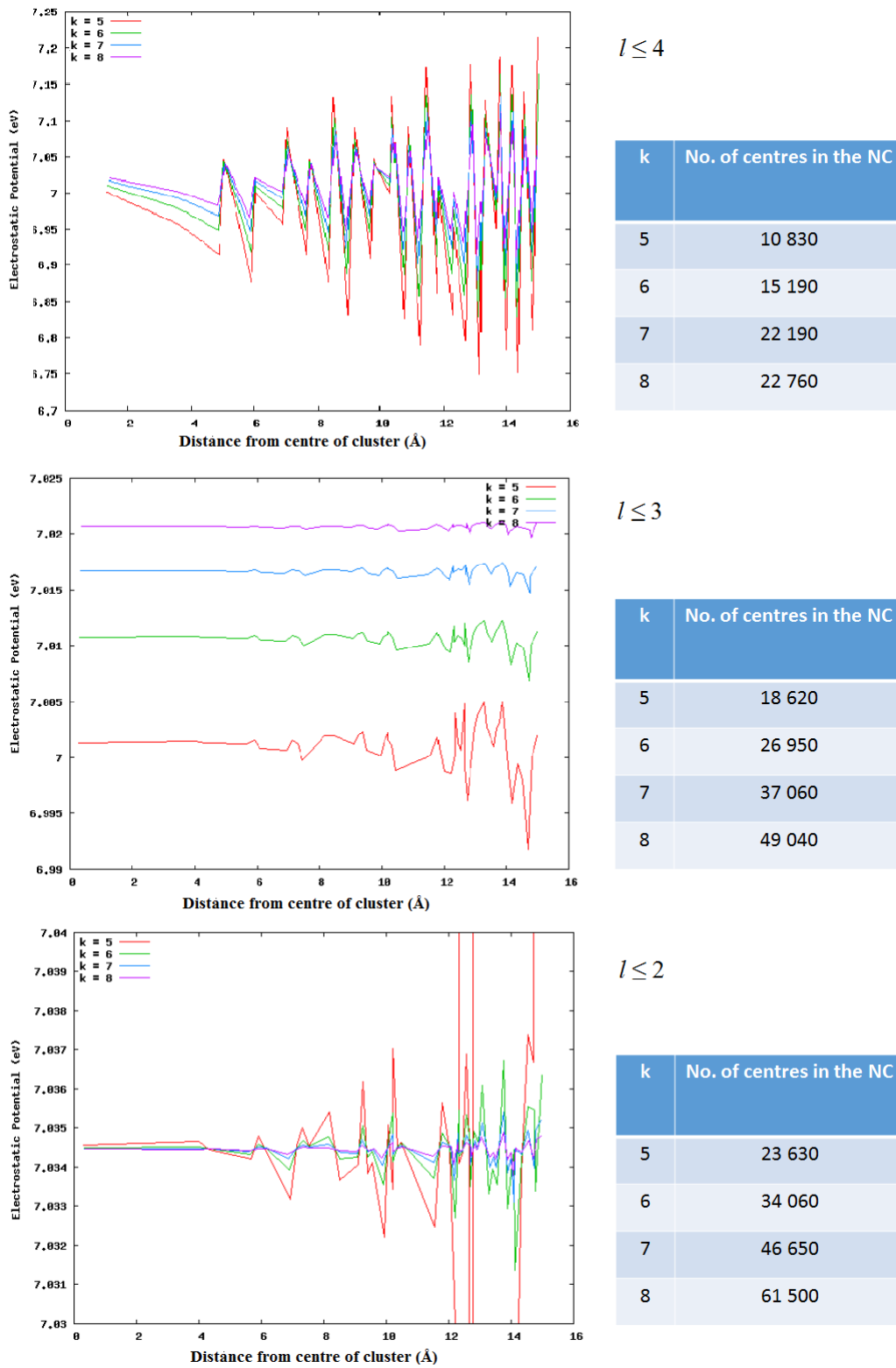


Figure 2.2: The variation of on-site electrostatic potential on the anions as a function of distance from the centre of the nanocluster, for nanoclusters with eliminated moments up unto $l = 2, 3$ and 4 . $l = 1$ corresponds to the dipole moments, $l = 2$ to the quadrupole moments and so on. The nanocluster is constructed with $(2k + 1)^3$ unit cells.

Buckingham potentials[94] of the form:

$$\Phi(r) = A\exp(-Br) - \frac{C}{r^6}, \quad (2.55)$$

where r is the distance between the two centres, and A , B and C are fitted parameters of the potential. The first term is repulsive and mimics Pauli repulsion, while the second term is attractive, and describes the van der Waals energy. The two shells of nearest neighbour cations of each anion in Region 1, that are not already defined as Region 1 atoms, are defined as interface atoms.

When performing geometry optimisation calculations, forces in Regions 1 and 2 are calculated simultaneously, with atoms then moved under the influence of forces until residual forces are smaller than a specified degree of accuracy.

Chapter 3

Modelling bulk CsBr and CsBr surfaces

The aim of this chapter is two-fold. The first aim is to critically assess and compare models of bulk CsBr using periodic boundary conditions, using embedded cluster methods, and using different functionals (PBE0 and B3LYP). The effect of increasing the amount of HF exact exchange from their standard values in hybrid functionals is examined. The second aim is to examine the experimental literature for evidence of the surface topology of CsBr grown by molecular beam epitaxial techniques on the LiF(100), KBr(100) and Cu(100) surfaces, as a preliminary to modelling desorption from CsBr films.

3.1 Introduction

Bulk CsBr has been modelled using three different models in this thesis, two using periodic boundary conditions (PBCs), as implemented in the CRYSTAL09[95] and CP2K[96] programs, and one using QM/MM embedding cluster methods. The use of three different models has been motivated by the various requirements of each situation. For example PBC models have the advantage of being relatively simple with regards to embedding techniques, with considerably less potential sources of error, and embedding cluster methods allow for the calculation of the electron affinity and ionisation potential of a system without requiring post-facto charge corrections.

It is well known that standard DFT functionals, using either LDA or GGA approximations tend to overestimate and underestimate the band gap of wide band-gap insulators such as the alkali halides, respectively. This is of particular significance

when examining properties which directly relate to the band gap of a material, such as the energy of an exciton or the optical properties of defects. Although hybrid functionals greatly improve the description of the band structure of the alkali halides, there remains a tendency to underestimate the band gap. Increasing the amount of HF exact exchange used in the standard formulation of functionals such as PBE0 and B3LYP is known to produce models with a one-electron band gap closer to that measured in experiment. However it is not always clear how ad hoc adjustment of these parameters affect calculations of other properties such as the lattice parameter.

All models used in this thesis make at least some use of atom-centred GTOs to describe the electronic structure of CsBr. The specific basis sets used are indicated in each chapter. GTO's are often computationally efficient with respect to plane waves, and allow for an intuitive interpretation of results in terms of atomic orbitals. As there exists no rigorous criterion from which to assess atom-centred GTO basis sets as sufficiently or insufficiently large for the task at hand, so an examination of various relevant properties is often necessary in order to establish whether a model is reproducing the salient properties of a material with comparison to experiment. In order to examine the variation of calculated properties of CsBr from the various models as a function of modelling technique, functional and basis set we here examine various fundamental properties as calculated in the various cases, and critically assess the degree to which they agree with each other.

Cu photocathodes are coated by CsBr thin films by particle vapour deposition (PVD) techniques. Calculations in Chapters 5 and 6 attempt to elucidate the results of desorption experiments conducted on LiF, KBr and Cu grown CsBr. These methods are sometimes referred to as molecular beam epitaxial (MBE) techniques, which emphasizes the role the epitaxial frame (i.e. LiF(100), KBr(100) or Cu(100)) plays in dictating the growth morphology of CsBr thin films. Here we conduct a brief survey of the experimental literature in order to gain information on how we expect the structure of the thin films to look like based on growth conditions and epitaxial frame. This information will then be used to justify models of CsBr thin films used in later chapters of this thesis.

3.2 Results

3.2.1 Modelling Bulk CsBr

The three different models used in this thesis to describe bulk CsBr are (1) a model implemented in CRYSTAL09 using PBCs, GTOs and a modified version of the B3LYP functional (2) a model implemented in CP2K using PBCs, a mixed plane-wave/Gaussian basis set and a modified PBE0 functional and (3) an embedded cluster model where the electronic structure of the QM region has been described using a modified B3LYP functional and GTOs.

The three different models of bulk CsBr therefore allow for an analysis of 1) the differences of calculated properties between the B3LYP and PBE0 functionals, 2) the effects of varying the amount of HF exact exchange on properties of CsBr such as the lattice parameter, 3) the sufficiency of basis sets used in each model and 4) the differences between models using PBCs and embedding cluster schemes.

The basis set used with CRYSTAL09 (taken from the CRYSTAL basis set library and Mike Towler's[97] basis set library, $6sp1d/4sp1d$ on the Cs ions and $4sp1d/2sp1d$ on the Br ions) and for the calculations contained in Chapter 5 (Double-Zeta valence basis sets taken from the CP2K library) is significantly smaller than that used for calculations in CP2K. The smaller basis was motivated by the need to use a large supercell so as to minimise the error due to spurious interactions between a defect and its periodically repeated image. The large number of ions in the supercells necessitated the use of a comparatively small basis set in order to make calculations computationally feasible, and was taken from Mike Towler's basis set library[97].

The lattice parameter and band gap have been calculated in CRYSTAL09 with the relatively sparse basis set for both the B3LYP and PBE0 functionals, where the amount of HF exact exchange included in the functional has been varied from the 'standard' amount up to the amount used in the studies in this thesis. The results are plotted in Table 3.1.

The variation of calculated lattice parameter for each functional with differing proportions of HF exact exchange over the ranges examined is small ($\approx 0.5\%a_0$). This is most likely due to the highly ionic nature of the bonds in CsBr, the attraction between the ions of which arises predominantly from electrostatic forces, and we therefore ex-

Functional	Lattice Parameter (\AA)	%	Band Gap (eV)	%
B3LYP (20)	4.1796	1.5	6.37	12.7
B3LYP (32.5)	4.1664	1.9	7.36	0.8
PBE0 (25)	4.0801	3.9	6.96	4.7
PBE0 (32.5)	4.0624	4.3	7.50	2.7
PBE0 (37.5)	4.0601	4.4	7.86	7.7
Exp.	4.245	-	7.3	-

Table 3.1: The lattice parameter(a_0) and band gap of CsBr in CRYSTAL09 as calculated by each functional. The number given in brackets after the functional name indicates the fraction of HF exchange energy.

Functional	Lattice Parameter (\AA)	%	Band Gap (eV)	%
B3LYP (20)	4.4685	5.3	5.72	21.6
B3LYP (32.5)	4.4595	5.1	6.64	9.0
PBE0 (25)	4.3543	2.6	6.28	14.0
PBE0 (32.5)	4.3433	2.3	6.94	4.9
PBE0 (37.5)	4.3363	2.1	7.30	0.0
Exp.	4.245	-	7.3	-

Table 3.2: The lattice parameter and band gap of CsBr in CP2K as calculated by each functional. The number given in brackets after the functional name indicates the fraction of HF exchange energy.

pect it to be the case for other alkali halides. The electron transfer leaves two-filled shells, such that the electron density is confined to orbitals close to the ions. However the change in the band gap is substantial, and indeed it is this change that originally motivated modification of the functionals. The calculated lattice parameter is within 2% of the experimental value for calculations using the B3LYP functional, however when the PBE0 functional is used, the lattice parameter is significantly underestimated by approximately 4%.

A survey[98] of the calculated lattice parameters of various simple elements and compounds in the solid state using the PBE0 functional with converged plane wave basis sets has found that all values are within 2% of the experimental values, with few exceptions. Where there are exceptions, the lattice parameter is more often overestimated rather than underestimated.

The lattice parameter and band gap have been conducted using CP2K and the CP2K basis sets for the various functionals. The results are plotted in Table 3.2.

As in the case in CRYSTAL09, the variation of the lattice parameter as a result of modifying the HF exchange contribution is small for both functionals. B3LYP ap-

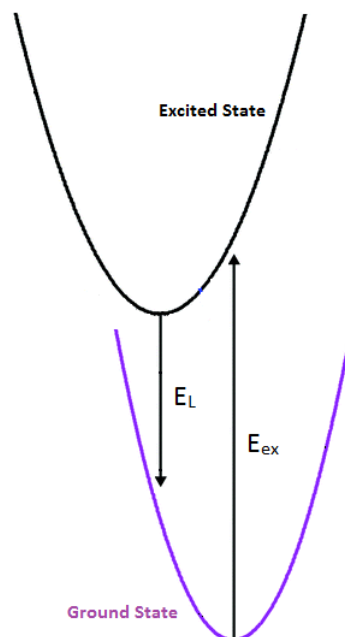


Figure 3.1: A schematic of the ground state and excited state potential energy surfaces. The exciton energy, E_{ex} , and luminescence energy, E_{L} , are both estimated as vertical transitions (i.e. instantaneous) from one potential energy surface to the other.

appears to significantly overestimate the lattice parameter, and indeed every functional calculates the lattice parameter as larger than the experimentally measured value. The PBE0 calculates the lattice parameter closest to the experimental one, with an error of approximately 2%. VASP plane-wave converged calculations using PBE0 with 25% and 32.5% exact exchange calculate the lattice parameters as 4.347 Å and 4.335 Å, respectively. These are close to the values calculated in Table 3.2, suggesting that the basis set used in CP2K is sufficiently large.

The overestimation of the B3LYP functional is quite large. It has been observed that there is a general tendency for B3LYP to overestimate the lattice parameter of heavier, wide band-gap materials[99, 100], so it is not clear *prima facie* if the error is due to the relatively small basis set or the functional. In addition, due to the different methods of calculation and approximation in CP2K and CRYSTAL09, a portion of the error may be due to the use of different programs, although we expect this effect to be comparatively small.

In order to further examine the validity of the CRYSTAL09 calculations with the B3LYP(32.5) functional, a number of properties have been calculated. The off-centre triplet exciton luminescence energy has been calculated in all three models, (that is in

CRYSTAL09, CP2K and GUESS). The energy has been estimated as the difference in energy between the relaxed off-centre exciton geometry state, and the singlet state in the same geometry (see Figure 3.1. In the embedding cluster model(B3LYP(32.5)) and in the CP2K(PBE0(37.5)) model this energy has been calculated as 3.63 and 3.42 eV, errors of 4.0% and 3.4%, respectively (experimental value = 3.54 eV). In the CRYSTAL09 model (32.5) the energy is calculated as 5.15 eV, an overestimate of 45%.

In order to further compare the model of CsBr using B3LYP(32.5) in CRYSTAL09 and using PBE0(37.5) in CP2K, the bulk modulus has been calculated by fitting a curve to energy-volume data for the two models, the so-called Birch-Murnaghan equation of state[101], defined as:

$$E(V) = E_0 + \frac{9V_0B_0}{16} \left\{ \left[\left(\frac{V_0}{V} \right)^{\frac{2}{3}} - 1 \right]^3 B'_0 + \left[\left(\frac{V_0}{V} \right)^{\frac{2}{3}} - 1 \right]^2 \left[6 - 4 \left(\frac{V_0}{V} \right)^{\frac{2}{3}} \right] \right\}$$

where a quantity of $B'_0 = 3$ has been fixed, as this has been found to be a useful approximation in order to estimate B_0 in other studies. For more extensive discussion see Refs.[102, 103]. The bulk modulus has been calculated as 15.50 and 15.98 GPa for B3LYP(32.5) and PBE0(37.5), respectively. Both of these are in good agreement with the experimental value of 15.77 GPa[104]. The formation energy of an F-centre has also been calculated in all three models, with all values lying within a range of 0.2 eV.

This evidence suggests that the basis set used in CRYSTAL09 calculations, while sufficiently complete to describe many ground-state properties, such as dielectric constant, bulk modulus, band gap etc. is lacking the flexibility to describe particular excited states, where the electron density may be distributed in more complex ways than in the ground state. In particular, the basis set may be good at describing the ground-state as the system is ionic, with an electron transferred from cation to anion, such that an electron shell is completed and the majority of the electron density is close to the ions, and are well described by compact basis functions.

Contrastingly, the good estimates for the luminescence energy in the other two models provide further evidence for the sufficiency of the basis sets used in these models. Nevertheless, despite the slight sparsity in the CRYSTAL09 basis set, calculations relating to the hyperthermal relaxation mechanisms, including excitons at the surface,

are quantitatively and qualitatively very similar to the descriptions in the other models (see below in Section 5.4.1 for further details). We conclude that a slightly deficient basis set used in CRYSTAL09 results in a poor calculated triplet luminescence energy in the bulk. Despite this, the basis seems sufficiently robust for all applications here, including the description of excitons at CsBr surfaces.

The (minor) overestimation of the lattice parameter by both the B3LYP and PBE0 functional in CP2K motivated an investigation into the effects of including a description of van der Waals forces into the calculations of bulk CsBr, which is described in the next subsection.

3.2.2 Van der Waals Forces

It is well known that the rocksalt alkali halides undergo a transition from the rocksalt NaCl (B1) structure to a CsCl-type (B2) structure under pressure[105]. It is also well known that the caesium halides (CsCl, CsBr, CsI) adopt the B2 structure in the ground state, and that CsCl transform from B2 to B1 phase at 742 K[106]. For these reasons it is clear that the two phases are energetically close. Despite this, many DFT calculations using standard GGA functionals favour the B1 phase over the B2 phase even for the caesium halides. Although most fundamental properties of CsBr are well-predicted by the models outlined, the cohesive energy is overestimated. Moreover the calculations of bulk CsBr in CP2K using the PBE0 consistently overestimates the lattice parameter, suggesting that the attractive forces between the ions are underestimated. It has been suggested that the reason for this error may be due to the neglect of dispersion forces[107]. In order to test this hypothesis, van der Waals forces have been added to the CP2K calculations of bulk α -CsBr and β -CsBr and the resulting changes in the lattice parameter and cohesive energy noted.

Although there are a number of different ways to include dispersion effects into standard DFT, the fairly simple additive pairwise potentials of Grimme et al. have proved to be very robust, leading to an improved description in a variety of different cases. Not only do Grimme's corrections generally function surprisingly well with comparison to more sophisticated attempts to include dispersion forces, such as a number of newly developed functionals[87, 88, 89], they also have the advantage of relative conceptual simplicity. The D2 and D3 descriptions are most appropriate for ionic com-

Dispersion Method	Lattice Parameter (Å)	%
α -CsBr	4.336	2.1
D2	4.243	< 0.1
D3	4.334	2.1
Exp.	4.245	-
β -CsBr	7.343	1.7
D2	7.222	< 0.1
D3	7.383	2.3
Exp.	7.26 [109]	-

Table 3.3: The calculated lattice parameter of both α - and β -CsBr with the D2 and D3 descriptions, and the calculated values in the absence of any dispersion correction.

Structure	No Dispersion	D2	D3	Exp.
α -CsBr	5.93	6.18	6.46	6.48[110]
β -CsBr	5.98	6.17	6.38	< 6.48

Table 3.4: The effect of including dispersion forces on the cohesive energy of both α - and β -CsBr.

pounds, such as discussed here, as they take no account of any charge transfer effects. The D3 formulation includes an attractive term proportional to R^8 , and is intended to be a refinement of the D2 description.

The D2 and D3 formulations have been included here, where the parameters for Cs have been taken from Ref.[108]. The results of the calculations are displayed in Tables 3.3 and 3.4.

As can be seen from the data, inclusion of both D2 and D3 improves the description of bulk CsBr. The use of D2 brings the lattice parameters to within less than a tenth of a percent of the experimentally measured values, a large improvement on the description which does not include dispersion, which has lattice parameters about two percent off of the measured values. Using the PBE0 + D3 functional however barely changes the lattice parameters from the values obtained without the inclusion of any dispersion effects. Inclusion of either dispersion method correctly identifies the B1 structure as the ground-state, in contrast to the case of no dispersion correction, where the B2 method is incorrectly calculated as being lower in energy. The D3 method has the advantage of having less empirical parameters than the D2 method, and improves the cohesive energy to a value very close to experiment (in the B1 case). The tendency for Van Der Waals forces to increase the cohesion energy in α -CsBr relative to β -CsBr

is a result of the fact that the ions in α -CsBr are eight-coordinated and those of β -CsBr six-coordinated, and thus the sum of dipole-dipole interactions are larger in the former.

It was not considered necessary to recalculate CRYSTAL09 calculations with the inclusion of the D2 or D3 correction, but the PBE + D2 functional has been used in for bulk CsBr calculations in Chapters 6 and 7 and some CsBr/Cu calculations in Chapter 7, where accurate estimates of the work function and similar properties are known to be highly sensitive to the interfacial distance between Cu and CsBr.

3.2.3 Topology of CsBr Grown on LiF, KBr and Cu Substrates

The caesium halides are unique among the alkali halides in adopting the CsCl-type body-centred cubic structure (α -CsBr) at room temperature. The rocksalt face-centred cubic phase (β -CsBr) is however energetically very close to the ground-state structure. The coexistence of two energetically close phases opens up the possibility of selectively growing CsBr films of a particular phase by suitable choice of epitaxial frame. Experiments conducted in parallel with both α - and β -CsBr give insight into the effect of structure on the characteristics of the films, such as radiation hardness, and provide an opportunity to investigate how defects such as excitons are influenced by differences in structure. Calculations conducted in Chapters 5, 6 and 7 have been conducted in order to simulate films grown on the LiF(100), KBr(100) and Cu(100) surfaces. The scarcity of direct experimental evidence as to the surface structure of the MBE-grown films necessitates a review of the literature in order to gain insight into their structure, and inform theoretical models which attempt to represent these real films.

Experiments of CsCl deposited on MgO(100) at various temperatures[1] have observed the coexistence of α (110) and β (100) islands which becomes a series of α (110) terraces at thicknesses between 100 and 200 Å. Initial growth is Volmer-Weber type, with growth of individual islands predominating. Figure 3.2 shows Atomic Force Microscopy (AFM) images of the films in early and late stages of growth (films of nominal thickness of 15 Å and 150 Å, respectively).

The initial growth, depicted in (a), reveals small islands aligned in stripes of (110) orientation, suggesting α -type growth and scattered square and rectangular islands, suggesting rocksalt β -type growth. After deposition of 15 nm films, Figure 3.2(b) clearly shows the preponderance of wholly α terraces aligned in the (110) direction.

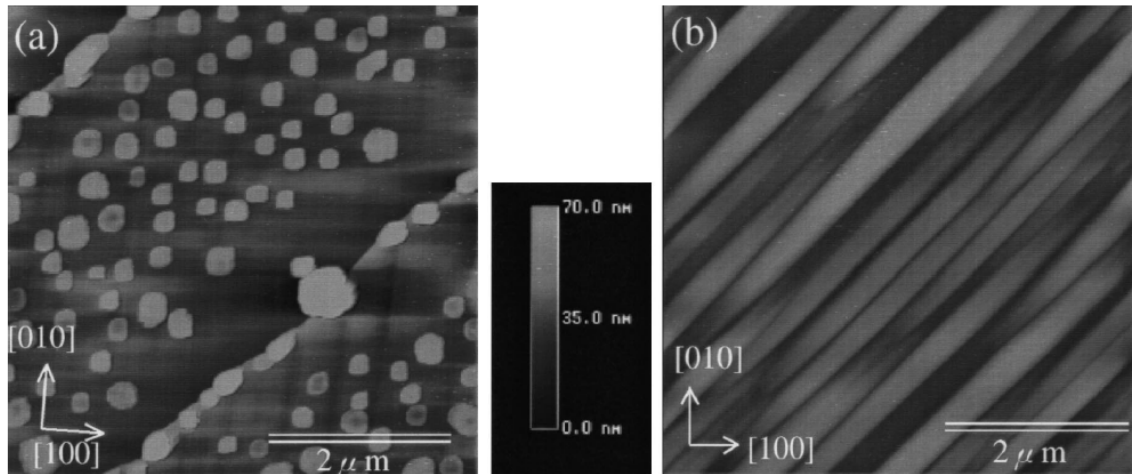


Figure 3.2: AFM images of (a) 15 Å films showing island type growth, containing both rectangular terraces and stripe-like formation running in the (110) direction and (b) 150 Å films homogeneously stripe-like terraces in the (110) direction. Images taken from Ref[1]. Copyright of Elsevier.

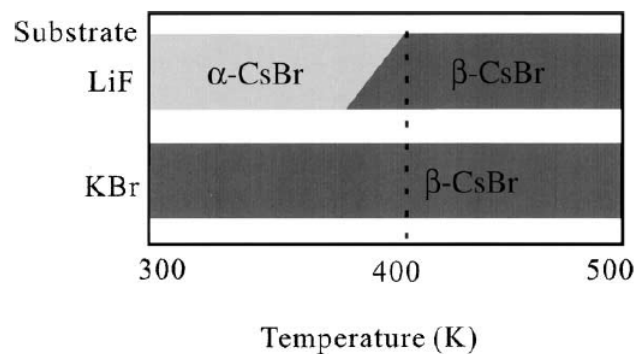


Figure 3.3: The phase diagram of the CsBr film as a function of the substrate temperature during the growth. Figure taken from Ref[2]. Copyright of IoP.

A more recent study has shown that α - and β -CsBr can be selectively grown by choice of epitaxial frame and variation of annealing temperature[2]. The growth of CsBr on both LiF(100) and KBr(100) has been examined by Reflection High Energy Electron Diffraction (RHEED) experiments, which reveal growth to be $\alpha(110)$ on LiF(100), until films are annealed at around 400 K, when the diffraction pattern changes to well-defined spots indicating homogenous $\beta(100)$ growth. The relatively sharp spots suggest that the $\beta(100)$ films are less rough than the $\alpha(110)$ films.

The growth of $\beta(100)$ on KBr was in contrast layer-by-layer throughout. At 300 K, growth was $\alpha(110)$ and $\beta(100)$ on the LiF(100) and KBr(100) surfaces, respectively. That LiF is predominantly α -CsBr and KBr β -CsBr is confirmed by Electron Energy Loss Spectroscopy (EELS). The EELS results suggest the surfaces are relatively clean,

as defect levels would otherwise be present in the spectrum. A phase diagram of the CsBr films grown on both substrates as a function of temperature is depicted in Figure 3.3.

3.3 Discussion

The increase in HF exchange in both the PBE0 and B3LYP functional increases the calculated bulk α -CsBr one-electron band gap in a roughly linear fashion over the small range investigated (approximately 20–40%). The lattice parameter by contrast varies very little. Calculated values of the bulk modulus and cohesive energy are in good agreement with experimental values.

The relatively sparse basis set used for calculations in Chapter 5 in CRYSTAL09 appears to be insufficient for some purposes. Although a number of properties have been calculated in order to test the basis, including the polarisation (high-frequency dielectric constant), ionisation potentials and electron affinity of the Br atom (see Methodology section of Chapter 5), some properties are not correctly reproduced, and the lattice parameter, although within 2% of the experimentally measured value, which is the commonly accepted DFT-limit of accuracy, is far off that calculated with a fully converged plane-wave basis set in VASP. In particular the (bulk) exciton luminescence energy is severely underestimated by this model (by approximately 1.5 eV), whereas other models are all within approximately 0.1 eV from the experimental value. This fact is consistent with the notion that the CRYSTAL09 basis sets are not spanning the interstitial space sufficiently well to describe some excited states, but are sufficient for most calculations in the ground state. Nonetheless the model has been successfully used to calculate excitons and F-centres at CsBr surfaces, and calculations are very close qualitatively and quantitatively to those calculated using the other models, as well as being in good agreement with experiment (see Chapter 6.4.1).

Experimental evidence strongly suggests that CsBr grown by MBE techniques on LiF(100) and KBr(100) in the temperature range of ~ 300 K should produce α (110) and β (100) surfaces. As the lattice mismatch between Cu(100) and β -CsBr is very small, smaller than for the KBr(100) case, and that with α -CsBr is large, we also assume that CsBr grown in this temperature range on the Cu(100) surface should produce the β (100) surface.

Chapter 4

Theoretical Modelling of Point Defects in CsBr

The aim of this chapter is to conduct calculations of vacancies, interstitials, trapped holes and self-trapped excitons in bulk α -CsBr. The geometry of each defect is detailed, as well as estimates of the migration barriers. Calculations of the optical absorption spectrum of each defect have been conducted using TD-DFT. The calculations are compared with experiment, with particular attention paid to explanation of the optical absorption spectrum, from which the accuracy of the TD-DFT techniques and model used can be gauged.

4.1 Introduction

Although the literature on point defects in the alkali halides is extensive, with Marshall Stoneham's seminal book (published in 1975) summarising their fundamental properties[111], most calculations contained have been conducted using classical or semi-classical methods. Moreover, point defects in the caesium halides, in contrast to the rocksalt alkali halides, are comparatively less well studied and understood. Although there exists substantial experimental results (e.g. for vacancies[112, 113, 114], holes[115], interstitials[3], and excitons[115, 116, 117]), there are very few theoretical calculations. With recent advances in computational power, it has become feasible to calculate these defects using DFT methods with hybrid functionals, and therefore calculate accurate quantitative results for their fundamental properties.

CsBr, as CsCl and CsI, adopts the so-called CsCl-type structure at room temperature: a body-centred cubic structure where each anion is surrounded by eight cations

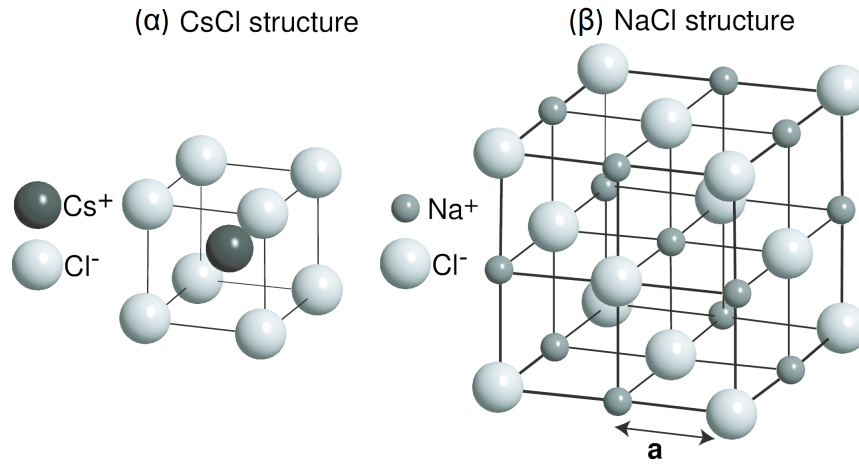


Figure 4.1: The CsCl-type structure and NaCl-type structures, α - and β -CsBr, respectively.

at the corners of a cube, and vice versa (see Figure 4.1). The geometry and diffusion behaviour of the fundamental defects of the caesium halides are therefore qualitatively different to the rocksalt alkali halides.

The economic feasibility of CsBr-based photocathode materials is crucially dependent on their behaviour and degradation under UV irradiation, but an understanding of radiation hardness of CsBr has much wider applications. For example, radiation damage causes loss of Eu^{2+} luminescence in $\text{CsBr}:\text{Eu}^{2+}$ storage phosphors[118]. Experimental observation of the QE of CsBr-Cu photocathodes has observed an activation period after initial radiation, typically lasting a number of hours, during which the QE steadily increases, until reaching a considerably larger equilibrium value. This effect has been attributed to defect creation at and around the interface[54, 57], but which defects, the mechanisms by which these defects are either created or diffuse towards the interface, and how they act to reduce the work function remains all remain unanswered questions.

The use of hybrid functionals allows for considerably more accurate description of the electronic structure, in particular, the band structure of large band gap insulators with respect to well established GGA-type functionals. The use of a hybrid functional description in conjunction with TD-DFT methods therefore allows accurate prediction of the optical properties of such point defects in insulators, (see e.g. Refs. [119, 120, 121]). As the defects have been examined experimentally, their spectroscopic properties are well established. As such, calculations of these defects not only give insight into the defects and their behaviour and properties, but also provide a test-bed for assessing

the accuracy of current state-of-the-art modelling methods.

The aims of this chapter are three-fold: to provide a comprehensive overview of the defects of CsBr and present them side-by-side, to assess the accuracy of current state-of-the-art modelling methods with regards to optical properties of large band-gap insulators, and to provide the foundations towards an analysis of defect behaviour at and around the CsBr-Cu interface.

This remainder of this chapter presents results of the geometry, migration behaviour and optical response of Br vacancies (F-centres), self-trapped holes (V_k -centres), interstitial ions (H- and I-centres) and self-trapped excitons, and finally the results of the theoretical calculations are assessed with comparison with experimental data.

4.2 Modelling Bulk α -CsBr: Embedded Cluster Approach

All calculations have been conducted in a mixed QM/MM embedded cluster model using the GUESS code[122, 123]. The embedded cluster model has the advantage over periodic model calculations of not requiring finite-size corrections in order to correct for spurious interactions of the point defects with repeated defect images and a compensatory background electric field. This is of particular convenience with the charged defects investigated here, where an accurate vacuum energy allows calculation of the electron affinities and ionisation potentials. The embedded cluster model also allows long-range relaxation to be taken into account with negligible increases in computational cost. In addition, the GUESS code allows for the use of TD-DFT calculations as implemented in the Gaussian code[124], which are considerably more complex to calculate in periodic models. In order to simulate the bulk crystal, a large nanocluster of 62 500 atoms has been generated, and surrounded by a thin skin of point charges positioned so as to replicate the Madelung potential of the perfect crystal. The number and arrangement of atoms and point charges in this ensemble were chosen such that the on-site electrostatic potential within a sphere of radius 15 Å at the nanocluster centre fluctuated from the correct Madelung potential of the infinite crystal by less than 1 meV (see section 2.3.2). The details of this procedure are published

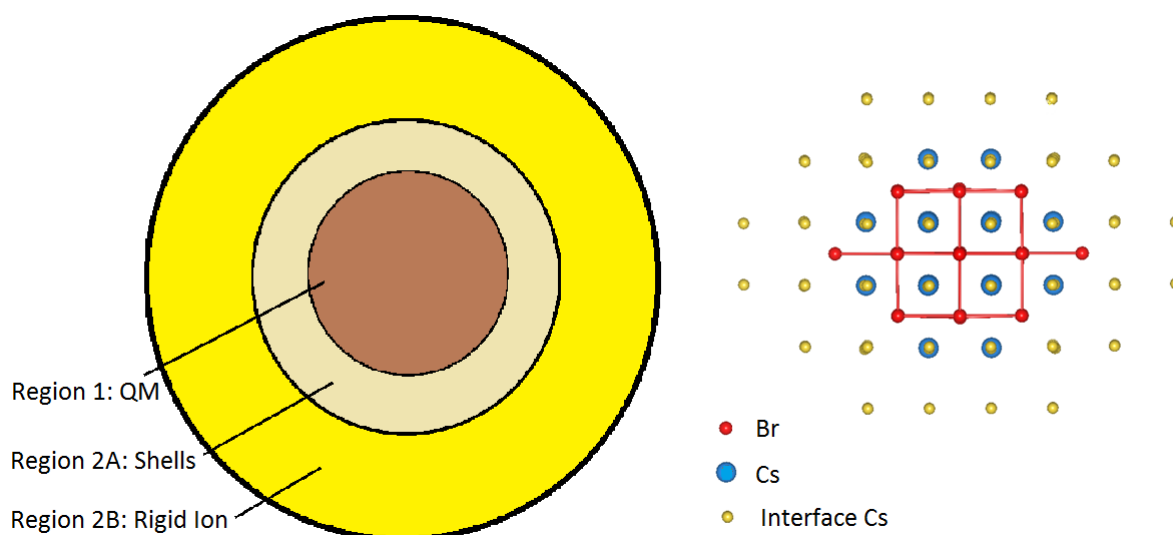


Figure 4.2: The partitioning of the nanocluster into different regions and the $\text{Cs}_{32}\text{Br}_{31}$ cluster with interface ions. Note that the relatively small radius of the interface cations is drawn to aid the eye rather than to reflect physical difference in ionic radius.

elsewhere[125, 126, 127].

The nanocluster was divided into two regions, and is depicted in Figure 4.2. Region 1 is described in a fully *ab initio* quantum mechanical manner, with pseudopotentials and Gaussian basis sets centred on the ions. This region is then surrounded by a layer of interface cations, with large-core Stuttgart pseudopotentials[128] centred on them, which serve to keep the quantum electron density confined to Region 1, and act as atoms mediating between the quantum and classical region. A profile of a $\text{Cs}_{32}\text{Br}_{31}$ cluster used in the study with surrounding interface cations is depicted on the right of Figure 4.2. The interface atoms and the ions in Region 1 are embedded within Region 2, which is further subdivided into Regions 2A and 2B. Region 2A is modelled using a polarisable core-shell model, with interatomic pairwise potentials describing the forces between the atoms. The cores and shells in this region are able to relax, such that they can be polarised, and therefore approximate the classical response of a dielectric medium, in order to correctly the local electric field surrounding the defect. Region 2B consists of fixed, non-polarisable classical atoms. The system total energy is then minimised simultaneously with respect to the electronic coordinates and the positions of the QM and classical ions.

The electronic structure of the quantum region has been described using a modified version of the B3LYP hybrid functional[71, 75]. This was deemed necessary in order to

correctly describe the position of the defect levels within the gap and to obtain accurate exciton energies. The amount of HF exchange included in the functional was increased to 32.5% from the standard 20%, a procedure justified in Chapter 3. Increasing the amount of HF exchange in existing hybrid functionals in order to correctly produce the band gap has become common procedure[129, 130, 131], and is justified more extensively in Chapter 3. The cores of the anions and cations in Region 1 were described using small-core Stuttgart pseudopotentials, leaving the Br^- $[(\text{Ar})3s^23p^63d^{10}]4s^24p^6$ and Cs^+ $[\text{Ne}]4s^24p^65s^0$ electrons to be described by $6s6p1d/4s4p1d$ and $4s5p1d/2s3p1d$ basis sets, respectively[132].

A $\text{Cs}_{32}\text{Br}_{31}$ cluster (see Fig. 4.3) was used to study all defects excepting the V_k - and I -centres, where a larger $\text{Cs}_{40}\text{Br}_{38}$ cluster was used to accommodate the D_{4h} symmetry.

The lattice parameter was calculated as 4.336 Å, within 2.1% of the experimental value (4.295 Å[133]). The difference in energy between the HOMO and LUMO eigenstates for the $\text{Cs}_{32}\text{Br}_{31}$ and $\text{Cs}_{40}\text{Br}_{40}$ clusters are 7.51 and 7.49 eV respectively. A two-photon absorption spectroscopy study has determined 7.20 eV as the lower bound for the difference in energy between the valence band to conduction band transition ($\Gamma_8^- - \Gamma_6^+$)[134]. CsBr has a negative electron affinity of 0.9 eV[50], which is underestimated slightly (~ 0.2 eV) in both models. Large-core Stuttgart pseudopotentials were placed on interface cations[132].

The forces in Region 2 were described using the Atwood Buckingham potentials[135], which give a lattice parameter of 4.295 Å. The small discrepancies in the quantum and classical lattice parameters did not give rise to large distortions of the geometry when relaxed. The system was then relaxed until the energy, ionic displacement and forces on each species per step become smaller than 10^{-6} , 0.0003 Å and 0.03 eV Å⁻¹, respectively.

4.3 Defects in CsBr: Geometry

4.3.1 F-centres

The most commonly observed and investigated point defect in the alkali halides are anion vacancies, or F-centres. A neutral F-centre, or F^0 -centre, is an anion vacancy with a single electron, such that the defect has neutral formal charge. It has been

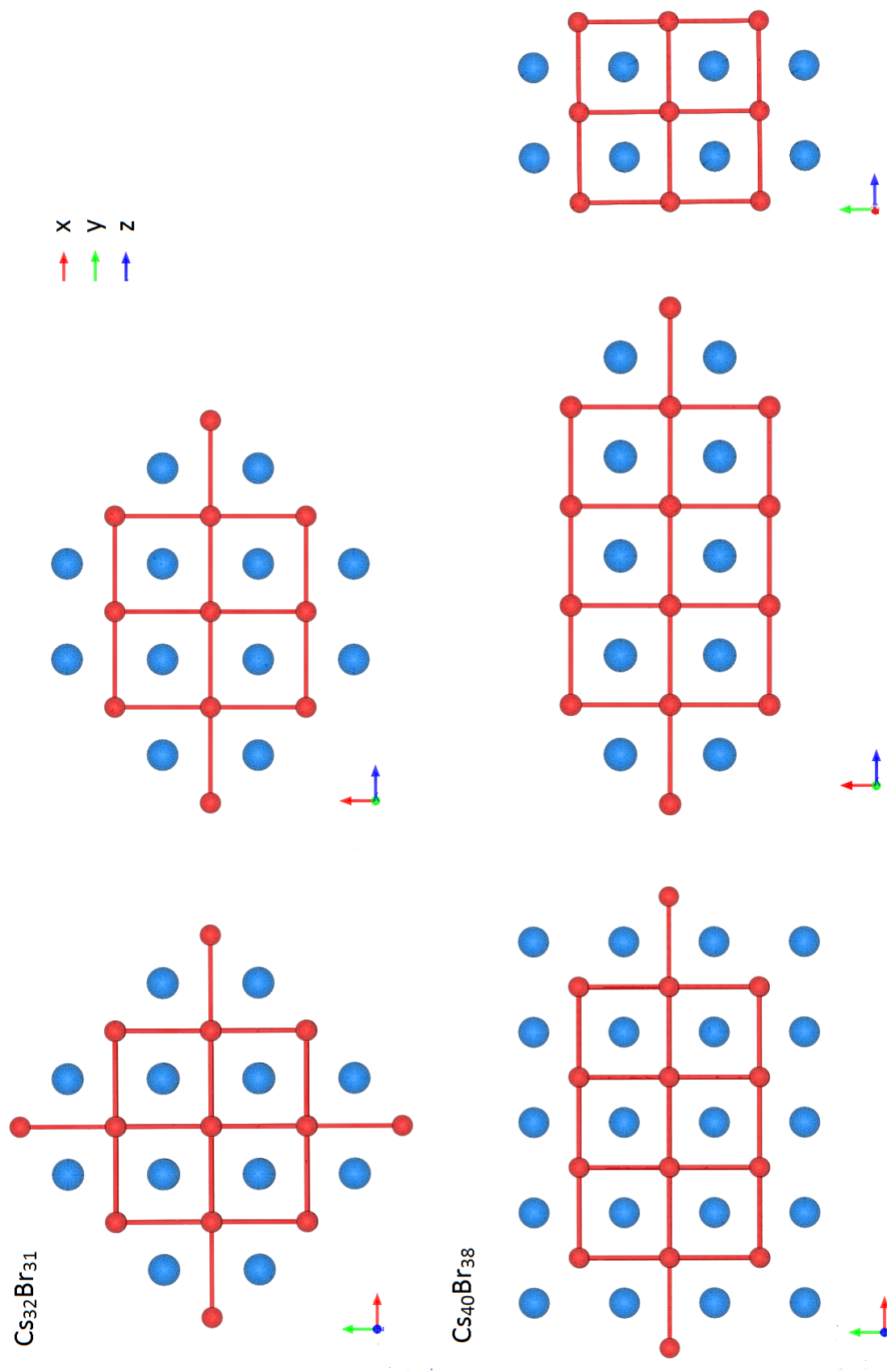


Figure 4.3: The $Cs_{32}Br_{31}$ and $Cs_{40}Br_{38}$ clusters shown from all non-identical projections. The figure above depicts the x-y and x-z (which is identical to the y-z) planes of the $Cs_{32}Br_{31}$ cluster. The figure below depicts the x-y, x-z, and y-z planes of the $Cs_{40}Br_{38}$ cluster. Note that the anions and cations are sitting in mutually exclusive planes. Anions are depicted in blue, cations in red.

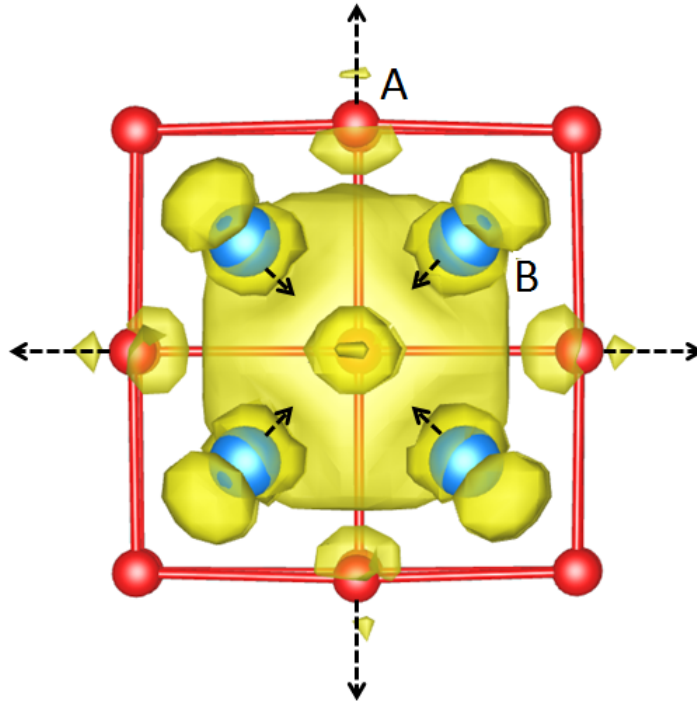


Figure 4.4: A plot of the spin density distribution of an F^0 -centre. The isosurface is set to a value of 0.001. The arrows on the diagram indicate movement direction of the ions in the case of an F^- centre, where the length of the arrow is approximately proportional to the magnitude of displacement. For the F^+ -centre directions of displacement are reversed. Br anions are depicted in red, and Cs cations in blue.

modelled by removing a Br anion from the centre of the cluster and placing a ghost basis set, identical to that on the anions, at the defect site. The ionic coordinates were then allowed to relax, although movement of the ions was negligible. A spin density plot of the defect is depicted in Figure 4.4.

The electron occupies a new state in the band gap, 2.7 eV below the conduction band maximum (CBM) of the defect-less cluster. A natural population analysis[136] reveals that the state is mainly composed from the surrounding 8 Cs $6s$ orbitals, $(0.52|e|)$, with a small contribution from the vacancy $1s$ orbital $(0.13|e|)$. The energy of the F^- centre is 0.1 eV lower with the vacancy “ghost” basis set than without the extra basis.

An F^- -centre (or F' -centre) is an anion vacancy with two electrons. The defect is negatively charged with respect to the lattice, causing the neighbouring Cs cations to relax towards the defect, and neighbouring Br anions to relax away. The state in the band gap is doubly occupied, and due to Coulombic repulsion between the two electrons, the energy of the state rises. The displacements of the neighbouring ions are displayed in Table 4.1, with the direction of displacements indicated in Figure 4.4.

	A (Å)	B (Å)	Energy level (eV)
F ⁺	0.22	0.19	2.1
F ⁻	0.27	0.02	0.5

Table 4.1: The total displacements of the nearest neighbour Br anions (A) and Cs cations (B) with respect to their perfect lattice sites as a result of F-centre formation. Directions of displacements are indicated in Figure 4.4. The positions of the defects states within the band gap are given with respect to the CBM.

An F⁺-centre (or α -centre) is an anion vacancy without any trapped electrons, such that it is positively charged with respect to the ionic lattice. The effective positive charge induces relaxation of the neighbouring anions and cations in the opposite directions to the F⁻-centre, (see Table 4.1). As a result of relaxation the unoccupied vacancy state is shifted upwards towards the CBM, to a smaller extent than in the F⁻ case, and the hole delocalises.

4.3.2 V_k-centres

The V_k-centre is a polaronic trapped hole defect. The hole becomes self-trapped by inducing the formation of a pseudo-Br₂⁻ molecular ion, such that the hole sits in an anti-bonding antisymmetric σ -type orbital constructed from the 4p orbitals of the Br ion polarised along the molecular axis. Calculations of the Br₂⁻ molecular ion electron affinity and ionisation potential in the vacuum have been conducted in Chapter 5, where calculations suggest, in agreement with experiment, that the molecular ion is stable (see Table 5.2 and following discussion). The defect has been modelled by the removal of an electron from the system and displacement of the anions, so as to encourage localisation of the hole. The system has then been allowed to relax under the influence of forces. The energy gained due to relaxation is 0.6 eV. The defect molecular ion is spread across two lattice sites, with the axis aligned along the (100) direction, such that the defect has D_{4h} symmetry. The local geometry of the V_k-centre is displayed in Figure 4.5, with the magnitude of displacements of the neighbouring ions in Table 4.2.

The defect induces the localization of two electrons into a σ_g symmetric bonding orbital with energies that lie within the valence band, and a higher energy singly occupied σ_u antibonding state within the gap.

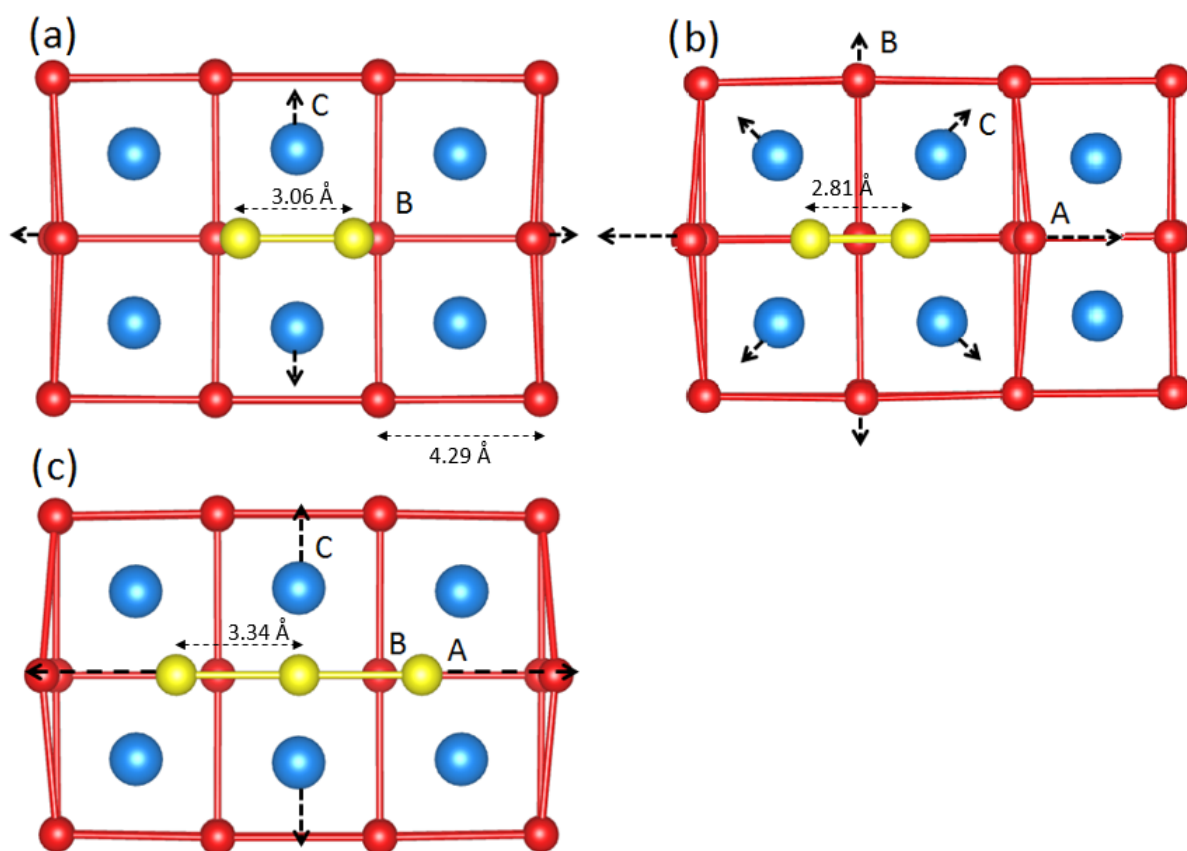


Figure 4.5: The local geometry of (a) the V_k - (b) H- and (c) I-centres. The magnitude of displacement is proportional to the length of the arrows. Cs cations are depicted in blue, Br anions in red, and the defect Br anions in yellow. Note the figure displays two vertical planes containing Br anions, and a single plane containing Cs cations bisecting the two anionic planes.

	r_e (Å)	A (Å)	B (Å)	C (Å)
H	2.81 (65% a_0)	0.47	0.06	0.03
V_k	3.06 (71% a_0)	0.13	0.31	0.11
I	3.34 (78% a_0)	0.52	0.06	0.22

Table 4.2: The displacements of the nearest neighbour Cs cations and Br anions with respect to their perfect lattice sites as a result of the defects. The direction of displacements are indicated in Figure 4.5. The label r_e refers to the intermolecular separation of the Br_2^- molecular ion, or the Br_3^- ions in the case of the I-centre, and a_0 to the lattice parameter.

4.3.3 H- and I-centres

An H-centre is a neutral interstitial Br atomic defect, which, similarly to the V_k -centre, forms a pseudo Br_2^- molecular ion occupying a single lattice site. Irradiation of CsBr at above band-gap energies creates a large number of F-H Frenkel pairs[137], that is, vacancies (F-centres) and interstitial atoms (H-centre). The molecular axis is oriented in the (100) direction, and the defect induces a large distortion of the local geometry, (see Fig. 4.5(b) and Table 4.2). The defect induces the localisation of two electrons into bonding σ_g orbitals lying in an energy level in the band gap, and a single electron occupying a higher σ_u orbital also within the band gap.

The I-centre is a negatively charged interstitial ion. I-centres are created with α -centres (also known as the F^+ -centre) after excitonic relaxation or tunnelling of electrons from F- to H-centres, or following electron capture by an H-centre[3]. Whereas the symmetry of the V_k - and H-centres have been established by experiment[138, 139] and modelled classically, that of the I-centre is unknown. The I-centre has been calculated in both the interstitial configuration (as in Fig. 4.5(c)), and as a pseudo Br_2^- molecular ion centred on a lattice site, similar to the geometry of the H-centre, with the interstitial configuration lower in energy by approximately 0.04 eV. In the interstitial configuration the I-centre is manifested as a pseudo- Br_3^- molecular ion, with the HOMO states being formed from along-axis $4p$ orbitals of the three Br ions, and having odd parity. The displacements of surrounding ions due to the defect are even larger than the H-centre, (see Table 4.2).

The defect induces localisation of two electrons into an orbital shared between the pseudo- Br_3^- ions, which lie at an energy within the band gap.

4.3.4 Self-trapped Exciton

Excitons are quasiparticles, bound states between an electron and hole, that can become self-trapped in a polaronic manner[140]. A TD-DFT calculation of the lowest energy transition of the bulk finds the first peak occurring at 6.65 eV, close to the experimentally observed first exciton peak at 6.8 eV[134], which corresponds to excitation of an electron moving in the valence band into the bottom of the conduction band. These electron-hole pairs can trap and form excitons. The electron is forcibly confined to Region 1 which will act to increase the estimated energy of this transition in the embedded

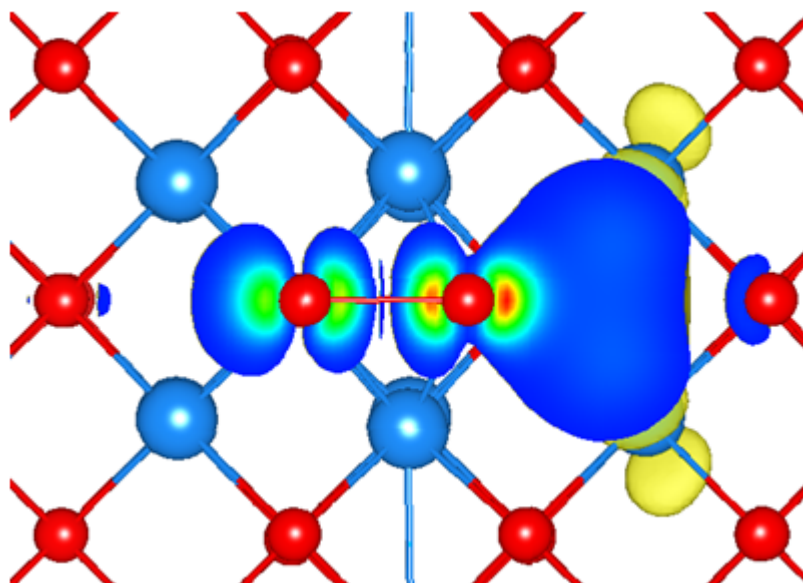


Figure 4.6: The spin density (isosurface = 0.001) of an off-centre triplet exciton. The spin density increases from red to blue. The proto F-centre is on the right, with the lobes of the hole orbital visible on the adjacent proto H-centre. The Br anions are depicted in red, and the Cs cations in blue. Note the figure displays two vertical planes containing Br anions, and a single plane containing Cs cations bisecting the two anionic planes.

cluster model. As a result the underestimation is unexpected.

Both singlet and triplet excitons are known to exist in CsBr, and the triplet state is lowest in energy[116]. Indeed, this is always the case for any cubic compounds, and is discussed in further detail here[141]. The triplet exciton has been modelled by perturbing a Br ion from its lattice site, so as to create a nascent vacancy for an electron to localise in, specifying the spin state of the system as triplet, and allowing the ionic coordinates to relax under the influence of forces. This method of modelling the triplet exciton using ground-state DFT methods has been used in other alkali halides and oxides[142, 143, 125]. This was necessary as the use of TD-DFT to calculate forces is unavailable in Gaussian03, which has been interfaced with the GUESS program and used to model Region 1.

An electron localises in the proto-vacancy and the displaced Br ion moves in the (100) direction towards a Br anion neighbour, such that the hole localises on two anions, forming a proto H-centre. This is referred to in the literature as the off-centre configuration[140]). A plot of the spin density, showing both the electron and hole components of the exciton, is displayed in Figure 4.6.

The total energy of the system in the relaxed geometry is 6.1 eV higher than the

perfect, unperturbed lattice (in the singlet state), suggesting that there is a gain in energy of approximately 0.55 eV due to localisation, relaxation and polarisation of the surrounding lattice, with respect to the original unperturbed nuclear geometry, as 6.65 eV has been estimated above as the first exciton energy. That is, the difference in energy between the bottom of each potential well illustrated in Fig. 3.1 is 6.1 eV. The net formation energy of an F- and H-centre at infinite separation from each other is calculated as 6.4 eV, such that the relaxed off-centre exciton is lower in energy by 0.3 eV. Consequently, these calculations predict that there is a small energy barrier for self-trapped exciton to separate into F-H pairs.

The position of the maximum of the triplet self-trapped exciton luminescence energy has been estimated by calculating the difference in energy between the relaxed triplet exciton and the system in a singlet state in the geometry of the relaxed off-centre triplet state, as an adiabatic “vertical” transition, (see Fig. 3.1). The calculated energy of 3.6 eV is very close to the observed luminescence energy of 3.54 eV, such that the Stoke’s shift is calculated as $(6.6 - 3.6) = 3.0$ eV.

4.4 Defects in CsBr: Migration

The adiabatic barriers to diffusion for each of the defects have been estimated by assuming the trajectory of motion. The NEB methods were not used as they are not implemented in the GUESS code, however due to the symmetry of the system and defects, the barrier points estimated here should approximate the results of NEB calculations quite well. In the case of the F-centres, motion is in the (100) direction by symmetry. The barrier has been estimated by moving a neighbouring anion towards the defect site in increments of 0.05 Å, fixing the coordinates of the ion and allowing all other ionic coordinates to relax, such that the energy of the system is calculated at each step. As Regions 1 and 2A are surrounded by the fixed Region 2B atoms, all atoms do not move in concert towards the ground state, as would be the case when adopting a similar strategy in a model employing PBCs. The barrier is then estimated as the difference between the highest energy point along the trajectory and the energy of the F-centre ground state. In the cases of the V_{k^-} and H-centres, the direction of motion has been established to be in the (100) direction by experiment. By extension this has been assumed to be the case for the I-centre also. The x-coordinate of one of the defect

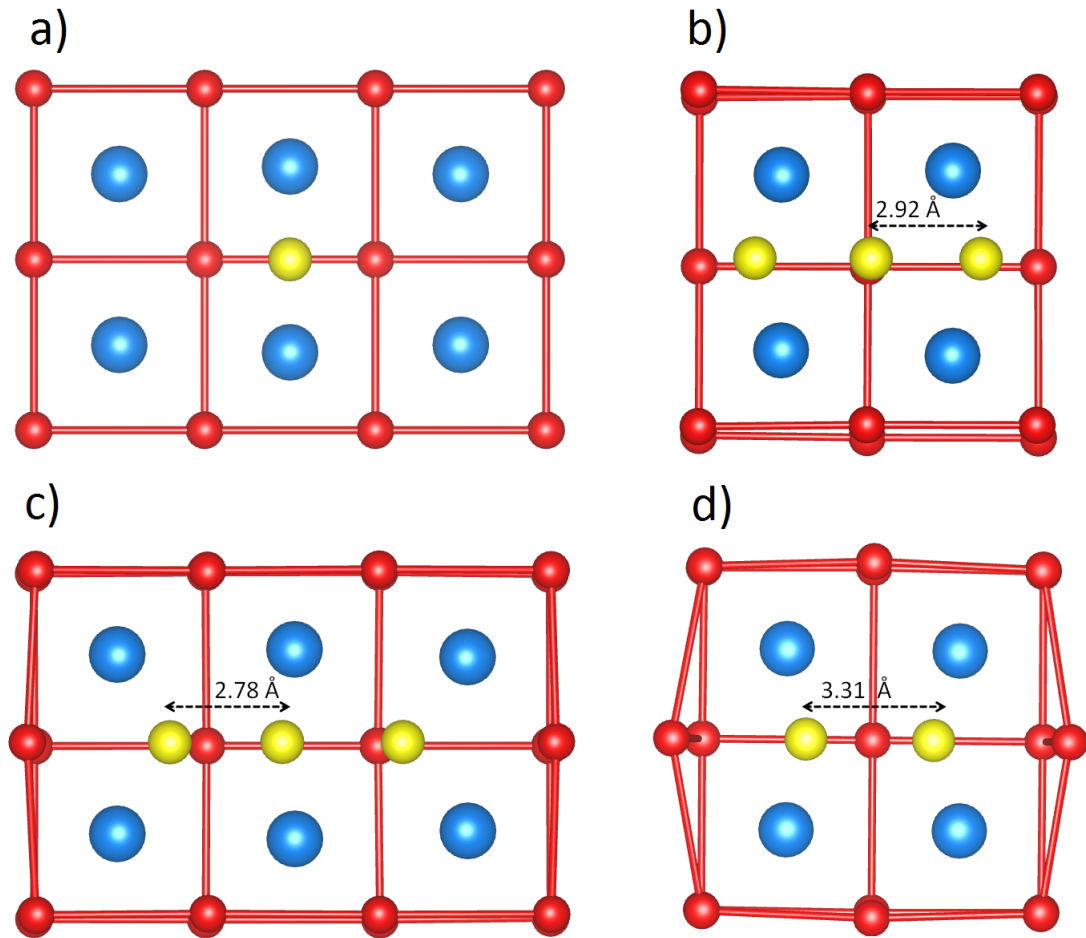


Figure 4.7: The local geometry of a) the F-centre, b) the V_k -centre, c) the H-centre and d) the I-centre at the the highest energy point along the diffusion trajectory (barrier point). The ions in yellow are those of the defect, with all other Br anions depicted in red, and the Cs cations in blue.

Br ions has been incremented in the (100) direction and fixed, with all other ionic coordinates allowed to relax. Again, the barrier to motion has then been estimated as the difference in energy between the highest energy point along the diffusion pathway and the energy of the defect in the ground state. The local geometry of the defects at the barrier point are illustrated in Figure 4.7, and the estimates for the diffusion barrier are displayed below in the right-hand column of Table 4.3.

4.4.1 F-centres

The calculated barrier of 1.0 eV is in agreement with the experimental observation that F-centres are largely immobile and is comparable to estimates of the neutral F-centre diffusion barrier in other (rocksalt) alkali halides[144]. The F^- -centre has an even larger barrier again (1.15 eV). As the motion involves delocalisation of two electrons

instead of one, this is in line with expectation. The F^+ -centre by contrast has a much reduced barrier of 0.3 eV, such that they are expected to be mobile at low temperatures (~ 150 K).

4.4.2 V_k -centres

V_k -centre motion in the caesium halides is predominantly linear and in the (100) direction, from the Br_2^- configuration of Figure 4.5(a) to a pseudo Br_3^- ion at the saddle point height (see Figure 4.7(b)), although 90° rotations are also observed[145, 146, 147]. Motion proceeds in a ballistic, so-called ‘‘crowdion’’ fashion (see Ref. [148] for a more detailed explanation). The hole in the V_k -centre ground state lies 1.6 eV below the CBM, so hot-hole migration, a feature of other alkali halides such as KBr[149], is not predicted. An experimental study has established the threshold temperature of V_k -centre motion to be around 130 K, from which a value of 0.22 eV is extrapolated as the adiabatic barrier, close to the value calculated here (0.25 eV). Previous studies which have sought to model the defect classically found a smaller barrier to rotation than linear migration, which is contradicted by experiment[147]. Here, with a quantum mechanical description, the theoretical linear migration estimate is close to the experimentally extrapolated value.

4.4.3 H- and I-centres

H-centres are known to diffuse freely at room temperature, and their motion has been established experimentally to be predominantly in the (100) direction[116], such that the configuration at the barrier resembles a proto Br_3^- molecule (see Fig. 4.7(c)). The calculated migration energy of 0.02 eV predicts that H-centres should become mobile around 15 K, and as such be mobile at room temperature and at liquid nitrogen temperatures, which is observed[3]. This is in good agreement with the barrier to thermal motion estimated in previous pulsed radiolysis experiment (0.035 eV)[150].

The motion of I-centres has not been observed or modelled. The small barrier to I-centre motion calculated here suggests that the diffusion rate should be similar to the H-centre. The geometry of the saddle point configurations for diffusion of the H- and I-centres are qualitatively the same as the ground state geometry of the I- and H-centres, respectively (c.f. Figure 4.7 (c) and (d) and Figure 4.5 (b) and (c)), and thus it is logical to suppose that I-centres also propagate in the (100) direction in a crowdion manner,

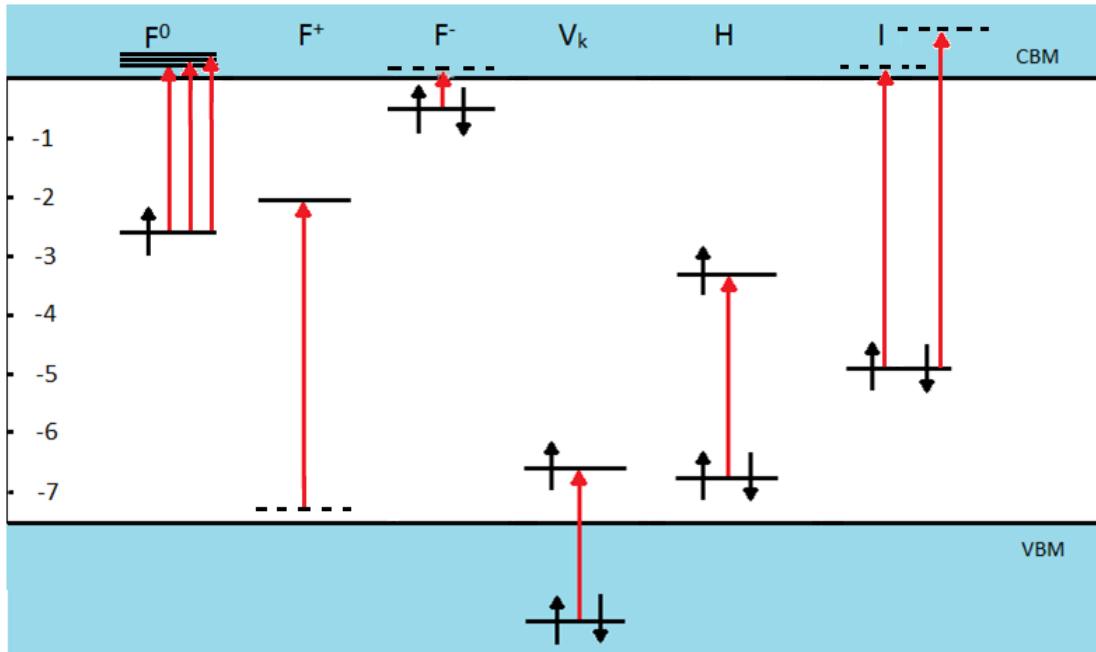


Figure 4.8: The positions of the calculated one-electron (DFT) energy levels involved in the primary optical transitions associated with the peak in the optical absorption spectrum of each defect. The dashed lines indicate semi-localised states confined to the clusters as opposed to the idealised VBM and CBM of the infinite crystal.

similar to the V_k -centre discussed above. We note that I-centre diffusion barriers have been estimated from liquid helium temperature measurements of KBr and KCl to be 0.06 and 0.09 eV, respectively[151]. Although the dynamics in CsBr is slightly different to these systems, this is close to the calculated value here of 0.04 eV.

4.5 Defects in CsBr: Optical Properties

Calculations of the (vertical) transitions corresponding to the most significant optical absorption features have been conducted for each defect. The main transitions are depicted figuratively in Figure 4.8, where the energy levels are taken from ground-state DFT calculations. As the Tamm-Dancoff approximation has been employed, all calculated oscillator strengths are unnormalised, although their relative strengths can be examined. The calculated vs. experimentally observed optical absorption peaks[152, 3, 145, 153] for all the primary defects are given in Table 4.3.

4.5.1 F-centres

The strongest peaks in the absorption spectrum of CsBr after a period of X-ray irradiation corresponds to transitions of the F^0 -centre[154, 3]. They have the strongest

	OA_{calc} (eV)	OA_{exp} (eV)	E_a (eV)
F^0	2.06	2.03[152]	1.05
F^+	5.96	6.05[3]	0.29
F^-	1.45	1.21[3]	1.14
$V_k \sigma$	3.06	3.23[145]	0.25
H_σ	2.41	2.74[153]	0.02
I	5.37	5.26[3]	0.04

Table 4.3: The calculated energies of optical absorption peaks (OA_{calc}), experimental absorption peaks (OA_{exp}) and migration barriers (E_a) associated with the primary defects.

optical absorption signature both because they are more numerous than other defects, and due to the strong overlap between the orbitals of the excited and ground state of the F^0 -centre electron. The peak is composed of three individual peaks observable at low temperature, occurring at 580, 617 and 637 nm, corresponding to energies of 1.95, 2.01 and 2.14 eV. The splitting is common to the caesium halides[152], although the origin of the splitting remains unknown, (for further discussion see Ref.[155]).

A TD-DFT calculation of the lowest energy transitions of the F^0 -centre finds three peaks occurring at 1.99, 2.09 and 2.10 eV, corresponding to transitions from the ground $1s$ -type state to a $2p$ state, that is, a state of spherical symmetry about the vacant site and a state with two p -type lobes. The twofold splitting is due to the $Cs_{32}Br_{31}$ cluster being symmetric in x and y directions, but not in z , and is thus an artefact of the embedding procedure. These calculations suggest that the F band splitting is not due to mixing with the Cs $6s$ states as has been proposed elsewhere[156].

The experimentally observed peak at 205 nm (6.06 eV) has been attributed to the F^+ -centre[3]. The peak in the calculated absorption spectrum occurs at 5.96 eV, corresponding to the transition of an electron occupying a quasi-local valence band state spread across the cluster, formed from the Br $4p$ states, into the vacant $1s$ -type state centred on the defect. As the overlap between the states is relatively small in comparison to the major F^0 transition, the overlap and oscillator strength of the transition is also relatively small, which is the reason for the relatively small experimental peak.

The peak in the experimental optical absorption spectrum at 1.21 eV has been assigned to the F^- -centre. Calculation finds a peak at 1.45 eV, corresponding to transitions from the occupied $1s$ -type states to quasi-local states composed from the Cs $6s$ orbitals and delocalised across the cluster. The transition has a slightly weaker oscilla-

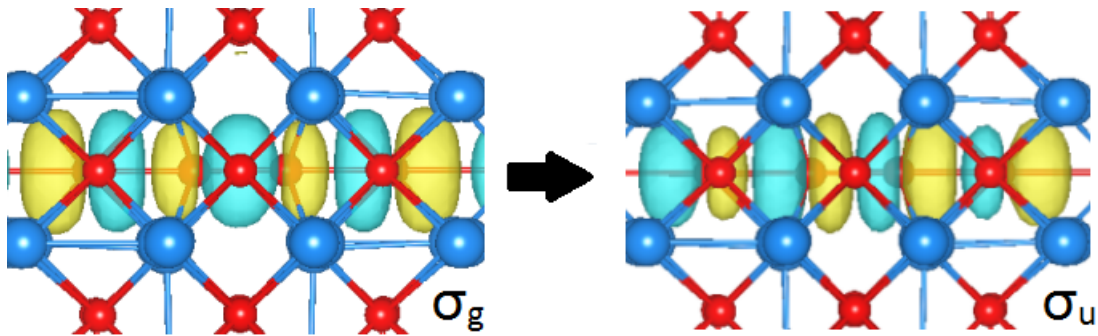


Figure 4.9: The σ_g - σ_u transition of the H-centre electron, responsible for the largest peak in the H-centre optical absorption spectrum. The yellow and blue iso-surfaces represent positive and negative value of the wavefunction, respectively. The Br anions are depicted in red, and the Cs cations in blue.

tor strength than the F^+ centre.

4.5.2 V_k -centres

The 385 nm (3.23 eV) band in the experimental absorption spectrum has been assigned to the V_k -centre[3]. The calculated absorption spectrum is dominated by one strong peak at 3.06 eV, corresponding to a transition from an electron localised on a σ_g orbital on the defect to the singly occupied σ_u state.

4.5.3 H- and I-centres

There are three peaks in the experimental absorption spectrum associated with the H-centre, two strong peaks with σ polarisation at 437 and 490 nm (2.53 and 2.84 eV), and one relatively weak one of lower energy occurring at 1 060 nm[3]. The σ polarised peaks derive from transitions from a σ_g state to the σ_u state in the band gap, illustrated in Figure 4.9. These states are split by the spin-orbit interaction[3]. A TD-DFT calculation of the hundred lowest energy transitions of the H-centre, that does not include any account of spin-orbit splitting, finds a single solution with significant oscillator strength at 2.41 eV, corresponding to a σ_g - σ_u transition. No allowed π transitions were found relating to the 1 060 nm peak.

The band at 236 nm (5.26 eV) in the experimental absorption spectrum has been assigned to the I-centre and has been observed to grow in proportion with the 205 nm band associated with the α -centre.

The calculated absorption spectrum contains two major peaks: one at 4.29 eV, and another about twice as large at 5.37 eV. The first peak corresponds to transitions

from the HOMO state derived from along-axis Br p orbitals and of odd parity, into a semi-localised conduction band state formed from the Cs $6s$ orbitals. The second peak corresponds to transitions of the electron occupying the HOMO into a state formed from Cs $6s$ and $6p$ orbitals with a large overlap with the I-centre intermolecular axis and of even parity.

The calculated optical spectra for the clusters containing the defects are displayed in Figure 4.10.

4.6 Discussion

The geometry, electronic structure and migration behaviour of vacancies, interstitials, trapped holes and excitons in CsBr have been modelled and the results presented. Both the calculated migration barriers and the calculated optical absorption peaks are in good agreement with available experimental data.

The off-centre exciton has been modelled, and the calculated estimate of the triplet luminescence energy is close to the observed experimental luminescence. The luminescence of an off-centre exciton is well known to be sensitive to proto F-H pair separation[116, 157], so an accurate estimate of the luminescence suggests that the calculated “off-centre” geometry is correct, and that the off-centre excitons predominate over any so-called “one-centre” excitons, the existence of which has been predicted in similar alkali halides[157, 158], as well as some silver halides and oxides[159, 160]. The weakly bound nature of these excitons also supports the model that exciton creation is the principal source of H-centre diffusion throughout the bulk following above band gap excitation.

The calculation of the σ transitions of the V_k^- and H-centres are also in close agreement with the experimentally observed transitions. The calculated transition energies are highly sensitive to the intermolecular separation, with the transition energy becoming smaller as the intermolecular separation becomes larger[161]. The formation energies of F-H pairs and α -I pairs, in systems where the Fermi energy is equal to the VBM, are calculated as 6.4 eV and 5.2 eV, respectively. Experiment has observed a larger presence of α -I pairs over F-H pairs at liquid helium temperature, but finds this is no longer the case at higher temperatures[162].

This has also been observed to be the case in certain rocksalt alkali halides, such

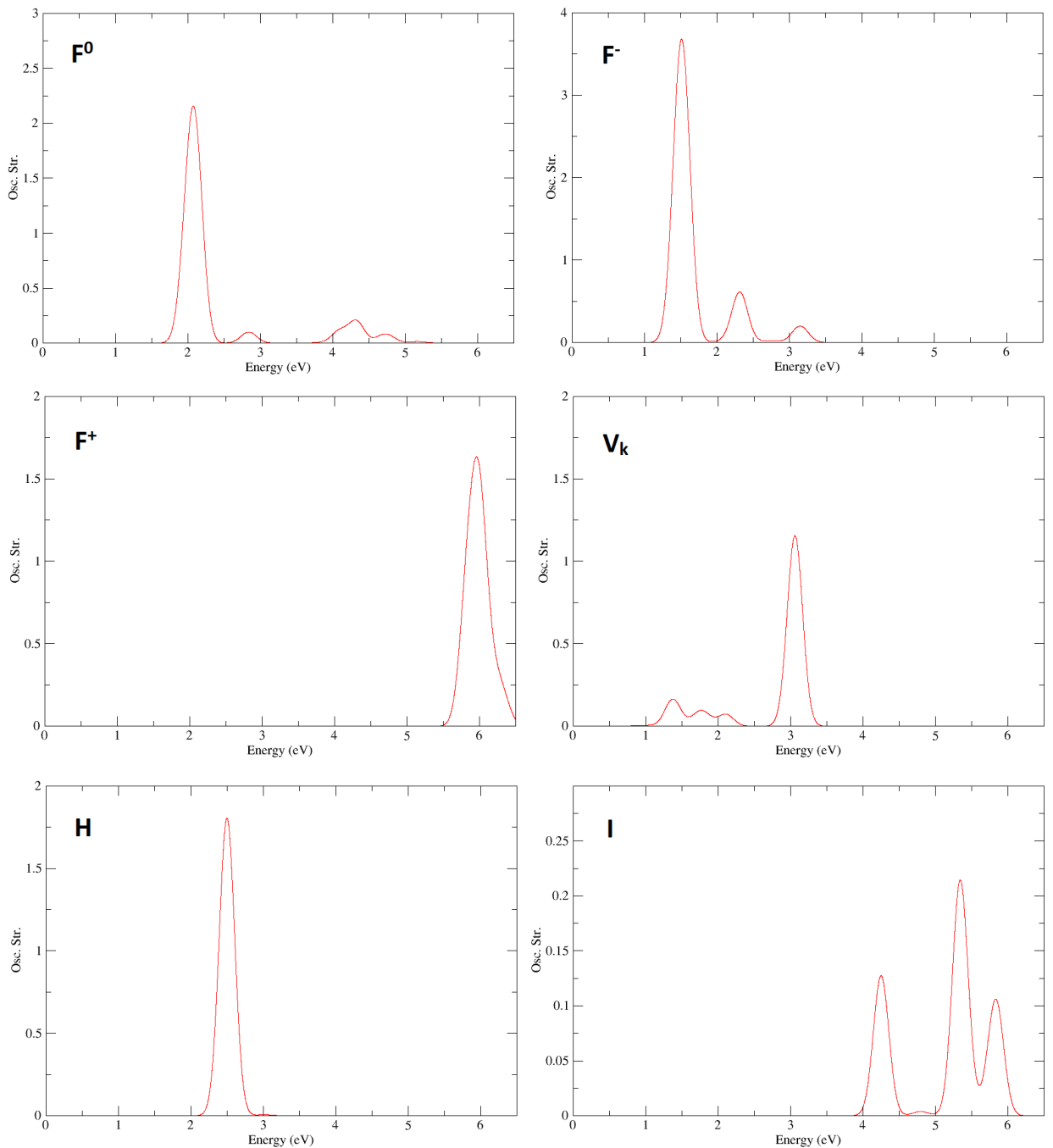


Figure 4.10: The calculated optical absorption spectra for the clusters containing each defect. In the case of the F^- , F^+ , H^- and I^- centres, the 50 lowest energy optically allowed transitions have been calculated, up unto a maximum of 6.5 eV. In the case of the F^0 -centre, the 100 lowest energy transitions have been calculated. For the V_k -centre, the 150 lowest energy transitions have been calculated, as the peak in the experimental absorption spectrum of CsBr assigned to the defect at 3.23 eV, of σ polarisation, corresponded to the 128th lowest energy transition.

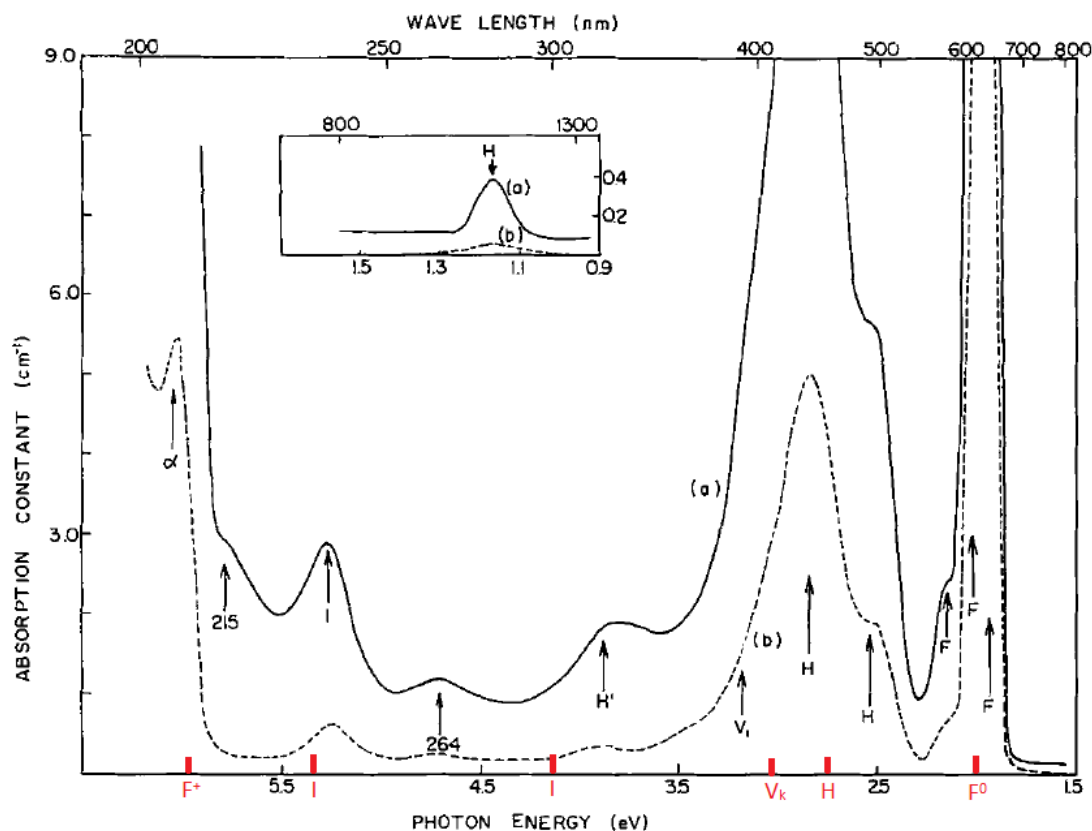


Figure 4.11: The optical absorption spectrum of liquid helium temperature CsBr after (a) 8 min of X-ray irradiation and (b) 1 min of X-ray irradiation. The red ticks on the x-axis mark the positions of the maxima of absorption for the defects as calculated in this study. Copyright of Elsevier, 1971[3].

as KBr[163, 164]. Calculated migration energies of the H- and I-centres here offer evidence that where thermal energy is available, α -I pairs will tend to transform into F-H pairs, and this suppressive reaction is predominant over electron tunnelling between the defects at high temperatures, (i.e. ~ 30 K).

Overall the agreement between the calculated TD-DFT peaks and the experimentally observed optical absorption spectrum is very good, with all calculations being within 0.3 eV of the observed peaks. The optical absorption spectrum of CsBr after X-irradiation is depicted in Figure 4.11, where the figure is taken from Chowdari et al.[3], and has been overlaid with red marks on the x-axis, indicating the positions of the calculated peaks.

The calculated peaks explain the shape of almost all of the observed spectra, with only the features believed to derive from di-H-centres, marked H' on the figure at an energy of approximately 3.6 eV, and the minor peaks at 215 nm and 264 nm which have

been tentatively assigned to impurities, remain unexplained by calculations undertaken here. The lack of an explanation of these minor peaks by the calculated defects supports the hypothesis that these features are due to impurities present within the sample. The weaker of the two calculated peaks due to the I-centre is not clearly observable, although it may be obscured by the peak at 324 nm assigned to the di-H-centre.

The V_k - and H-centres have previously been modelled as “molecules-in-a-box”, where the defects are regarded as behaving essentially as molecules, with the electrons perturbed by the electrostatic environment of the host crystal. These models have successfully predicted σ -type transitions, and have also predicted relatively weak π transitions. No π -type transitions with any significant oscillator strength have been calculated here. Previous studies have noted that the explicit treatment of next-nearest neighbour anions along the defect molecular axis improves the accuracy of calculated σ transition energies[161]. These calculations suggest that the perturbing environment of the crystal is such that the molecular model does not hold for π -type transitions, and the orbitals are perturbed to the extent that the simple model breaks down. We note that “molecule-in-a-box” models have been less successful in predicting the energy of these π -type transitions[161].

Although the reported spectrum contains a low energy peak assigned to the H-centre by the experimental group analysing the absorption spectrum (see inset of Figure 4.11), we note that the absorption constant is many orders of magnitude smaller than the other significant features in the spectrum that have been examined in this study. Moreover, the calculated V_k -centre spectrum contains low energy, small oscillator strength transitions which could be responsible for some of this signal. Analysis of the composition of the orbital contributing to these transitions reveals them to be not obviously π -like as might be expected, and are more complicated than can be explained by a simple perturbed molecular transition.

The calculations of migration energies for the F- and H-centres are in line with expectation. Due to their short lifetimes at anything but very low temperatures, there is comparatively less information available on I-centres, and contained above is the first known calculation of the I-centre in the alkali halides. Again, the largest peak in the calculated absorption spectrum is very close to the peak observed and assigned to the defect centre. The calculated migration energy, of around 0.05 eV, suggests that

they have a similar mobility to H-centres. We note that stable α -I pairs are observed at 5 K, but not at 26 K[3]. Stable α -I pairs are observed in CsCl up to temperatures of 28 K[165]. Attempts to model this barrier classically consistently overestimate this barrier to diffusion, as is also the case for V_k -centre diffusion[166]. In the rocksalt alkali halides, H-centres are oriented in the (110) direction[111], but this arrangement is often close in energy to alignment in the (111) direction. This complicates the diffusion process, and slows down H-centre diffusion in, for example, NaCl and LiF[140]. Here H-centre migration is in the (100) direction, with some 90° rotations, such that the diffusion should be a relatively efficient process.

Finally, we note that good agreement with experiment has been achieved by modelling all the primary defects using state-of-the-art hybrid functional calculations, using a modified version of the B3LYP functional with an increased proportion of HF exchange. Calculations of this type are here evidenced to be of high accuracy, high enough to correctly predict the optical properties to within a few tenths of an electronvolt for all the primary defects in CsBr. We expect a similar level of accuracy for calculations of the primary defects of other alkali halides.

Chapter 5

Thermal and Hyperthermal Desorption from α -CsBr(110) and β -CsBr(100) Surfaces

The aim of this chapter is to extend models of “thermal” and “hyperthermal” desorption from the rocksalt alkali halides to CsBr, the primary sources of thin film depletion subsequent to UV irradiation. As α - and β -CsBr can be grown by choice of suitable substrate, surface excitons and hyperthermal desorption modelled on different surfaces gives insight into the effects of structure on the hyperthermal desorption mechanism. Calculations of the motion of H-centres at and around the CsBr surface give insight into the source of thermally desorbing atoms subsequent to excitation of the bulk. Irradiation by sub band gap energies encourages preferential desorption from the CsBr surface. The calculations are compared favourably with the experimentally measured distribution of desorbing Br atom kinetic energies. This chapter is concerned with the *ab initio* modelling of CsBr surfaces, focussing on calculations supporting experimental results that provide a model of Br-atom desorption from the α (110) and β (100) surfaces.

5.1 Introduction

Excitation of alkali halide crystals by a variety of different radiation sources (electron, ion impact, laser) results in the emission of neutral halogen atoms with a distinct bimodal velocity distribution[111, 143, 140, 167, 168]. The two peaks correspond to halogen atoms desorbing with thermal and hyperthermal velocities. Excitation of these

insulators at energies above the band gap creates electron-hole pairs which can recombine to form excitons within the bulk and at the surface. Hyperthermal neutral halogen atom desorption has been shown to stem from the decomposition of a surface exciton along a repulsive potential energy surface into an F-centre at the surface and an emitted neutral halogen atom, resulting in the formation of halogen vacancies at the surface[169, 170]. Alkali atom desorption has also been observed to take place from irradiated NaCl[171], although the mechanism by which this occurs remains unknown. Alkali atom desorption shall be investigated in Chapter 6.

A self-trapped exciton in the bulk may decompose into a pair of neutral Frenkel defects: an F centre and an H-centre[140, 172]. Although F centres diffuse slowly at room temperature, H centres are known to be comparatively mobile above 25K, and can move freely throughout the crystal. H-centre diffusion towards the surface, leaving a neutral Br atom adsorbed on the surface, which subsequently thermodynamically desorbs is commonly believed to be the source of the thermal distribution peak after irradiation with above band gap energies[137, 140, 173, 172].

Calculations in Chapter 4 have estimated the (off-centre) bulk exciton energy to be lower in energy than an infinitely separated F-H pair by only 0.3 eV. The migration barriers towards F-centre desorption and H-centre desorption have been calculated as 1.05 and 0.02 eV, respectively. These calculations all support the hypothesis that self-trapped excitons can easily separate into F-H pairs in CsBr. A high barrier to F-centre migration means they should be largely immobile, H-centres in contrast can translate by linear migration through the crystal in the (100) direction, and may experience 90° rotations. The experimentally observed thermal distribution shows clear thermal dependence; as the temperature of the substrate rises so do the energies of the Br atoms with lower kinetic energies, however this is not the case for the hyperthermal component.

Photodesorption experiments on the alkali halides have shown that by carefully tuning the excitation of the surface directly, at energies above the surface exciton threshold but below the bulk exciton threshold, hyperthermal emission can be selectively induced[137, 174, 175, 176, 177]. For example excitation at 6.4 eV in KBr, near the bulk absorption threshold[178], induces efficient desorption of Br($^2P_{3/2}$) atoms, with a minor component of Br*($^2P_{1/2}$).

A number of alkali halides have been probed by laser[142, 169, 174, 179, 180,

181] and electron sources[181, 182, 183, 184, 185, 186], but to date there exists no studies for CsBr, despite its practical applications, such as a component in scintillators[187], as well as protective films for photocathodes. As discussed above, CsBr is unusual among the alkali halides in that thin films of CsBr can be grown selectively by choice of substrate that has a conducive lattice mismatch[2]. Bulk phase CsBr adopts the CsCl-type structure at room temperature (α -CsBr) whereas most of the other alkali halides adopt the rocksalt structure, (in the case of CsBr, β -CsBr). Chapter 4 has outlined the evidence that sufficiently thick epitaxial films α - and β CsBr can be grown on LiF(100) and KBr(100), respectively. Furthermore, H-centres move in the (100) direction in CsBr, whereas in most other alkali halides, such as KBr, they are in the (110) direction[116], or move in a more complicated manner, such as is the case in NaCl[188]. It is not known how these differences will affect the thermal and hyperthermal desorption dynamics, kinetic energy distributions and neutral atom yields of irradiated CsBr. Moreover, the previous theoretical simulations of desorption have been conducted using embedded cluster models, which necessarily induce localisation of electrons. Here we use hybrid functionals with a large number of atoms and a periodic model to investigate the dynamics.

This chapter presents detailed *ab initio* modelling calculations alongside ultrasensitive laser pump-probe experimental data from collaborators at PNNL to develop the framework for a surface-exciton based desorption model, and to elucidate the thermal desorption mechanism. The use of different models and functionals to model exciton relaxation at surfaces are compared and contrasted. Calculations are found to be in good agreement with experimental findings. Thermal and hyperthermal desorption from CsBr are discussed within the context of an exciton-based model.

5.2 Experimental Methodology and Results

CsBr films of thickness 7 nm (70 Å) have been grown on LiF and KBr at room temperature. Following the discussions of Chapter 3, the exposed faces should be the α (110) and β (100) surfaces, respectively, under the growth conditions here applied. The experimental apparatus in place at PNNL is depicted in Figure 5.1.

The samples are irradiated with excimer laser pulses every 5 ns of wavelength 193 and 157 nm (6.44 eV and 7.91 eV), at angle of incidence of 60° to the surface normal.

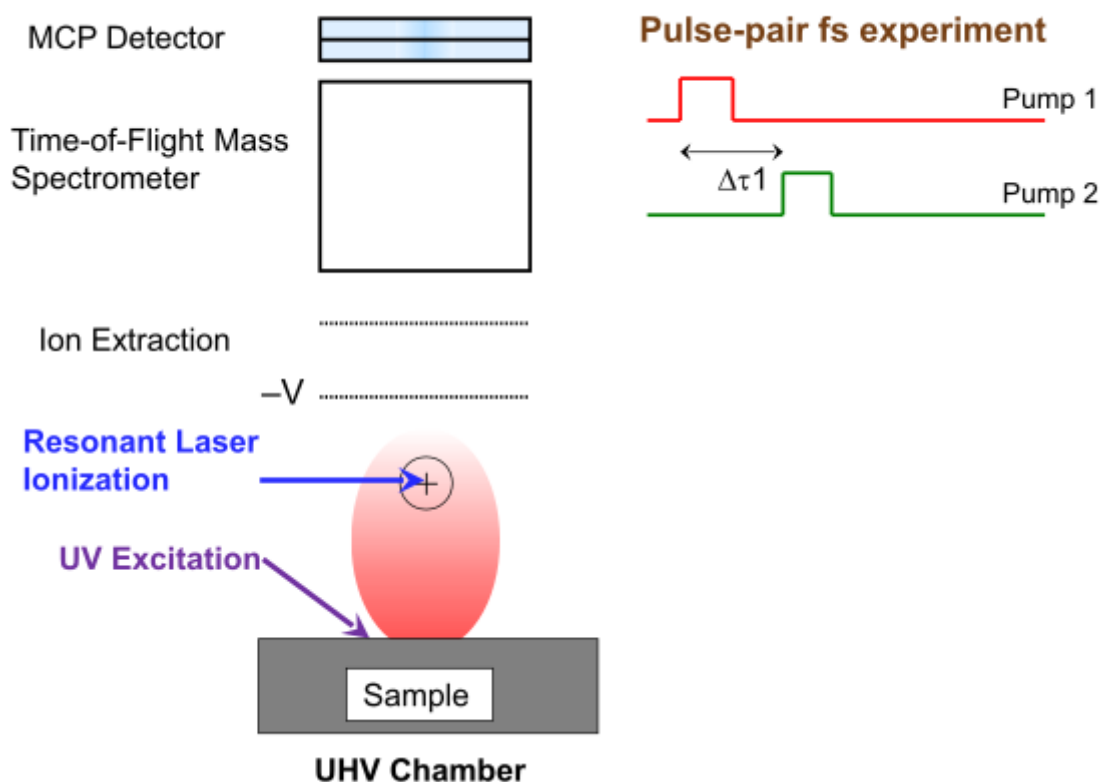


Figure 5.1: Experimental schematic of the apparatus for the desorption experiments conducted at Pacific Northwest National Laboratory (PNNL).

Desorbing atoms are then detected by laser pulses at a distance of 3.8 nm above and parallel to the surface tuned to the resonant frequency of the neutral $\text{Br}(^2\text{P}_{3/2})$ atoms, which are subsequently ionised, and pass through an electric field and a time-of-flight (TOF) spectrometer. The second laser pulse therefore has the purpose of ionising the neutral atoms such that they can then be accelerated by the electric field and their kinetic energy extracted. The velocity of photodesorbed atoms are determined by integrating the Br atom yield as a function of the delay between the pulse and probe lasers, and can be converted by a Jacobian transformation into a kinetic energy distribution.

Figures 5.2 and 5.3 show kinetic energy distributions of desorbed $\text{Br}(^2\text{P}_{3/2})$ atoms from 7 nm CsBr films grown on the LiF(100) and KBr(100) surfaces following emission induced by (sub band-gap) 6.4 and (above band-gap) 7.9 eV photons, respectively.

In Figure 5.2, the hyperthermal kinetic energies distributions are a good fit to Gaussian functions, centred around 0.33 ± 0.02 and 0.27 ± 0.05 eV for the CsBr samples grown on the KBr(100) and the LiF(100) substrates, respectively.

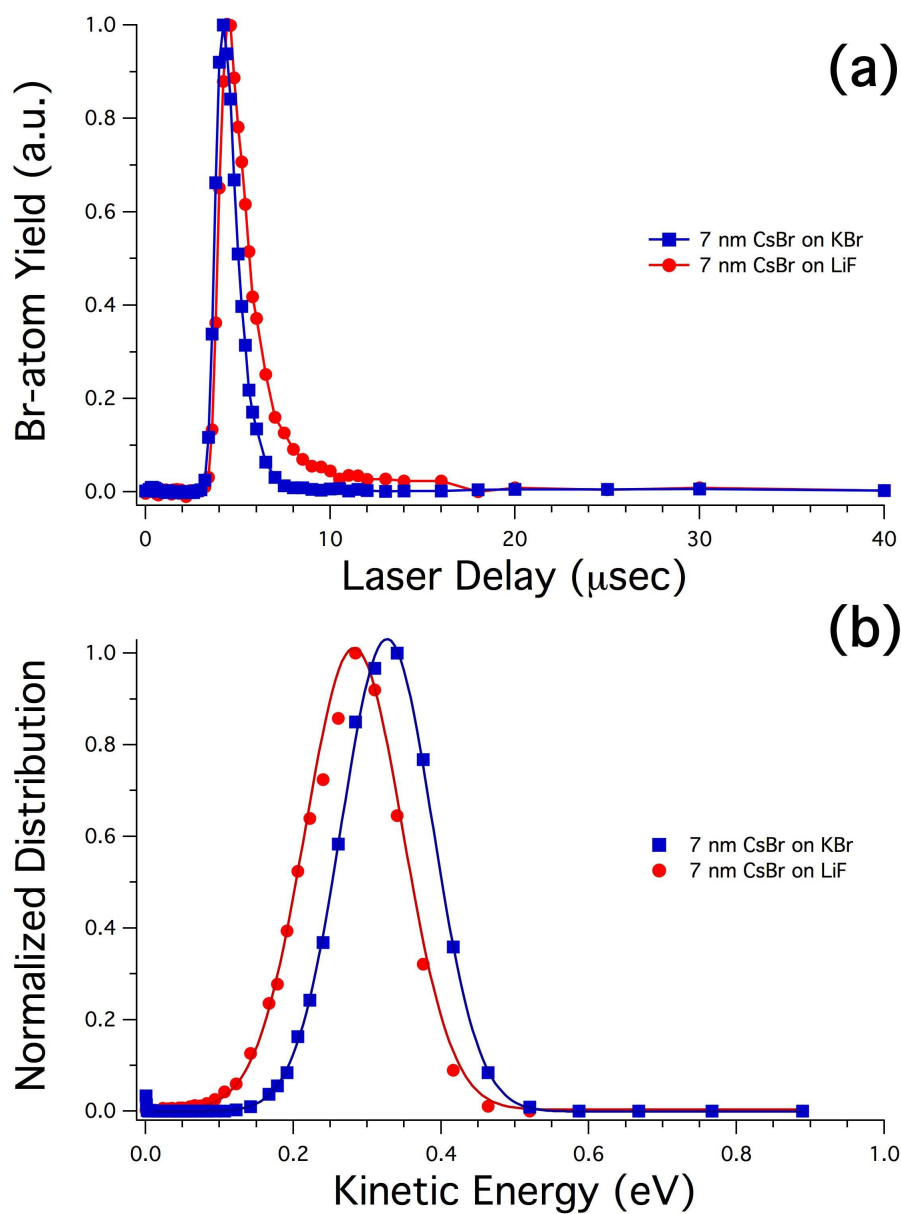


Figure 5.2: The distributions of the desorbed $\text{Br}(^2\text{P}_{3/2})$ atoms following 6.4 eV laser emission showing (a) the laser delay between pulse and probe and (b) the kinetic energy. The hyperthermal kinetic energy distributions peak at 0.33 and 0.27 eV on the KBr(100) and LiF(100) surfaces, respectively. The lines in the part (b) display Gaussian fits to the data.

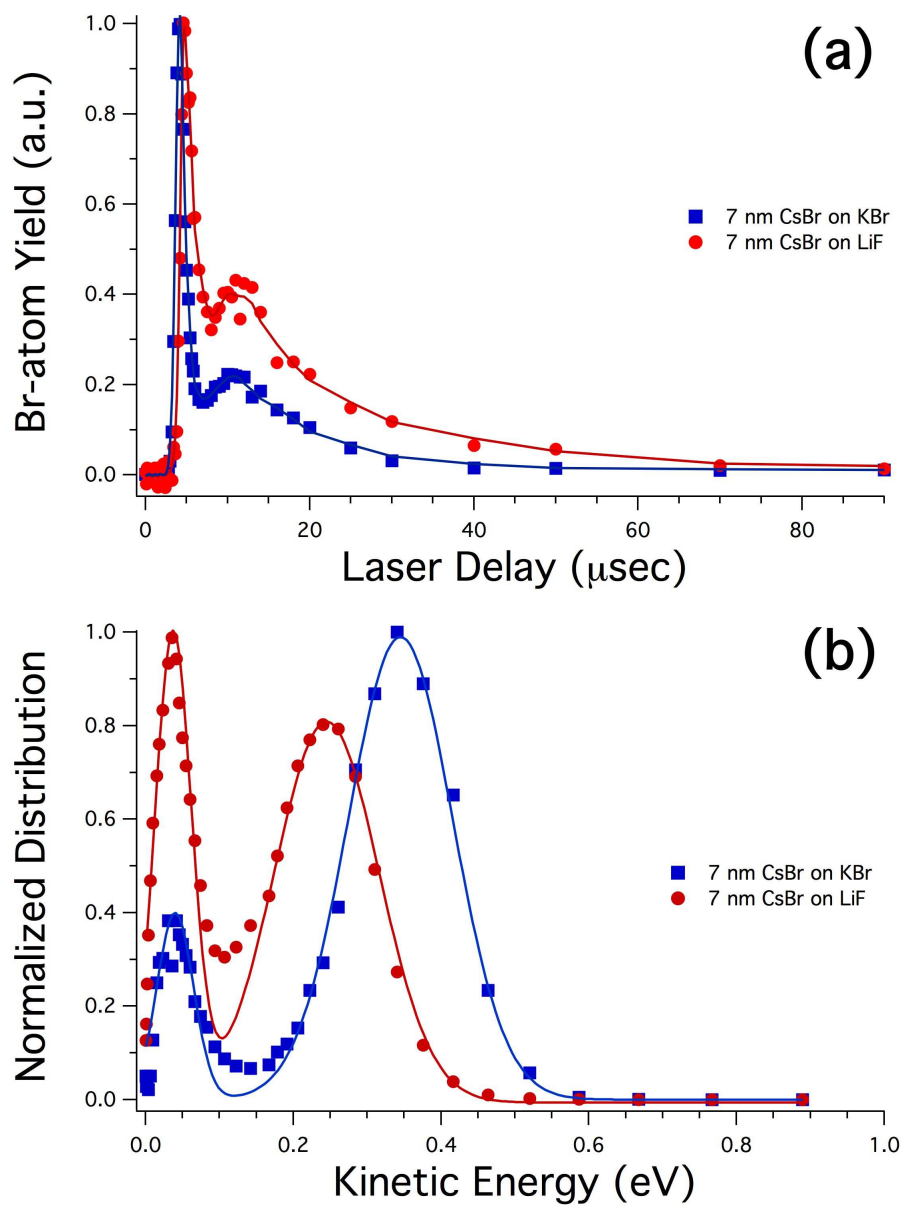


Figure 5.3: The distributions of the desorbed $\text{Br}(^2\text{P}_{3/2})$ atoms following 7.9 eV laser emission showing (a) the laser delay between pulse and probe and (b) the kinetic energy. The hyperthermal kinetic energy distributions peak at 0.34 and 0.25 eV on the KBr(100) and LiF(100) surfaces, respectively. The lines in the part (b) display Gaussian fits to the data.

The analogous data for 7.91 eV excitation is depicted in Figure 5.3. Here the distribution can be fitted by two Gaussians, one for the thermal and one for the hyperthermal velocity distributions. The hyperthermal distribution is centred at 0.34 ± 0.04 and 0.25 ± 0.10 eV on the KBr and LiF substrates, respectively. Both curves contain a thermal component which is much narrower and centred under 0.05 eV.

There are several significant differences between the distributions grown from the LiF(100) and KBr(100) surfaces. The hyperthermal emitted $\text{Br}(^2\text{P}_{3/2})$ velocity peaks are consistently lower in energy on the LiF(100) grown CsBr than the KBr(100) grown CsBr. Moreover the width of the hyperthermal Gaussians are wider in the LiF(100) case. Both of these observations are consistent with a relatively disordered film growing on LiF predominantly composed of α terraces but also exhibiting some roughness and containing low-coordinated sites. We infer from both previous studies outlined above and the symmetric (to a good approximation) hyperthermal peak that the CsBr films are composed of large β (100) terraces.

Furthermore, the angular distribution of emitted Br atoms is much broader for CsBr films grown on the LiF(100) surface, and the signal intensity roughly 35% as strong as the KBr(100) grown CsBr films.

5.3 Methodology

Calculations of the α (110) and β (100) surfaces have been carried out using a slab model with PBCs in the x and y directions, with the electronic structure calculated using DFT as implemented in the CRYSTAL09 code[95]. A modified version of the B3LYP hybrid functional has been used[71, 75], where, as for the calculations of defects in the bulk in Chapter 4, the standard amount of HF exchange energy has been increased, from 20% to 32.5%. This was increased in order to obtain a one-electron level HOMO-LUMO gap as large as the experimentally determined gap. Due to the large number of electrons in the system, (35 for Br and 55 for Cs), the electron cores have been described using Stuttgart pseudopotentials on both ions[132, 189], leaving the $4s^2 4p^5$ and $4s^2 4p^6 5s^1$ electrons to be described by the basis sets, respectively. A number of different pseudopotentials have been tested, including the Hay-Wadt pseudopotentials[190, 191], and were found to be unsuitable for the investigations as their use resulted in large deviations from the calculated band gaps, and incorrectly describing the band gap as in-

Property	α -CsBr		β -CsBr
	experiment	theory	theory
a_0	3.68[133]	3.61	3.61
E_g	7.3 [134]	7.3	7.6
E_{VB}	1.7 [194]	1.7	0.5
E_{coh}	6.7 [195]	7.1	6.8
ϵ_∞	2.78 [196]	2.78	2.30

Table 5.1: The calculated and experimental values of various properties in both α - and β -CsBr in the CRYSTAL09 model. a_0 denotes the lattice parameter; E_g the band gap; E_{VB} the valence band width; E_{coh} the cohesive energy; and ϵ_∞ the high-frequency dielectric constant.

direct. The basis set for Br was taken from the CRYSTAL basis set library and that for Cs from a separate library, given in Ref[97]. Both basis sets were supplemented with d functions, which were added in order to give a greater flexibility to describe the excited states, and also greatly improved the agreement between the calculated and experimental high-frequency dielectric constant, thus improving the description of the polarisation characteristics.

Increasing the band gap of the HF exchange in order to describe the band gap correctly has become standard practice for calculations of alkali halides, oxides and semiconductors[129, 130, 131, 192, 193].

In order to assess the sufficiency of the basis set, and accuracy of the functional description, fundamental properties of both $\alpha(110)$ and $\beta(100)$ have been calculated using the Gaussian molecular software suite[124] (i.e. without PBCs), and the results have been compared with experiment where data exists. These results have been tabulated in Table 5.1. Most of the calculated values compare favourably with the experimental measurements, and the lattice parameters of both bulk α -CsBr and β -CsBr are within about 2% of the extrapolated 0 K experimental values, commonly regarded as the DFT limit[98]. The cohesive energy has been slightly overestimated. Calculations in Chapter 4 suggest that the caesium halides require an account of van der Waals forces in order to improve the calculated cohesive energy, and indeed the inclusion of dispersion forces were found to be necessary in order to correctly describe α -CsBr as being lower in energy than β -CsBr[108]. For β -CsBr only the Cs-Br distance of 3.62 Å has been measured experimentally[2].

In order to test the sufficiency of the CRYSTAL optimised basis set used to de-

Br	$a_0 = 0.2$	%	$a_0 = 0.325$	%	Exp. Value (eV)
1st IP (eV)	11.86	0.4	11.910	0.8	11.814[197]
2nd IP (eV)	21.4	1.7	21.4	1.7	21.8[197]
EA (eV)	3.30	1.9	3.363	< 0.1	3.364[198]

Table 5.2: The calculated and experimental values for the EA and IPs of a Br atom using the pseudopotentials and basis sets used throughout the study and the B3LYP functional with varying amounts of HF exchange energy.

scribe the Br ions, and correctly describe the energetics of anion defects, the first and second ionisation energies (IP) and the electron affinity (EA) of a Br atom have been calculated using B3LYP with a proportion of both 20% and 32.5% HF exchange energy. Calculations have been conducted using the Gaussian software suite[124]. The results of these calculations are written in Table 5.2. The good accuracy of results further supports the functional and basis set used in the model.

5.4 Results

5.4.1 Hyperthermal Desorption

The 128-atom $\alpha(110)$ surface and 144-atom $\beta(100)$ surface have a calculated rumpling of 0.16 Å (4.4% a_0) and 0.04 Å (1.1% a_0), respectively. Both singlet and triplet excitons are known to exist in CsBr, and the triplet state is lower in energy[116]. Initial excitation into the singlet state is followed by a transformation of some of the excitons into a triplet state. As is the case for calculation of the self-trapped exciton modelled in Chapter 4, the triplet exciton can be modelled using ground-state DFT[199] by specifying the spin multiplicity as triplet. The spin state of excitons responsible for emitted Br atoms is unknown, and is here, as in previous studies on the alkali halides, presumed to be triplet[143, 170].

The majority of previous calculations concerning a triplet exciton breaking down into a desorbing Br atom and a surface F-centre have been conducted with small clusters treated quantum mechanically, and embedded into the rest of a crystal which is either modelled with classical point charges[170, 200, 201], or, in more sophisticated models, with polarisable ions[143, 179]. In these small quantum cluster models, desorption has been found to be the only possible relaxation pathway from the triplet excited state.

The periodic model employed here has a number of advantages over embedded

cluster calculations. The large surface unit cells offer much more freedom for relaxation of the ions as a result of the defects, and unlike the situation in small quantum cluster studies, the electrons are not artificially confined to a region treated quantum mechanically. Here all surface ions are equivalent, and both the electron and hole components of the exciton are fully delocalised in the case of the perfect surface.

Photons incident on the surface can create electron-hole pairs which can form a Frenkel-type one-centre exciton, conceived as simultaneously superposed on all equivalent Br-atom surface sites prior to any localisation. Here it is assumed, after previous studies[129], that exciton localisation then takes place when thermal fluctuations of the surface anions are such that it is energetically beneficial for the localisation of the exciton on a surface anion.

In order to model an exciton a Br ion has been displaced from the perfect surface by 0.1 Å ($\sim 3\%$ of the lattice parameter). This displacement is at the tail of vibrational amplitudes at room temperature, and is sufficient to cause localisation of the exciton onto the Br ion. In this way a Frenkel-type exciton is modelled in a pseudostatic state before relaxation has occurred, and thus the energy of the system is calculated immediately prior to the dynamic process of desorption. Attempts to obtain a converged solution without perturbation from the ground-state geometry were unsuccessful.

The optical absorption spectrum of α -CsBr by Teegarden et al. shows the first bulk exciton peak at 6.8 eV[202]. Previous studies of the alkali halides have noted an inverse correlation between the shift in energy from the exciton in the bulk to the surface, and the interatomic crystal lattice parameter[143, 203]. By these arguments, one can expect a shift of approximately 0.4 eV for both α - and β -CsBr. Attempts to estimate this shift as the difference in energy between the one-centre exciton in the bulk and at the surface were unsuccessful as efforts to induce localisation of the one-centre exciton in the bulk failed. However, the calculated surface exciton energy is in good agreement with the value that may be expected with reference to previous studies[143, 203]. In further support of these estimates, the calculated exciton energy for both surfaces differed by less than 0.1 eV. By these observations we conclude that irradiation of both $\alpha(110)$ and $\beta(100)$ surfaces with 6.4 eV photons can create surface excitons, at the very least in the Urbach tail of the surface exciton peak, and irradiation with 7.9 eV photons can excite both the surface and the bulk.

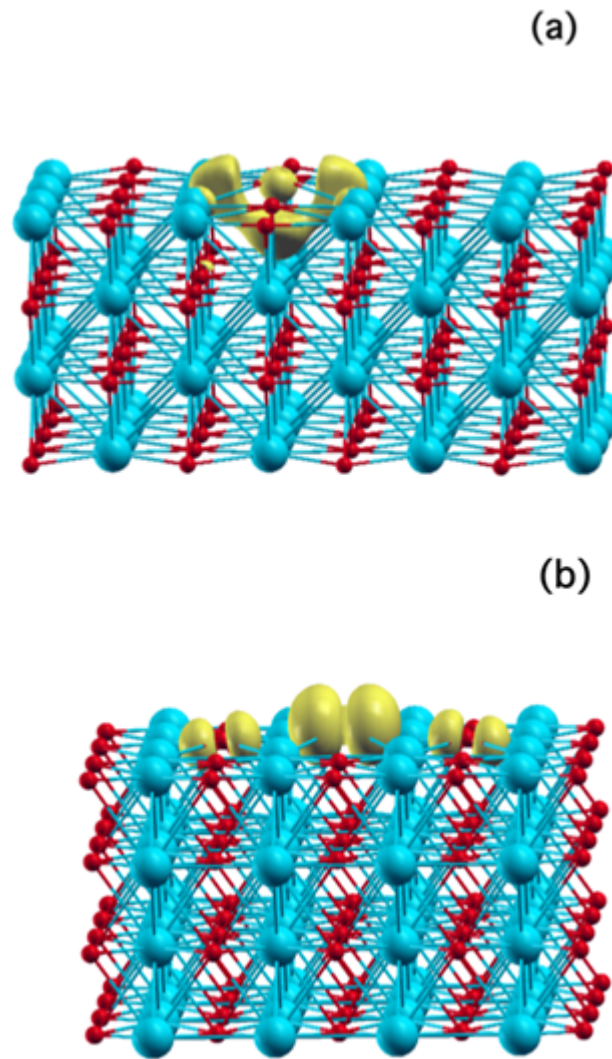


Figure 5.4: Spin density iso-surfaces of the exciton on the $\alpha(110)$ surface. The orbital of the electron component is depicted in (a), with an iso-surface value of $0.001|e|$, and that of the hole component in (b), with an iso-surface value of $0.003|e|$. Note that the two plots are oriented towards the surface from mutually orthogonal directions. The cations are represented by large blue spheres, and the anions by smaller red spheres.

Spin density plots of both the electron and hole components of the localised triplet exciton on the $\alpha(110)$ surface are displayed in Figure 5.4. The hole, labelled (b), resides in a p -type orbital centred on the protruding Br atom, polarised in a direction parallel to the surface, such that a significant amount of the wavefunction is shared between two Br anion neighbours. The electron component, labelled (a), is largely confined to the surface, occupying an orbital polarised in a direction orthogonal to that of the hole, and parallel to the surface, with the bulk of the density below the surface, resembling a nascent F-centre.

The exciton on the $\beta(100)$ surface is similar in form to excitons seen in other rock-salt alkali halides[143]. The hole occupies a p -type orbital centred on the protruding Br anion, polarised normal to the surface. The electron bulbs out of the surface in a comparatively more diffuse orbital that is broadly spherically-symmetric.

The exciton on the $\alpha(110)$ surface is qualitatively different to that on the $\beta(100)$ surface, and on other alkali halides. The separation between surface Br anions is smaller in the α case than in the β case (4.2 Å and 5.1 Å), and the rumpling of the $\alpha(110)$ surface is larger than that of the $\beta(100)$ surface. The Br anions are therefore closer to and less shielded from each other on the $\alpha(110)$ surface. This means the hole is in an orbital shared across neighbouring anions parallel to the surface, in an orbital similar to the of a σ -bonded Br_3^- molecule, with a larger amount of electron density centred on the protruding Br ion. This reflects a general tendency of polarons in CsBr to tend to compound, creating a situation where it is generally energetically beneficial to form Br_2^- or Br_3^- compounds, as in the case of trapped holes and interstitial ions, (V_k^- and H-centres), and interstitial atoms (I-centres), covered in Chapter 3.3.2 and 3.3.3. This is in contrast to the β case, where both the electron and hole are in p orbitals perpendicular to the surface. The proposed mechanism of hyperthermal desorption is depicted in Figure 5.5.

Radiation impinging on the surface can interact with the electrons of the surface anions, leading to creation of an electron-hole pair, which can recombine to form a surface triplet exciton, as in Figure 5.5(a). The geometry relaxation can lead to spontaneous emission of a neutral Br atom, leaving an electron behind in the vacancy, a surface F-centre, as in 5.5(b). F-centres have been modelled on both surfaces by the removal of a surface anion and replacing it with a ghost basis set identical to that on

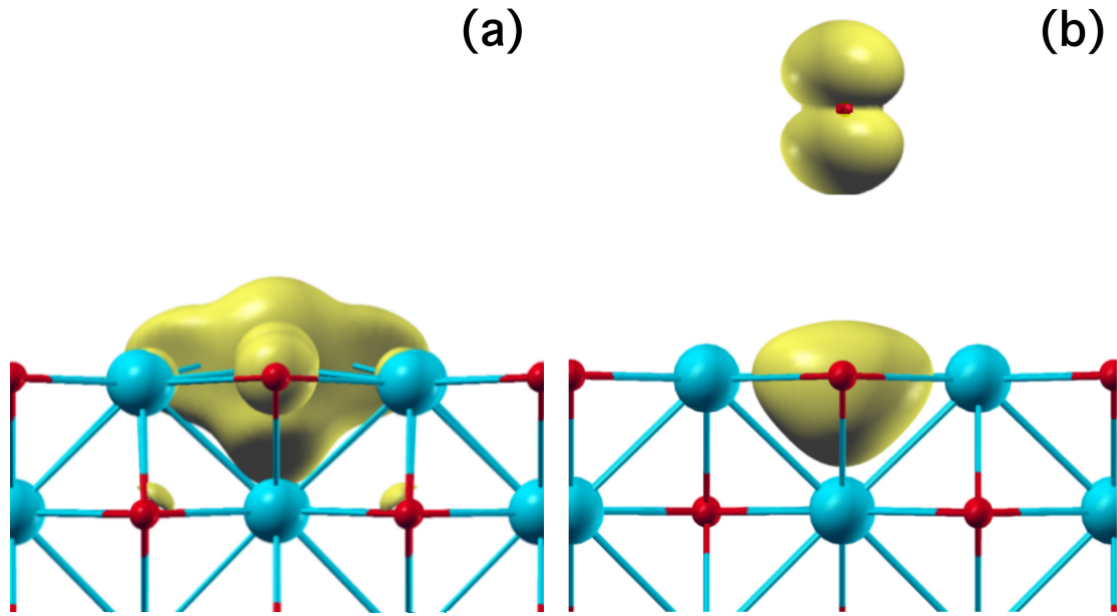


Figure 5.5: Two stages in the hyperthermal desorption process. Spin-density plots corresponding to (a) a surface triplet exciton localised on a surface Br site and (b) a surface F-centre and a desorbing neutral Br atom.

	$\alpha(110)$	$\beta(100)$
Exciton energy	6.41	6.33
Surface F^0 formation energy	6.01	5.67
ΔE	0.40	0.66

Table 5.3: The calculated exciton energies, surface F-centre formation energies, and maximum kinetic energies for both surfaces. All energies are given in eV.

the anions centred on the vacancy site. The ionic coordinates have then been allowed to relax, while the ghost atom basis set coordinates remain fixed. The difference between the energy of a triplet exciton on an atom protruding the surface by 0.1 Å, and an F-centre and Br atom at infinite separation, gives the remaining energy available as kinetic energy to the desorbing Br atom in the dynamic desorption process, where some of the energy will also be dissipated by phonons during desorption. This energy is thus a theoretical maximum kinetic energy for both surfaces, and the the results of the calculations are summarised in 5.3.

A Br atom has been displaced away from the surface in increments of 0.05 Å, with the system energy decreasing monotonically with each step up to a distance of at least 1.5 Å. This indicates a repulsive energy surface, and no barrier for the desorption process to occur.

5.4.2 Thermal Desorption

The bulk of Br atoms measured as result of emission induced by 7.9 eV photons have thermal energies, (see Fig. 5.3). It is hypothesized that this component largely results from weakly adsorbed Br atoms on the surface gaining enough energy from the surface to desorb thermally from the sample. As this component is most prominent in above band gap excitation, it can originate from the creation of excitons in the bulk. In Chapter 3.3.4 the self-trapped exciton in bulk has been modelled. The calculated energy penalty for separation of a self-trapped exciton into an F-H pair is 0.3 eV, and the migration energy of an H-centre has been established in Chapter 3.4.3 to be around 0.05 eV, such that at experimental temperature (~ 300 K) we can expect H-centre mobility through the bulk, and a large number of mobile interstitial atoms as a result of exciton creation and subsequent separation. Here H-centres are examined at and around the $\alpha(110)$ surface in relation to observed ‘thermal’ desorption.

An H-centre has been placed into the second layer of the $\alpha(110)$ surface, and is depicted in Figure 5.6.

The H-centre has been placed aligned along the (100) direction, at an angle of 45° to the $\alpha(110)$ surface, as in part (a). When the ionic coordinates were allowed to relax, the defect moved towards the surface, such that in (b) it resembles an interstitial atom, lying in a position between the surface and second layer, with the two Br ions displaced from their lattice positions. In (c) The H-centre has transferred to the surface layer, the extra electron is shared between the two surface ions, and the axis between the two ions rotates, such that it tends towards a direction normal to the surface. As the coordinates are further allowed to relax the H-centre fully rotates, such that it resembles an adsorbed Br atom on the $\alpha(110)$ surface, which sits 2.9 \AA above a Br anion site, and shares some of the unpaired $4p^5$ electron density with the anion. This is depicted in Figure 5.7(a).

The adsorption energy is calculated as 0.13 eV. This confirms the notion that they are weakly adsorbed and may desorb at room temperature.

As well as relaxing by hyperthermal desorption of a Br atom, the exciton on the $\alpha(110)$ surface can also relax into an off-centre exciton-type arrangement as depicted in Figure 5.7(b). This was found to be the steepest gradient on the energy surface, although desorption of a Br atom is ultimately lower in energy. The spin density plot

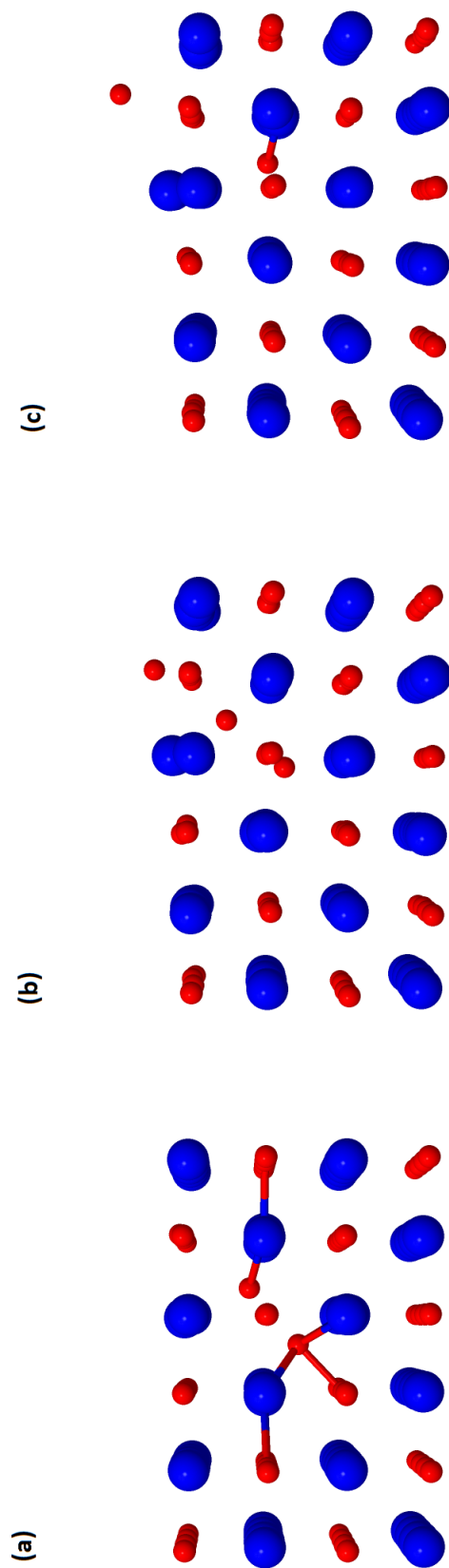


Figure 5.6: The mechanism by which interstitial Br atoms created by the relaxation of an exciton can transform into adsorbed Br atoms on the surface. In (a) the H-centre is in the second layer, where it feels a force in the direction of the surface. In (b) an anion has moved close to the second layer anion lattice position and the partner anion is displacing a surface anion from its lattice site. In (c) The H-centre is now in the surface layer and reorienting towards a lattice and adsorbed Br atom arrangement. Cations are depicted in blue, and anions in red.

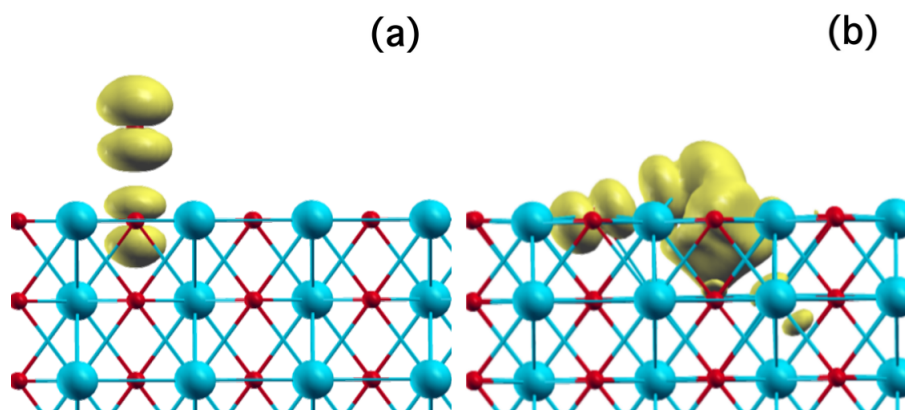


Figure 5.7: A profile of a portion of the unit cells containing the defects, depicting (a) A Br atom adsorbed above a Br lattice site, and (b) an off-centre exciton arrangement at the surface. The spin density is displayed in yellow, and corresponds to an iso-surface of 0.001, with all Br anions depicted in red, and cations in blue.

resembles a pair of nascent F- and H-centres, where the H-centre is inclined at an angle of 19° to the surface, and the F-centre electron is largely confined to the vacancy. It was hypothesized that the Br_2^- could rotate, and then emit a Br atom. In this way surface excitation could directly contribute to some of the hyperthermal distribution in two distinctive ways, however calculations showed that the attractive Coulombic force between the electron in the vacancy and localised hole on the Br_2^- molecular ion was great enough to suppress this behaviour, and therefore there is not a large contribution to the hyperthermal desorption distribution from this channel.

The fact there there exists another relaxation channel for the surface $\alpha(110)$ exciton suggests that, as in the bulk, these could separate into F-H pairs, H-centres could then diffuse along the surface, and eventually desorb thermally, therefore contributing to the thermal distribution directly from excitation of the surface only. It is not possible to predict the relative efficiency of this process with these calculations alone, however the insignificant amount of Br atoms at thermal energies after 6.4 eV sub band-gap excitation would seem to suggest that this channel is less likely than the Br atom desorption channel.

5.5 Discussion

Selective surface excitation has been successfully applied to a number of alkali halides, and has also been investigated in some rocksalt oxides, e.g. CaO and MgO[200, 204], both of which are wide band-gap insulators that adopt the rocksalt structure. A natural extension of this model is to apply it to similar wide band-gap insulators which adopt a different structure, and indeed with suitable substrate choice selective surface excitation can be examined from both the α and β structures directly.

Results clearly show that 6.4 eV radiation can excite the $\Gamma_{3/2}$ exciton on the surface, but not the $\Gamma_{1/2}$ exciton which is expected to be about 0.5 eV higher (~ 6.9 eV) based on the spin-orbit splitting in measured exciton electron paramagnetic resonance (EPR) signal[117]. This is consistent with the fact that comparatively little Br($^2P_{1/2}$) desorption is detected in contrast to the Br($^2P_{3/2}$) signal.

The theoretical calculations leave 0.40 and 0.66 eV available as a maximum kinetic energy for hyperthermally desorbing Br atoms and as energy diffused through phonons on the $\alpha(110)$ and $\beta(100)$ surfaces, respectively. The experimental hyperthermal peaks show an increase of approximately 0.1 eV from CsBr films grown on KBr(100) with respect to those grown on LiF(100), in both the 6.4 and 7.9 eV irradiation cases (see Figs. 5.2 and 5.3). This would vindicate the theory that these peaks are due to the proposed hyperthermal desorption process, Br atoms emitted from surface sites subsequent to surface excitation.

The 7.9 eV radiation can excite electrons from the valence band into a conduction band state, creating electron-hole pairs (e^-h^+) in the bulk. These can relax into self-trapped excitons in the bulk. Calculations in Chapter 4 show these can separate and H-centres can diffuse through the lattice in the (100) direction. Calculations of H-centres at and around the $\alpha(110)$ surface here are shown to move towards the surface under the influence of forces, and reorient, decomposing into a weakly adsorbed Br atom positioned above a Br surface site, with a calculated adsorption energy of 0.13 eV, thermally accessible to Br atom at the temperatures of experiment (300 K). Indeed, the thermal component is significant following 7.9 eV radiation, but not after 6.4 eV radiation.

These calculations predict both desorbing and non-desorbing channels of relaxation of the surface exciton. The former is clearly fast, and the second channel may

lead to thermally desorbed Br atoms, a much slower process.

The calculations support the propositions that predominantly $\alpha(110)$ rough films and relatively clean $\beta(100)$ films are grown on the LiF(100) and KBr(100) surfaces, respectively, due to epitaxial lattice constraint. This is significant in consideration of the growth of CsBr films on Cu, as the Cu(100) has a lattice mismatch of 1% and 33% with KBr(100) and LiF(100), respectively, and so we predict growth of polycrystalline of $\beta(100)$, with large terraces. Thick films of CsBr grown on the Cu(100) surface will be examined in Chapter 6. Chapter 6 also contains models of CsBr surfaces with the PBE0 functional.

In conclusion we have provided evidence supporting models of hyperthermal and thermal desorption from the $\alpha(110)$ and $\beta(100)$ surfaces. The disparity between the velocities of hyperthermally desorbing Br atoms can be attributed to the difference in localised on-centre exciton energies at the surface resulting from structural differences of the two films. These results form a prelude to understanding desorption from CsBr/Cu films investigated in the next chapter.

Chapter 6

Desorption from CsBr/Cu films: Trapped Electrons, Holes and Excitons

The aim of this chapter is to extend the models of desorption from insulator-grown CsBr films to Cu-grown CsBr and explain experimental kinetic energy distributions of desorbed Br atoms from UV-irradiated CsBr/Cu. The existence of the metal substrate substantially changes the photophysics, leading to desorption occurring at lower energies. These calculations therefore offer insight into the material degradation of CsBr/Cu photocathodes in operation. A model of cation desorption via excitation of surface F-centres subsequent to excitation by electrons photoemitted from the substrate is presented. The experimental results are explained via a model of electron-trapping at defect sites at the CsBr surface, which creates an electric field acting to decrease surface exciton energies, leading to slower desorption. The model also predicts that electrons trapping at divacancies on the surface inhibit the agglomeration of vacancy clusters at the surface, leading to a qualitatively different evolution of the surface with comparison to irradiated CsBr grown on insulating substrates.

6.1 Introduction

In Chapter 5 we have examined the experimental profile of desorbed Br atoms from irradiated films of CsBr grown on LiF(100) and KBr(100) surfaces, and provided models of Br desorption supported by *ab initio* calculations following radiation from photons at energies larger than and smaller than the band gap (7.9 eV and 6.4 eV, respectively). The insulating substrates were chosen so as to encourage growth of α - and β -CsBr films, respectively. Two channels of Br desorption have been identified, termed “hy-

perthermal” and “thermal”. Hyperthermal desorption results from excitation of the surface and is observed after irradiation of 6.4 and 7.9 eV photons. Photons incident on the surface can create surface excitons, which can become instantaneously localised at an anion surface site due to displacements following thermal vibrational displacements. Surface excitons can relax by emitting a neutral Br atom and leaving an F-centre on the surface. Thermal desorption is only observed following above band-gap (7.9 eV) excitation and derives from the creation of excitons in the bulk, which can separate into F-H pairs. H-centres can freely diffuse through the bulk at these experimental temperatures, and near the surface transform into weakly adsorbed neutral Br atoms on the surface, which can subsequently desorb with thermal energies.

Interest in CsBr stems from the observation that films of CsBr deposited on bare Cu greatly improves the effective functioning of the Cu as a photocathode. CsBr/Cu-based photocathodes have a considerably larger QE than photocathodes constructed of bare Cu. Their use has been motivated by the need for a protective layer, however how exactly the protective films will degrade during irradiation remains unknown. As a natural extension to the calculations contained within Chapter 5, here we examine Br desorption data following desorption from films of CsBr and KBr grown on the Cu substrates. Preliminary investigations suggest the presence of the metal profoundly affects the photophysics. Perhaps counter-intuitively, this Br desorption profile seems to change little as film thickness is varied.

An understanding of how CsBr protective films degrade and evolve during irradiation is essential in order to assess the viability of CsBr/Cu based photocathodes, and to inform their design. Moreover, an understanding of how insulating films grown on metal substrates behave after laser excitation is of general scientific interest.

The aims of this chapter are three-fold: to explain the velocity profile of emitted Br atoms from CsBr/Cu films, to provide some understanding of the evolution of CsBr/Cu films following irradiation, and to provide insight into the electron and hole-trapping characteristics of defects at CsBr surfaces.

6.2 Experimental Methodology and Results

Films of CsBr and KBr have been deposited by PLD techniques on the Cu(100) and KBr(100) surfaces from an effusion cell at 425 °C. The experimental apparatus is iden-

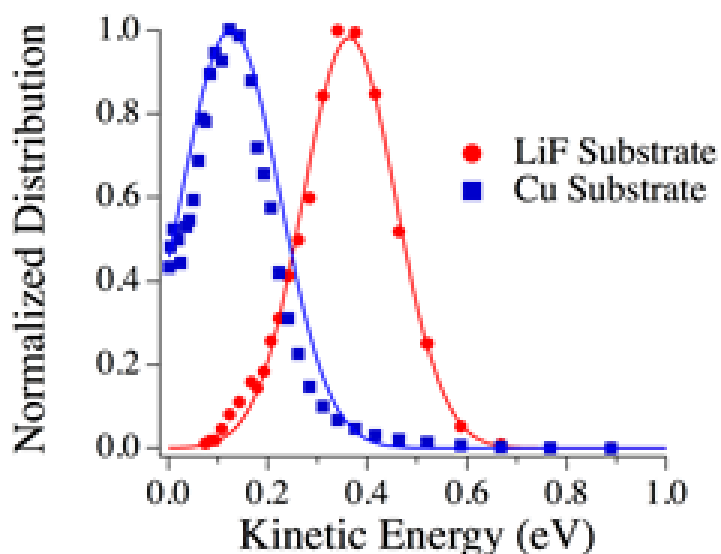


Figure 6.1: Preliminary results of the velocity distribution of neutral $\text{Br}(^2\text{P}_{3/2})$ atoms after 4.7 eV irradiation of KBr/LiF and KBr/Cu films. Image provided courtesy of Prof. Wayne Hess and Dr. Alan Joly.

tical to that described in the experimental background section of Chapter 5, where it is described in more detail. The error in film thicknesses has been estimated as $\pm 5\%$. Figure 6.1 displays normalised kinetic energy distributions for $\text{Br}(^2\text{P}_{3/2})$ emission following 6.4 eV excitation of KBr films grown on LiF and Cu substrates. The KBr films have been studied in order to offer insight into the desorption of CsBr films.

The KBr/LiF energy distribution has been fitted to a Gaussian with a peak at a kinetic energy of 0.36 eV, and the KBr/Cu energy distribution has been fitted to a Gaussian peaking at 0.13 eV. Figure 6.2 displays the desorbed Br kinetic energy distributions following 6.4 eV irradiation of CsBr films of various thicknesses grown on Cu substrates.

As in Figure 6.1, the distribution displays an asymmetry, in particular a high energy tail, which is not apparent from the analogous desorption profiles contained in Chapter 5, following excitation of CsBr from insulating substrates (KBr and LiF). The distribution appears to be very similar for the films of varying thicknesses, and peaks around 0.1 eV. It is unclear if we are looking at “thermal” or “hyperthermal” desorption, but as the films have been irradiated with sub-band-gap laser energies (4.7 eV), and as a Gaussian fitted to the KBr/Cu distribution peaks at around 0.13 eV, significantly higher than thermal energies, we conclude that we are looking at attenuated hyperthermal des-

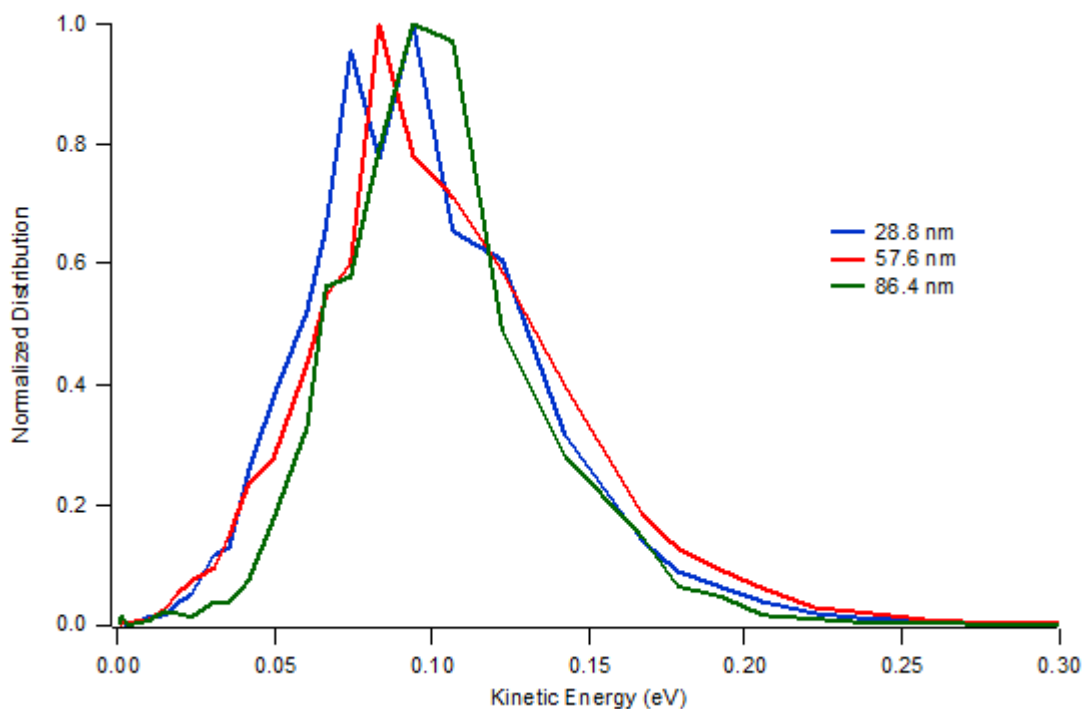


Figure 6.2: The velocity distributions of emitted neutral $\text{Br}(^2\text{P}_{3/2})$ atoms after 4.7 eV irradiation of CsBr/Cu films of various thicknesses (see key). Image provided courtesy of Prof. Wayne Hess and Dr. Alan Joly.

orption, rather than thermal desorption where the Br atoms have by some mechanism gained a small amount of energy. The lack of thickness dependence has been observed for films as thin as 7 nm and as thick as 200 nm. Figure 6.3 displays Br desorption kinetic energy profiles of KBr deposited on both LiF and Cu of different thicknesses. The lack of thickness dependence of desorption from KBr/Cu films is apparent, as well as the presence of a high energy tail not observable in desorption from KBr/LiF films.

Kelvin Probe measurements of the surface charge of the films have been performed approximately two minutes after irradiation and have measured a small negative potential at the surface of -0.15 V, equivalent to a charge density of approximately 10^6 electrons/cm². The accumulated surface charge discharges fully over the course of several hours.

As the thickness of the films appears to have no discernible effect on the Br atom velocity distributions, we hypothesize that the disparity between the desorption distributions from insulating and metal substrates is due to electrons photoemitted from the Cu substrate, rather than by direct interaction between the metal and the alkali halide surface. This lack of thickness dependence is observable in both CsBr/Cu and KBr/Cu

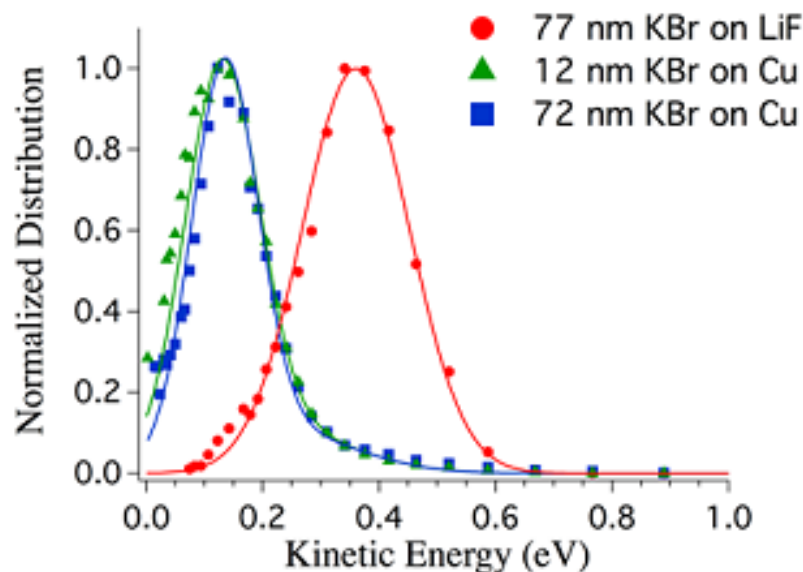


Figure 6.3: Kinetic energy distribution functions for Br-atom emission from 77 nm-thick KBr films deposited on LiF (red circles) and a 12 nm-thick KBr film deposited on Cu (blue squares) and a 72 nm-thick KBr film deposited on Cu (green triangles) following 4.7 eV laser excitation. The nominal film thickness does not appreciably change the recorded kinetic energy distribution function.

films. If we discount the possibility of direct interaction between metal and film, the only difference between the CsBr/Cu and the CsBr/KBr systems at the CsBr surface is the presence of photoemitted electrons, hence our hypothesis.

As argued in Chapter 3, α -CsBr(110) surfaces are produced by deposition of CsBr on LiF($a_0=4.04$ Å) substrates, and the β -CsBr(100) surface by deposition of CsBr on KBr($a_0=6.60$ Å). We note that the lattice mismatch of the Cu(100) surface ($a_0=3.61$ Å) is very large with α (110) (33%), and very small with β (100) (1%), we expect CsBr deposited on Cu(100) to be β (100). The LEED experiments conducted by Kiguchi et al. show that films of β (100) are grown on KBr under much less favourable lattice mismatch conditions (22% and 8.5% for α (110) and β (100) films, respectively). Although we expect the CsBr films to be largely β -type, the roughness of the film surfaces remain unknown, both before and after irradiation. Due to Br desorption from the films vacancies will accrue on the film surfaces during irradiation. Atomic Force Microscopy (AFM) images of KBr after high-energy (\sim keV) electron bombardment reveal a surface characterised by monatomic pits, which largely preserve stoichiometry (see Figure 6.4).

The monatomic pits contain low-coordinated sites, such as step edges, and internal

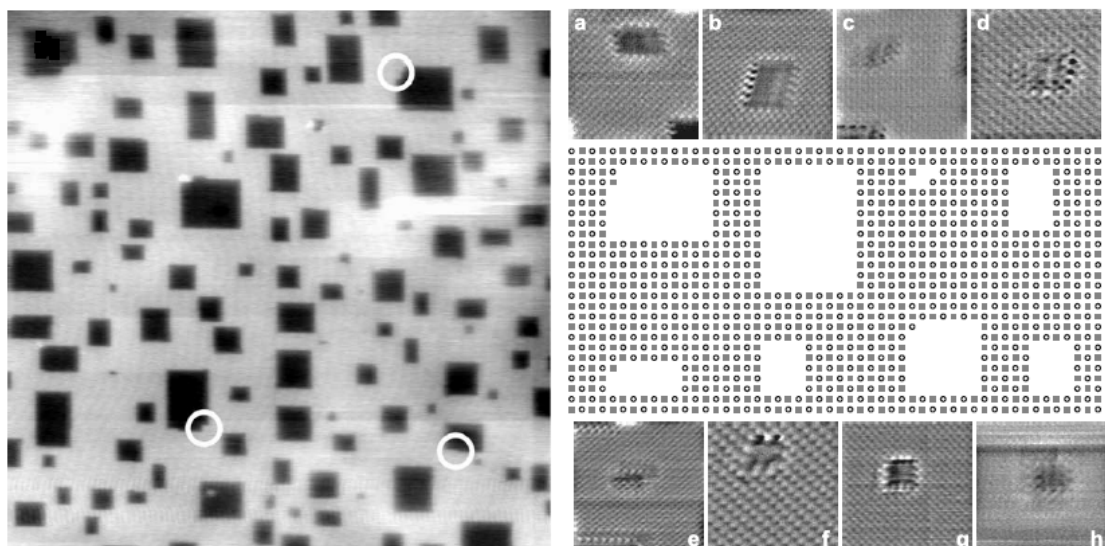


Figure 6.4: AFM images of electron-irradiated KBr. On the left characteristic monatomic pits are clearly visible. On the right are displayed atomic resolution of various surface features, along with a schematic interpretation of the atomic structure. Copyright of Elsevier[4].

corner sites, with a number of kink sites (identified by white circles). Although films grown here are irradiated with a laser of significantly lower photon energy, and films have been grown on Cu substrates (i.e. metal), these images can serve as a first order guide as to the surface topology of irradiated CsBr/Cu films.

6.3 Methodology

Two distinct models have been used to perform calculations in this chapter, one model using an embedded cluster model as implemented in the GUESS code, and a model using PBCs as implemented in CP2K[96, 205].

In order to model the $\beta(100)$ surface using a QM/MM embedded cluster model, an 8-layer thick slab consisting of 40 000 atomic centres was constructed, such that the on-site electrostatic potential on the surface is that of an infinite slab to within an accuracy of 1 meV for every atomic centre within 25 Å of the centre of the nanocluster. As for calculations in Chapter 4, the nanocluster has been divided into Region 1, 2A, and 2B, depicted in Figure 6.5.

The B3LYP functional with 32.5% exact exchange has been used along with the basis sets and classical potentials used to model bulk α -CsBr in Chapter 4. Calculations on the perfect terrace have all been conducted with a Region 1 Cs₂₉Br₃₀ cluster,

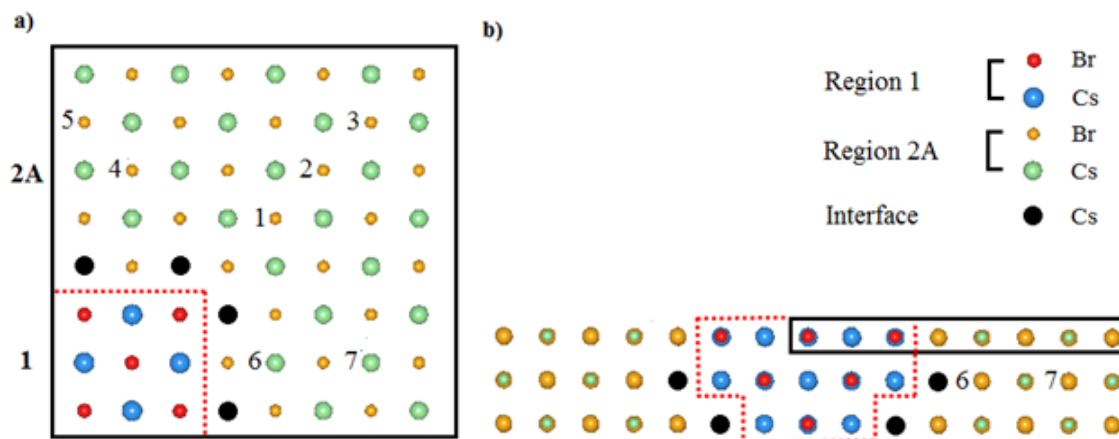


Figure 6.5: a) A quadrant of Regions 1 and 2A and b) a cross-section of the two regions. Anions and cations in Region 1 are coloured red and blue, and in Region 2A yellow and green, respectively. Interface cations have been coloured black. The numbered anions indicate where charges have been modelled, with the consequent desorption energy in Table 6.2. Labels 6 and 7 index anions in the bulk.

with slightly larger $\text{Cs}_{34}\text{Br}_{35}$ and $\text{Cs}_{38}\text{Br}_{38}$ clusters used to describe step and kink sites, respectively. The energy of Regions 1 and 2 have been minimised simultaneously with respect to the coordinates and forces of each region until the change in energy and ionic displacement on each species per step did not exceed 10^{-5} hartrees and 0.003 \AA , respectively.

The Cs-Br separation was calculated as 3.70 \AA in Region 1 and 3.68 \AA in Region 2. The discrepancy gave rise to a small ($\leq 0.5\% a_0$) increase in the displacement of Region 1 ions in the direction perpendicular to the plane of the surface.

A 5-layer 320 atom $\beta(100)$ surface has been modelled in CP2K using a slab model, with 2D PBCs in the x - and y -directions, and a vacuum in the z -direction. The PBE0 functional has been used with an increased HF exchange (37.5% instead of the standard 25%) in order to reproduce the one-electron band gap, when varying the amount of exact exchange in increments of 2.5%. Although in theory DFT does not describe the conduction band well as calculations are made in the fictive Kohn-Sham system, and there exists no equivalent to Koopman's theorem in HF theory which can be used to define quasi-particle energies, in practice this appears to be accurate enough for our purposes and has become standard practice (see the methodology section of Chapters 3 and 4 for references to the literature). This is the same increase from the standard PBE0 fraction as was required to replicate the band gap with standard B3LYP fraction as described in Chapter 5, (12.5%). The use of the PBE0 functional was motivated by a desire to model

the CsBr/Cu system using a mixed PBE0 and PBE functional to describe the CsBr and Cu, respectively. In conjunction with the ADMM method this would make calculations feasible where otherwise the calculation of the full hybrid exchange-correlation would be prohibitively computationally expensive. The use of the PBE0 functional also provided an opportunity to test the effect of a different functional on the calculated properties of the system. The set of GTH pseudopotentials[206, 207, 208] has been used to describe the cores of the Cs and Br ions, with Double-Zeta MOLOPT valence basis sets[209] supplemented with polarisation functions used to describe the valence electrons. After a geometry optimisation of the surface, the rumpling was calculated as 0.01 \AA ($0.25\% a_0$). In order to model kink and step sites, atoms have been removed from the top surface layer. In order to model a nanocorner, a cell of 216 atoms has been used, with 12 \AA of vacuum in each direction. A TD-DFT calculation of the surface finds the first exciton energy peak at 5.9 eV, such that 6.4 eV photons have sufficient energy to excite the surface.

6.4 Results

Figure 6.6 illustrates schematically the mechanisms by which incident 6.4 eV photons can potentially contribute to the emitted $\text{Br}(^2\text{P}_{3/2})$ velocity distribution. Photons can, as (1) create excitons at the surface. Excitons relaxing at the terrace has been established in Chapter 5 to be the primary source of desorbed Br atoms from CsBr films grown on insulating substrates at laser energies of 6.4 eV. Excitons may also be created at low-coordinated sites on the surface, as well as at terrace sites. In contrast to films grown in insulators, photons may penetrate the films and induce photoemission of electrons from the metal, as (2). A study of photoemission following irradiation of Cu with 6.2 eV photons has measured a wide distribution of photoemitted electron energies ranging from 0 - 2 eV, peaking at around 1 eV[210]. Many studies have measured the reduction of the work function after the deposition of thin CsBr films on Cu, with the most conservative estimates measuring a reduction of 0.8 eV[54].

As a combination of work function reduction due to the films, and increased photon energy used in this study, we are effectively radiating with photon energies of $6.4 + 0.8 = 7.2 \text{ eV}$, or 1 eV greater than the study cited above, and as such we estimate electron emission to range from 0 - 3 eV, and peak at energies of 2 eV as a first or-

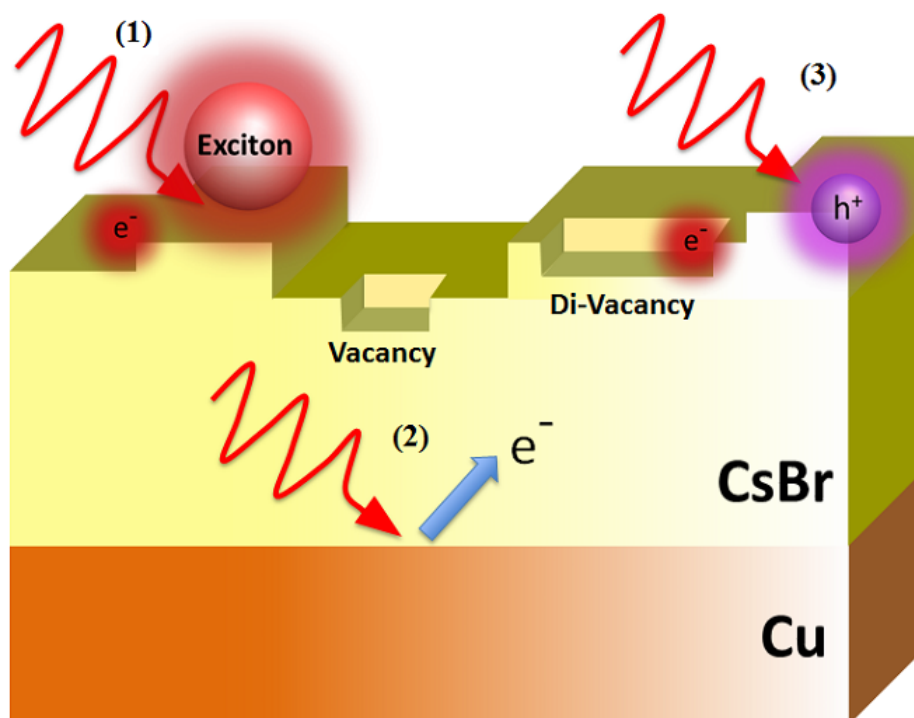


Figure 6.6: Photons incident to CsBr/Cu, and the three distinct ways they can directly or indirectly contribute to the emitted $\text{Br}(^2\text{P}_{3/2})$ distribution. Photons may, as (1), interact with surface sites creating excitons, may as (2), penetrate the films and induce photoemission of electrons from the Cu substrate, or as (3), create a hole at a surface site.

der approximation. As the mean free path of electrons at the energies around 1 eV is large[5, 211, 212], we expect some of the electrons to pass through the CsBr conduction band and either become trapped by defects or low-coordinated sites on the surface, or to excite existing surface defects. Finally, as (3), photons can ionise low-coordinated sites at the surface, creating holes, which may subsequently lead to neutral Br atoms desorption.

Irradiated films of CsBr grown on LiF, as in Chapter 5, may contribute to the Br desorption distribution via (1) and (3), however desorption from CsBr/Cu films is affected by electrons induced by photoemission from the metal substrate, as (2). One explanation of the dramatic change in photophysics from CsBr films grown on LiF and those grown on Cu is due to photoemitted electrons. The following sections undertake an analysis of several desorption pathways.

6.4.1 Excitons at the $\beta(100)$ Surface

Triplet excitons have been modelled on the embedded surface using the DFT technique outlined in Chapter 5, briefly, displacing an anion from the surface by 0.1 Å, so as to model instantaneous localisation due to thermal fluctuation, specifying the spin state as triplet, thus promoting an electron to a higher energy level, leaving a hole in the valence band, and finding a self-consistent solution so as to model a one-centre exciton in a pseudo-static state before full relaxation (and desorption) has occurred. The classical shells in Region 2A have been allowed to relax in order to simulate dielectric screening effects.

The electronic structure of the exciton is displayed in Figure 6.7. A natural population analysis assigns $0.4|e|$ of the hole to the protruding Br $4p$ orbital polarised perpendicular to the surface, with a total of $0.5|e|$ from the four nearest neighbour Br $4p$ orbitals. The electron component is considerably more diffuse, appearing to bulb out of the surface, with $0.35|e|$ and $0.2|e|$ in the four nearest neighbour Cs $6s$ and $6p$ orbitals, respectively. The remaining electron density is spread across the Cs $6s$ orbitals of the cluster. Pulling the Br atom out of the surface results in a monotonic decrease of the system energy, indicating no barrier to desorption, as calculated in the periodic case in Chapter 5. The desorption energy is defined as the difference between the triplet exciton energy, and the energy of an F-centre on the surface and a Br atom at infinite separation, where a positive number indicates that the exciton state is of higher energy. The desorption energy therefore represents the maximum energy available for hyperthermally desorbing Br($^2P_{3/2}$) atoms, and includes any energy diffused through phonons during the relaxation process.

F-centres on the surface have been modelled by the removal of a surface anion and replacing it with a ghost vacancy basis set, identical to that on the anions. Regions 1 and 2 were then allowed to relax under the influence of forces. The electron at the surface vacancy site sits in an energy level 1.7 eV below the vacuum level. As expected, this is higher in energy than in the bulk, where the level is 2.7 eV below the CBM, (see Chapter 4). A natural population analysis shows $0.1|e|$ described by the vacancy s orbitals, $0.7|e|$ by the neighbouring Cs $6s$ orbitals, along with some minor contributions from the Cs $5d$ levels. The desorption energy is calculated as 0.65 eV.

We have used three different models to examine the triplet exciton at the $\beta(100)$

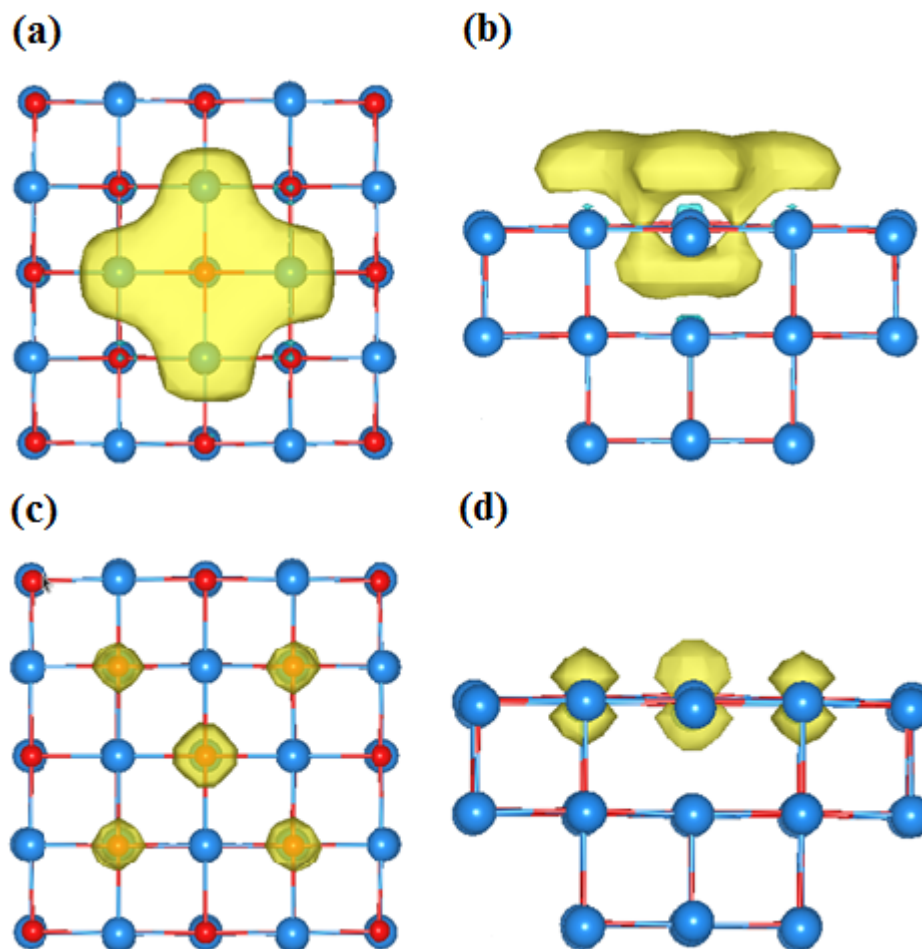


Figure 6.7: The exciton on the $\beta(100)$ surface. The charge density isosurfaces (value = 0.01) of the electron from (a) above and (b) adjacent to the surface, and the hole (c) above and (d) adjacent to the surface. Anions are depicted in red, and cations in blue.

Model	$\alpha(110)$ E_{kin} (eV)	$\beta(100)$ E_{kin} (eV)	ΔE (eV)
CRYSTAL09 (B3LYP)	0.40	0.65	0.24
CP2K (PBE0)	0.36	0.70	0.34
GUESS (B3LYP)	0.36	0.66	0.30

Table 6.1: The calculated energy available for desorption from the $\alpha(110)$ and $\beta(100)$ surfaces for each model.

surface in this thesis, using both different exchange-correlation functionals (PBE0 and B3LYP) and using different models (PBCs and an embedded cluster scheme). The desorption energy as calculated in the three different models is displayed in Table 6.1.

The calculated desorption energies vary across each model by only 0.05 eV, for both the $\alpha(110)$ and $\beta(100)$ surfaces. The differences between the desorption energy for the two surfaces ranges from 0.25 - 0.35 eV in all models. The good agreement with all three models provides further support that both functionals and both approaches (PBCs

and embedded cluster methods) produce results that are very similar to each other, and provide support for the adequacy of each model. In particular, despite the discrepancy between the lattice parameter as calculated in CRYSTAL09 with the slightly deficient basis set with comparison to other models, the calculated desorption energy is nonetheless in good agreement with the models that calculate the lattice parameter more closely to the B3LYP VASP calculated plane-wave converged result. Both CP2K and CRYSTAL09 predict a very small rumpling of the $\beta(100)$ surface of approximately 0.01 Å.

6.4.2 Cation Desorption and the Franck-Hertz Effect

Although the model of anion desorption subsequent to surface excitation is well established in the alkali halides, that of cation desorption is less well understood and experimental data is scarce. Almost equal depletion of Cs and Br has been observed in the XPS spectra of thick CsBr films (i.e. 4ML and above) irradiated by UV light (266 nm) [54]. We also note that the AFM images of electron irradiated KBr and NaCl from Bennewitz et al. appear to suggest that stoichiometry is largely preserved (see Fig. 6.4)[4, 185]. A study has observed the emission of (ground state) Na atoms from NaCl after optical excitation of electron irradiated samples[171]. Calculations following these studies have proposed a model of Na desorption following the excitation of F-centres (F^*), although calculations conducted using HF methods predicted a substantial barrier to this process (2.1 eV)[201].

The difference in energy between the perfect surface, and a surface with a cation vacancy and a Cs atom at infinite separation has been calculated as 6.0 eV. That is, the calculated formation energy of a Cs vacancy at the surface with respect to a Cs atom. The difference in energy between an F-centre at the surface, and a divacancy and Cs atom at infinite separation is significantly reduced, at 1.3 eV, (i.e. formation energy of a Cs vacancy adjacent to a neutral Br vacancy at the surface), but is still too large to expect spontaneous emission.

In order to examine a mechanism analogous to that proposed for cation desorption in NaCl from Puchin et al., we have displaced the Cs ion away from the surface in increments of 0.25 Å and calculated the adiabatic potential surface (APES) in three different scenarios: (a) spontaneous desorption from a terrace site, (b) desorption from a site adjacent to an F-centre, and (c) desorption from a site adjacent to an F-centre with

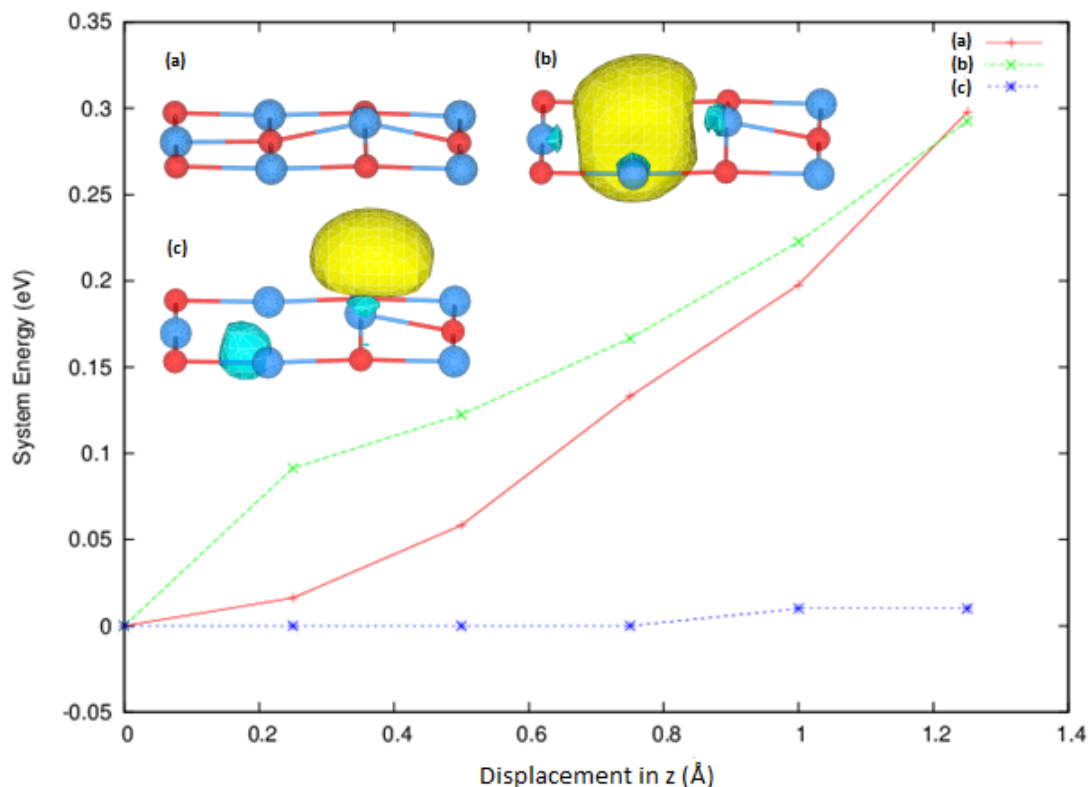


Figure 6.8: The adiabatic potential energy surface (APES) of the Cs atom in perpendicular to the surface from (a) a terrace site (b) a site adjacent to an F-centre and (c) a site adjacent to an F* centre.

the vacancy-centred electron in an excited state. In case (c), the excited F-centre state has been modelled by using TD-DFT at each position of the Cs ion. The calculated APES in the three separate cases is depicted in Figure 6.8. The APES has a positive gradient in cases (a) and (b), corresponding to a force on the ion in the direction of the nascent vacancy, whereas in case (c) the APES is almost flat. In case (c), the excited F-centre orbital is initially delocalised on the four surrounding Cs ions. After pulling the Cs ion out by 0.01 \AA , within the displacements due to thermal fluctuation, the lowest energy transition involves excitation of the F-centre electron onto the Cs^+ ion protruding from the surface, creating a neutral Cs atom. The difference in energy between F* state and a di-vacancy and Cs atom at infinite separation is calculated as 0.08 eV , which we define as the Cs desorption energy. Moving the Cs atom in the x-y plane increases the energy of the calculated excitation, such that trajectory of desorption is perpendicular to the $\beta(100)$ surface. The initial excitation of the F-centre is calculated as 2.1 eV . These results suggest that this mechanism is feasible, and can account for Cs

desorption, and that Cs atoms should desorb at lower energies than Br atoms. As a consequence we would expect the formation of di-vacancies on the surface as a result of irradiation.

Excitation of the F-centre can take place from scattering events of hot electrons photoemitted by the Cu surface travelling in the CsBr conduction band, a manifestation of an effect analogous to the Franck-Hertz effect in solids[213]. The cathodoluminescence spectrum of Al_2O_3 after electron injection shows clear signal from F- and F^+ -centres, providing evidence that these electrons can excite the vacancy electrons in scattering events[214]. Luminescence of electron-excited Ag^+ and Tl^+ impurity ions in similar alkali halides such as RbCl and KCl[215, 216] has also been observed. The calculated F-centre excitation energy (2.1 eV) is well within the estimated range of kinetic energies of photoemitted electrons (0 - 3 eV).

6.4.3 Alternative Br Desorption Pathways

In order to provide a comprehensive analysis of alternative potential relaxation mechanisms which may contribute to the desorbed Br distribution, excitons have been modelled at low-coordinated sites on the $\beta(100)$ surface. The excited states of certain defects have also been modelled, and the possibility of desorption via hole creation at low-coordinated sites has also been investigated, corresponding to processes (1) and (3) in Figure 6.6.

Excitons and F-centres have been modelled at nanocorner and kink sites using CP2K. The periodic model was used to calculate these defects as computation is relatively efficient with respect to the embedded cluster model, which has been used for the majority of calculations in this study. As the defects are neutral the error due to interaction between repeated defect images is negligible. The resulting desorption energy, in the absence of trapped negative charges, has been calculated as 0.70 eV, 0.30 eV and 0.38 eV on the terrace, nanocorner and kink sites, respectively. By moving the anion on which the exciton is centred away from the surface the energy monotonically decreases, indicating there are no barriers to these processes. The decrease in energy is primarily due to excitons at these sites being of lower energy. We note that the cross-section of interaction between incident photons and the terrace will be much larger than that with nanocorner and kink sites, as there are significantly more terrace sites, and also

that electrons trapped at these sites prohibits exciton creation. Nevertheless, part of the low-energy desorbed Br atoms may be due to exciton relaxation at these sites.

Photoemitted electrons can interact with existing defects on the surface, which may contribute towards desorption. In particular, as shown above, electrons can excite F-centres leading to cation desorption. The di-vacancy with an electron is a negatively charged surface defect with a fairly deep potential well. The triplet exciton at the di-vacancy has been calculated by putting the system into a triplet state. The tri-vacancy, a cation vacancy with two adjoining anion vacancies, has also been calculated. In this way we wish to establish whether it is possible that relaxation of excitons at di-vacancies can contribute to the Br desorption profile, by calculating the energy difference between the di-vacancy (initial state), and a tri-vacancy and Br atom at infinite separation (final state). The final state was calculated as being higher in energy by 0.6 eV, suggesting that this mechanism should not significantly contribute to the desorption process. The electron component of the excited electron occupies an energy level in the anion vacancy, such that the exciton is of lower energy than on the terrace. An attempt has also been made to model an excited F^- -centre on the surface, by specifying a triplet state. The electron in the HOMO state sits in an orbital with an energy above the vacuum level, so it was concluded that this is not a stable state, and does not contribute to desorption.

The ionisation potential of nanocorner and kinks sites have also been calculated to examine whether incoming 6.4 eV photons can create holes at these sites, which may subsequently lead to Br atom desorption. The IP has been calculated as 5.9 and 6.2 eV for the kink and nanocorner sites, respectively. Although these energies are accessible to the incoming photons, and this leads to significant reduction of the bonding between the Br atom and the surface, holes localised on these sites experience repulsive forces to desorption, with barriers of 0.7 and 0.6 eV, for the kink and nanocorner sites, respectively. As a result, we conclude that desorption via hole-induced processes is comparatively insignificant with respect to exciton-induced desorption.

6.4.4 Excitons and Charge at the $\beta(100)$ Surface

The Kelvin Probe measurement indicates a small negative charge present on the CsBr surface after irradiation, suggesting negative charges at the surface may be playing

Position	r (Å)	E_{des} (eV)
1	15.7	0.34
2	20.8	0.50
3	26.0	0.58
4	14.8	0.50
5	13.3	0.48
6	18.8	0.31
7	31.2	0.54
no charge	-	0.66

Table 6.2: The energy available for hyperthermally desorbing Br atoms (E_{des}) in the presence of negative charges placed at the positions indicated in Fig. 6.5, and the corresponding distances between the charges and excitons (r).

a role in reducing the energy available for desorbing Br atoms. In contrast to models using PBCs, the embedding cluster method allows for the modelling of positive and negative charges in the classical Region 2, by changing the charge of the ions, without changing the spin state of Region 1, such that the triplet exciton can be modelled using ground state DFT methods in the presence of charge. The effect of trapped holes/electrons at the surface was simulated by changing the charges of the classical shells in Region 2A anions at the positions indicated in Figure 6.5, and recalculating the electronic structures of both the F-centres and excitons. The shells of Region 2A were then allowed to relax. The calculated desorption energies for negative charges placed at the positions indicated in Figure 6.5 are recorded in Table 6.2. Positive charges were found to increase the desorption energy, and have not been further investigated.

The results show that the presence of negative charge reduces the energy available for desorption, up to a maximum of 0.3 eV. Negative charges placed at positions closer than 15.7 Å rendered the exciton unstable, with the energy level occupied by the electron component of the exciton lying above the vacuum level energy. The surface F-centre formation energy is calculated as 5.30 eV in all cases excepting the case where a negative charge is placed at position 1, where it is slightly reduced at 5.18 eV.

The effect of the negative charge on the relatively diffuse electron component of the exciton is comparatively small, with the bulk of the difference in energy due to interaction between the hole component of the exciton and the negative charge. This Coulombic attraction reduces the energy of the exciton, such that there is less energy available for desorbing Br atoms. The hole energy level rises by 0.5 eV as the charge

moves from position 1 to position 3, and rises by 1 eV with the charge at position 1 with respect to the uncharged surface. We note that the local environment of charges placed at positions 1, 2 and 3 with respect to the exciton position is characterised by a line of anions, whereas charges placed at positions 4 and 5 are separated from the exciton by both anions and cations. The difference in polarisability of the Br^- and Cs^+ (approximately 6 and 2.4 \AA^3 , respectively[217]), and their consequently different screening properties accounts for the difference in desorption energy between charges placed at similar distances from the exciton, but at different positions (e.g. 1 and 5).

For completeness charges have also been placed at positions 6 and 7 in the bulk, where they again reduce the energy available for desorption.

These results suggest that negative charges trapped at the surface can affect exciton states and reduce the energy available for desorbing Br atoms. A reduction in energy observed by experiment is, according to these calculations, approximately equivalent to one trapped electron per hundred atoms.

6.4.5 Electron Trapping Sites at $\beta(100)$ Surface

In order to investigate where charges may be trapped at the $\beta(100)$ surface an investigation of the electron trapping characteristics of low-coordinated sites and defects has been conducted.

Charges may be trapped in the bulk at grain boundaries or dislocations[218]. F-centres in the bulk can also trap electrons, becoming F^- -centres. The additional electron raises the energy of the state due to the Coulombic repulsion between the negative charges, such that the energy level rises in the band gap. The one-electron energy level of the HOMO of the F- and F^- -centres in the bulk are 2.7 and 0.5 eV below the conduction band, respectively. The F^- -centre in the bulk has been calculated as being higher in energy than the neutral bulk F-centre by 1 eV in Chapter 4.

In Table 6.3 we have summarised the calculated electron trapping characteristics of several surface defects, namely, F-centres, divacancies, trivacancies and quadvacancies. The vertical electron affinities (EA), which characterise the electron-trapping cross-section, vertical ionisation potentials (IP) after electron capture and relaxation has occurred, which characterises the depth of the potential well with respect to the neutrally charged case, and the thermal ionisation energy of the extra electron (ΔE),

	EA (eV)	IP (eV)	ΔE (eV)
Surface F	-0.35	0.30	-0.13
Divacancy	-0.22	0.85	0.28
Trivacancy	-0.30	0.47	0.05
Quadvacancy	-0.47	0.22	-0.08

Table 6.3: The results for the calculated EA, IP and ΔE of each trapping site, where a positive number for ΔE indicates that the system with an extra electron is of lower energy than without the electron. The energies are defined in Figure 6.9.

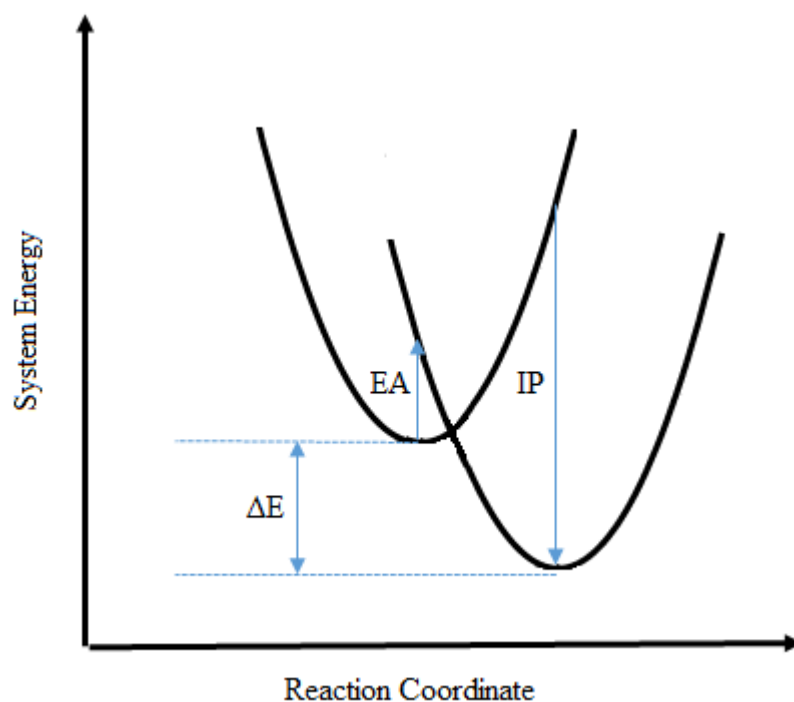


Figure 6.9: A schematic of the potential energy surfaces with and without an electron (above and below, respectively).

which defines the energy difference between fully relaxed states of the defect with and without an extra electron, have all been tabulated. Figure 6.9 figuratively illustrates these energies with respect to the potential wells of each state. Negative values of the EA indicate that there is a not loss in energy with the addition of an electron.

Although we do not have much structural information on what the surface looks like during irradiation, we know F-centres will be produced on the surface due to exciton relaxation via the hyperthermal desorption mechanism. The F-centre EA is calculated as -0.35 eV. After relaxation of the system with the additional electron, the IP has been calculated as 0.3 eV. A natural population analysis shows $1.6|e|$ and $0.2|e|$ described by the four neighbouring Cs $6s$ and $6p$ orbitals, respectively, with $0.2|e|$ on

the Cs 6s orbital immediately below the surface defect and almost no electron density described by the vacancy basis. As there is an energy cost associated with the initial capture of an electron, and the IP is small, we expect F-centres to act as transient electron traps, although it seems unlikely that such shallow traps can account for all the negative charge that our calculations and experiment predict to be at or around the surface. Moreover the neutral F-centre is lower in energy than the F^- -centre by 0.1 eV. A diagram of the F-centre and the F^- -centre, with an iso-surface of the HOMO and the geometric relaxation, is shown in Figure 6.10(a) and (b), respectively.

The divacancy has been calculated as having an EA of -0.22 eV, but after relaxation of the surrounding ions the IP is calculated as 0.85 eV. The bulk of the electron density is in the anion vacancy, with some density spilling over into the vacant cation site. The geometry and HOMO of the divacancy with and without an electron are depicted in Figure 6.10(c) and (d). Thus, analogously to the F-centre, divacancies are not predicted to trap electron easily until they relax, where they become deep electron wells, with a comparatively long lifetime. The smaller magnitude of the (negative) EA and large IP in the relaxed geometry suggest divacancies are plausible candidates as electron traps. In addition, the divacancy with an electron is lower in energy than the neutral state by 0.3 eV.

As divacancies are calculated as more electronegative than F-centres, and AFM images of high energy electron bombarded KBr reveals pits, we have modelled trivacancies and quadvacancies in order to examine their electron trapping characteristics. The calculated EA and IP for all the defects is in Table 6.3.

The electron trapped at the trivacancy (two neighbouring anion vacancies with an adjoining cation vacancy) occupies an orbital that is primarily distributed in the two anion vacancy sites, in equal proportion. The negative charge induces relaxation of the neighbouring cations towards the void. Iso-surfaces of the trapped electron density and local ionic displacements of the trivacancy and quadvacancy are depicted in Figure 6.11. This raises the electrostatic potential on the two anion vacancy sites, such that the occupied energy level rises, and the EA decreases. This effect increases with the quadvacancy, where the electron orbital is largely confined to the two anion vacancies, and ionic relaxation is larger again, such that the EA decreases even further. The divacancy has the highest EA, with the electronegativity decreasing as pit size decreases.

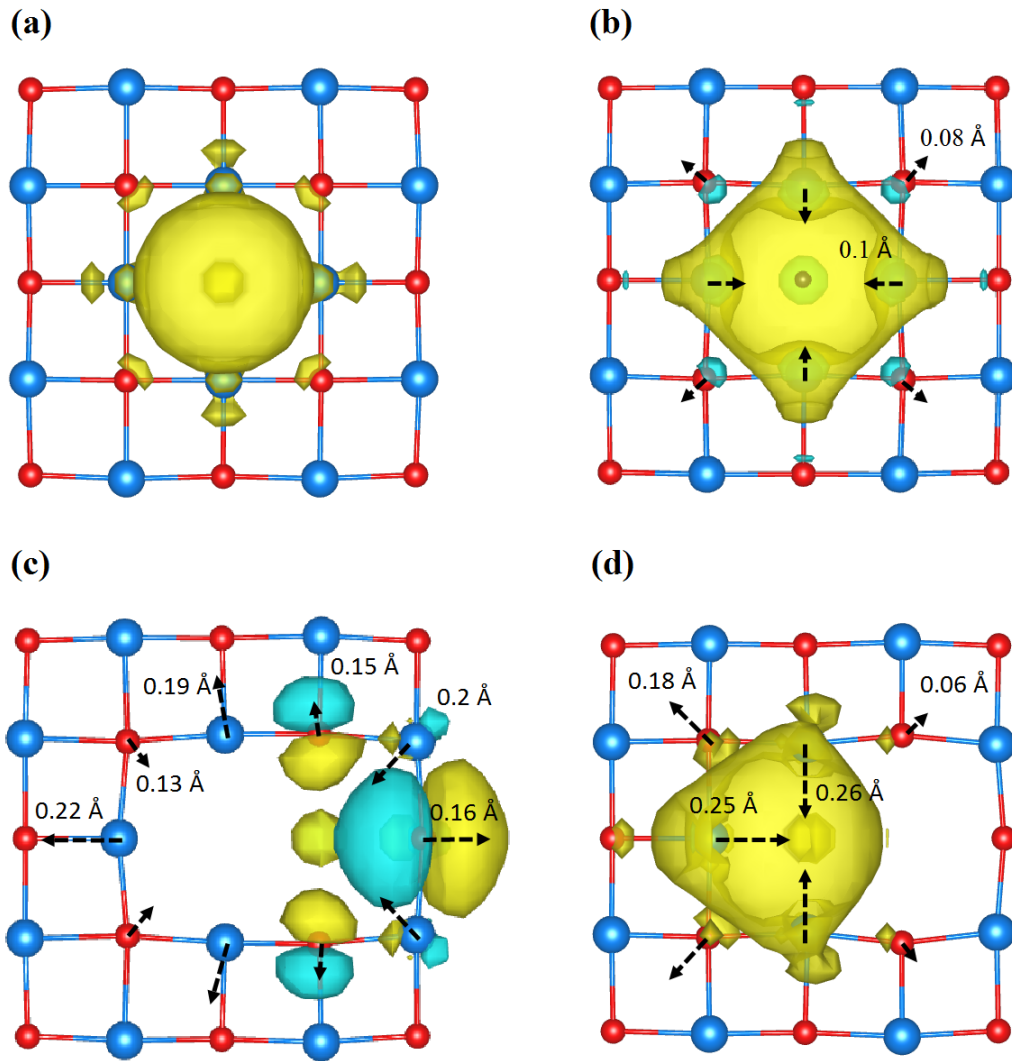


Figure 6.10: The iso-surfaces of the HOMO of (a) an F-centre (b) an F^- -centre (c) a divacancy and (d) a divacancy with a trapped electron. The geometric relaxation is given with respect to the defectless surface for (c), and with respect to the neutral defects (i.e. (a) and (c), respectively) for (b) and (d), with the length of the arrow corresponding approximately to the magnitude of displacement in the directions indicated.

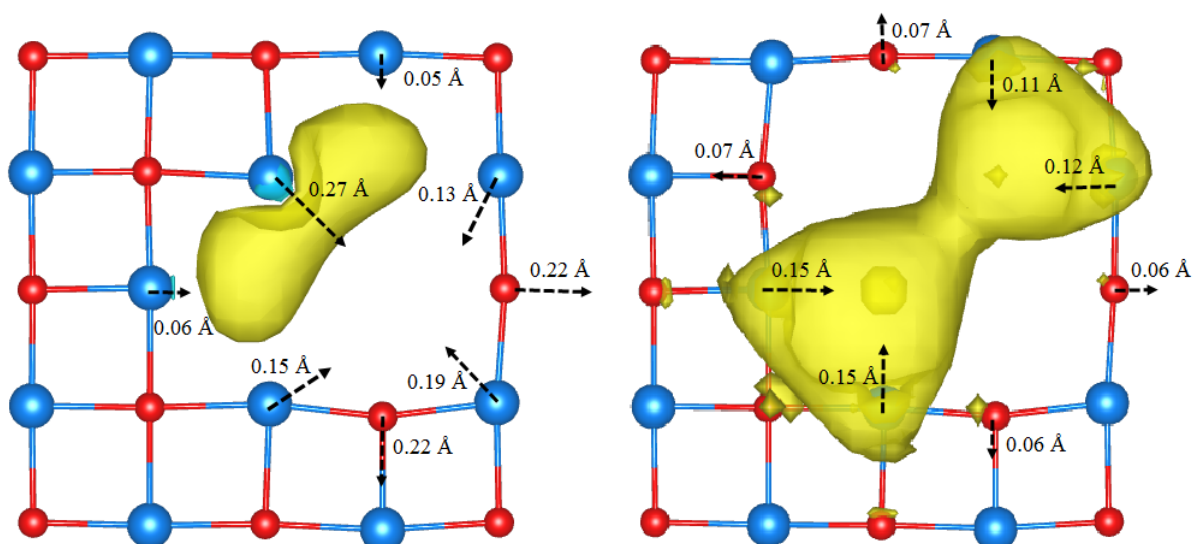


Figure 6.11: The HOMO iso-surface = 0.001 for the trivacancy and quadvacancy with trapped electrons, where displacements are given with respect to the relaxed ionic coordinates in the neutral state. The length of the arrows are approximately proportional to the displacements.

	Coordination Number	EA (eV)	IP (eV)	ΔE (eV)
Terrace	5	-0.66		
Nanocorner	3	-0.13	0.23	0.08
Kink	3	0.02	0.45	0.23
Step	4	-0.02	0.14	0.08
Internal Corner	5	-1.12	-0.25	-0.74

Table 6.4: The calculated EA and IP of the unrelaxed and relaxed geometries for the low-coordinated clusters, and the difference in height of the potential wells with and without an electron.

As well as surface vacancies and pits, the CsBr films grown on the Cu(100) surface may produce a rough film with low-coordinated sites. In order to examine potential electron trapping characteristics of these low-coordinated sites, Cs terminated nanocorner, step, kink and internal corner sites have been modelled, with and without an extra electron. The geometry of the clusters is displayed in Figure 6.12.

The calculated EA, IP and ΔE are displayed in Table 6.4. All the sites examined either have a low or slightly negative EA, although the nanocorner site, and especially the kink site, have a large relaxation when an electron has been captured, and the subsequent IP is significant. The kink site is the only site with a positive EA, albeit small. The relaxed ionisation potential of 0.45 eV is large enough such that one can expect it to function as a fairly robust electron trap. A spin density diagram of the nanocorner

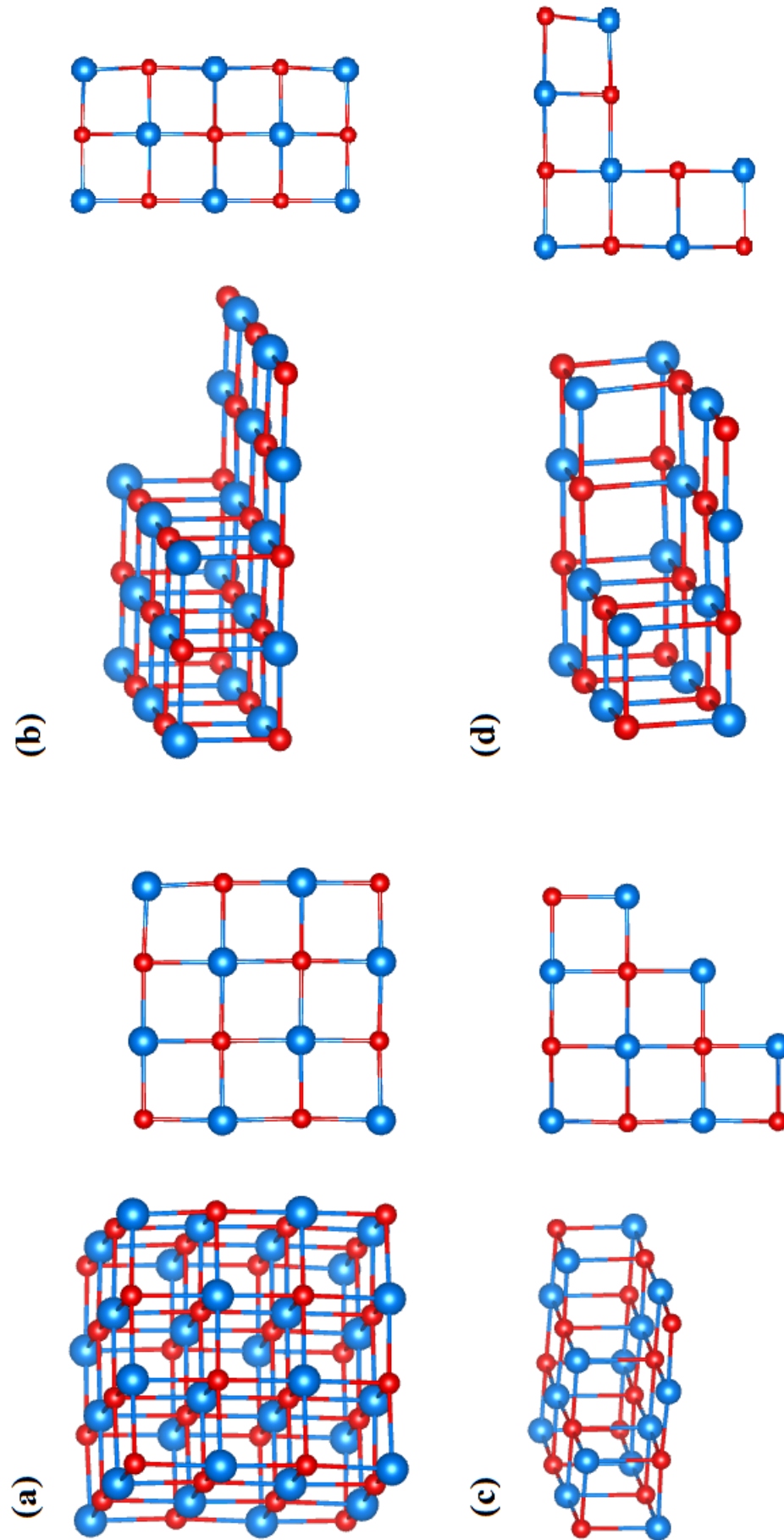


Figure 6.12: Geometries of the clusters used in order to model low-coordinated sites. In (a) a nanocorner sites has been modelled, such that one side of the Region 1 cube is displayed on the right. Parts (b), (c) and (d) are step, kink and internal corner sites respectively. On the left is depicted the top layer of the terrace with the additional ions on top. On the right is displayed the additional ions only, from directly above the surface.

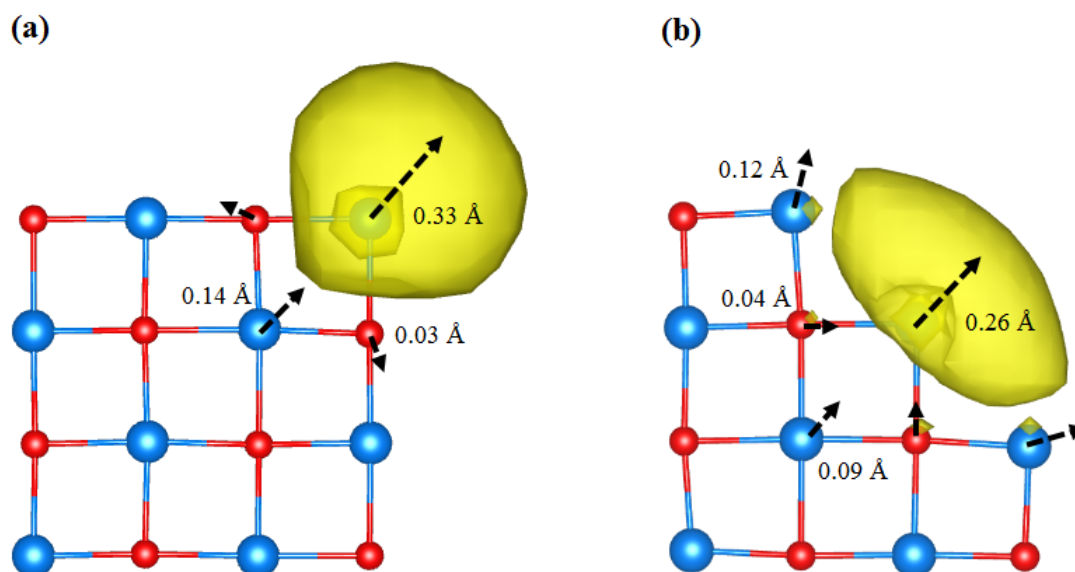


Figure 6.13: The geometry of (a) an electron trapped at a nanocorner and (b) an electron trapped at a kink site. The spin density iso-surfaces have been included, where the surfaces correspond to values of 0.001 and 0.003 for the nanocorner and kink sites, respectively. Displacements are given with respect to the geometry of the uncharged structural defects.

and kink sites with trapped electrons, and the accompanying geometric displacement, is depicted in Figure 6.13. The general trend is the EA and IP both increase as the coordination number of the site decreases.

6.4.6 Evolution of the Irradiated $\beta(100)$ Surface

The results in the previous section demonstrate that divacancies, corner and kink sites are the most likely candidates for electron traps at the surface. The calculated density of negative surface charge required to reduce the desorption energy by 0.2 - 0.3 eV is approximately equal to one electron per (13 x 13) atomic surface units, which is equivalent to a charge density of 4×10^{12} electron/cm². The Kelvin Probe measurement of the charge at the surface at room temperature approximately 2 mins after irradiation reveals a small surface charge of approximately 10^6 electrons/cm². This is consistent with results as all calculated thermal ionisation energies are under 0.3 eV. After 3 mins we would expect the vast majority of these trapping sites to discharge.

The predicted negative surface charge density is not consistent with a surface which dynamically evolves as the post facto AFM images of KBr from Bennewitz et al. These calculations suggest that as a pit increases in size it less readily accepts new

electrons. As such, a surface with large pits is not expected to trap electrons, and photons incident on the terrace should induce hyperthermal desorption by surface exciton relaxation uninhibited by charge. This scenario would result in a desorbed Br kinetic energy distribution with a considerably larger population towards energies of around 0.3 eV, as is the case for desorption from insulating films of CsBr/KBr in Chapter 5.

As the AFM images of KBr have been taken after irradiation, many defects present during laser exposure may have diffused or agglomerated into more regular features. In particular, divacancies may have agglomerated into larger pits. Calculations in Chapter 4 demonstrate that F-centres have a smaller migration barrier than F^- -centres. As a consequence we have conducted calculations in order to estimate the migration barrier for divacancies on the surface with and without a trapped electron. The trajectory of motion has been assumed to be a 90° rotation by inspection, with a Br anion adjacent to the divacancy moving to occupy the Br vacancy. The divacancy has been calculated by removing an anion and adjacent cation from a 4-layer, 144-atom β -CsBr unit cell using CP2K. The migration barrier has been estimated as the difference in energy between the ground state, and the system in the geometry corresponding to the top of the barrier. A Br anion was moved to a site equidistant between the two Br lattice sites, the coordinates of the Br anion and the bottom layer of the CsBr surface were fixed, with all other ions allowed to relax under the influence of forces. Figure 6.14 (a) and (b) depict the divacancy ground-state and barrier point, respectively. The barrier has been estimated as the difference between the energy of the two geometries, and is calculated as 0.46 eV.

Calculations have been repeated with an additional electron. The ground-state and barrier points have been identically calculated, and are depicted in Figure 6.14(c) and (d). As the barrier is estimated as the difference in energy between the two different geometries, corrections due to spurious interactions between charged defects in repeated unit cells has been neglected. The migration barrier has been calculated as 1.2 eV.

6.5 Discussion

We have presented the experimental results for photoinduced desorption from KBr and CsBr thin films grown on metal and insulator substrates. The velocity distributions of desorbed Br atoms changes from a single narrow symmetric peak on CsBr/LiF and

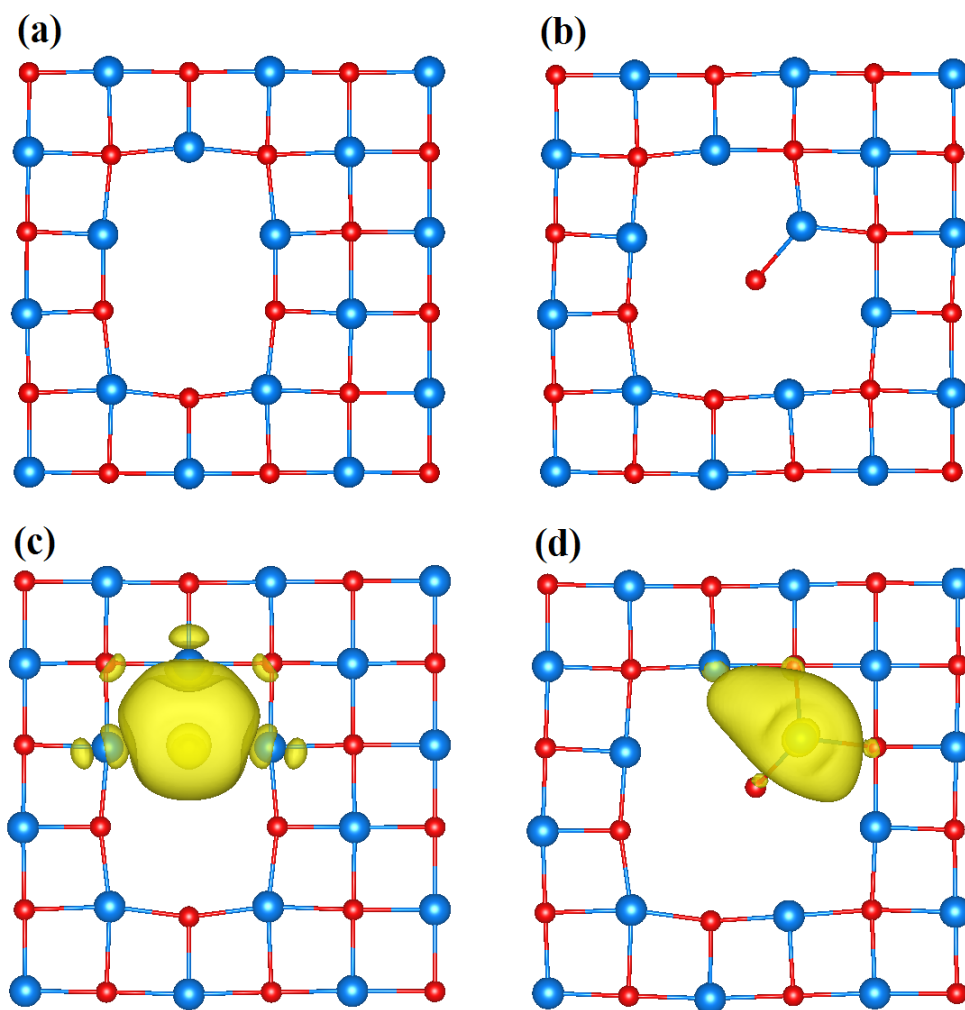


Figure 6.14: The geometry of (a) a divacancy (b) the barrier point to divacancy migration and the geometry and spin density diagram of (c) a divacancy with an electron (d) a divacancy with an electron at the barrier point. Anions are depicted in red, and cations in blue. Spin density iso-surfaces of a value of 0.001 are also shown in the negatively charged cases.

CsBr/KBr to a wider distribution for CsBr/Cu, with a peak at a lower energy and a high energy tail. The lack of thickness dependence of the CsBr/Cu films suggests that this attenuation is not due to direct interaction between activity on the surface of the films and the metal substrates. Theoretical calculations suggest that the difference between desorption from insulating and metal substrates can be explained by a model of electron trapping at low-coordinated sites at the interface. Figure 6.15 illustrates the proposed model from desorption induced by sub-bandgap 6.4 eV photons from CsBr films grown on insulating LiF and metal Cu substrates.

The top of the figure represents desorption from CsBr films grown on insulating

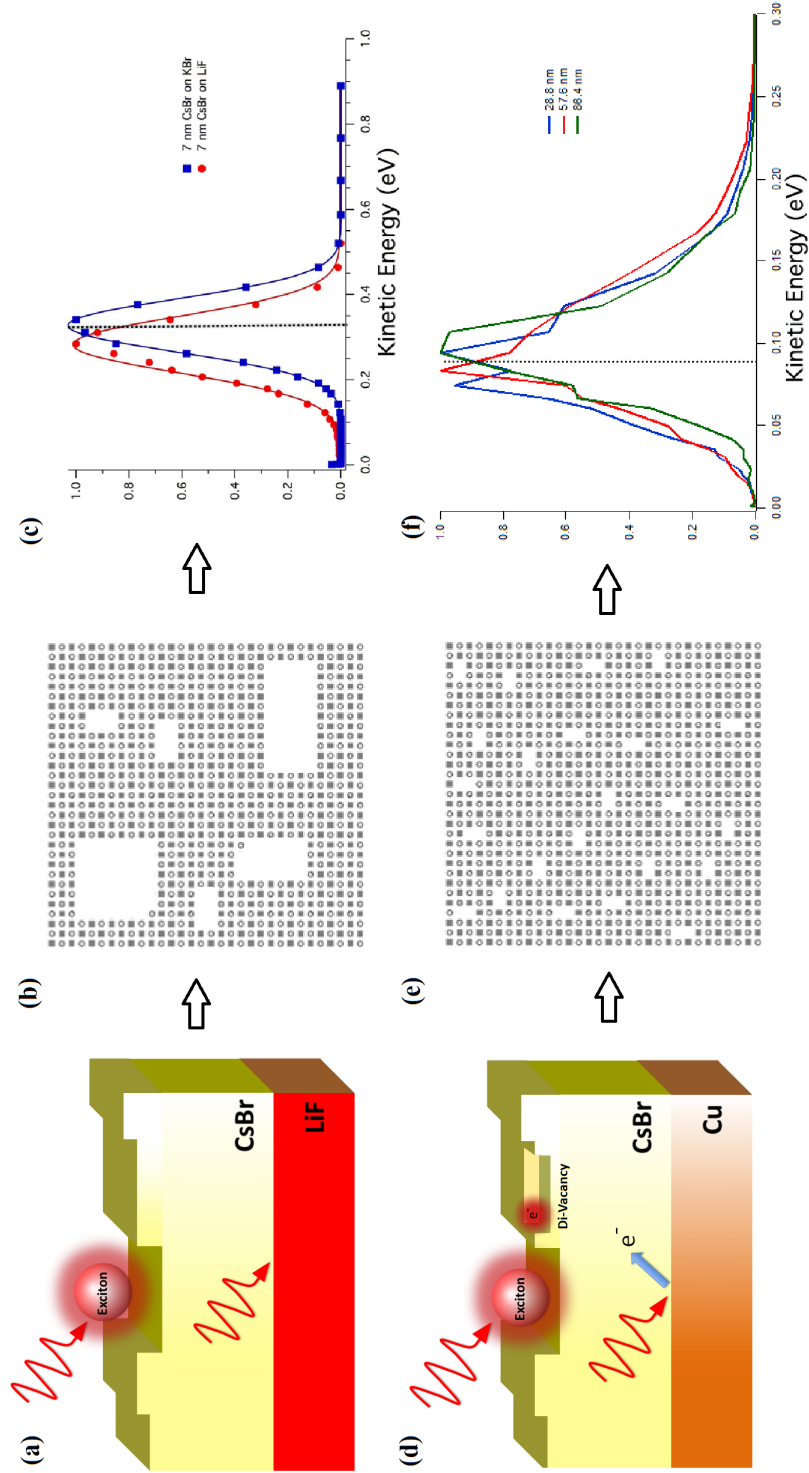


Figure 6.15: Desorption following irradiation of CsBr films on insulating and metal substrates (below and above, respectively.), including a snapshot of the morphology of the surface during irradiation, and resultant Br kinetic energy distributions.

substrates. In (a), incident 6.4 eV radiation can interact with the surface, creating an exciton which can subsequently relax by emitting a Br atom at hyperthermal velocities. Exciton relaxation leaves vacancies at the surface which may subsequently agglomerate due to the low migration barrier to neutral vacancy and divacancy diffusion on the surface, leaving behind characteristics 1ML pits shown in (b), similar to the AFM images of electron irradiated KBr produced by Bennewitz et al. Exciton relaxation occurs by emitting Br atoms of energies well fit to a Gaussian which peaks around 0.35 eV, as in (c).

The bottom of Figure 6.15 represents the model for desorption induced by 6.4 eV radiation on CsBr/Cu films. Photons can, as (a), interact with the surface creating excitons. In contrast to insulator-grown films, photons may pass through the films and induce photoemission of electrons from the underlying substrate, as in (d). These electrons may trap at low-coordinated sites at the surface, such as vacancies, divacancies, kink and corner sites. In particular, exciton relaxation leaves Br vacancies at the surface. Photoemitted electrons can then induce cation desorption by exciting F-centres on the surface. Divacancies on the surface are stabilised by electrons: trapped electrons raises the barrier to diffusion substantially, quenching this effect. As such, we expect the surface to resemble (e), a series of divacancies which do not agglomerate. Furthermore, calculations suggest that significant desorption does not occur at excitons created at divacancy sites, as excitons at these sites are of lower energies, such that Br desorption is no longer energetically favourable. As a consequence of electrons trapped at the surface, the negative charge reduces the energy of excitons at the surface due to Coulombic attraction between the hole and surface charge. Desorbed Br atoms have a much reduced energy, peaking at around 0.075 eV, as in (f), due to negative charge on the surface.

Experimental measurements and theoretical calculation both suggest electron-trapping at the CsBr surface. We note that AFM images by Bennewitz et al. of KBr are taken after electron bombardment has taken place. If the images represented a snapshot in the dynamically-evolving layer-by-layer surface during irradiation of the CsBr surface then the desorbed Br distribution would resemble that of CsBr on insulating (i.e. LiF or KBr) surfaces, peaking around 0.3 eV. On the Cu(100) surface this is not the case, peak kinetic energy occurs at significantly lower energies (< 0.1 eV). Due to

triplet exciton relaxation at the surface, anion vacancies are produced during the radiation process. Electron photoemission from the Cu substrate facilitates the emission of cations adjacent to anion vacancies (F-centres). Therefore divacancies should be created on the surface during irradiation. Kelvin Probe measurement and reduced kinetic energy of emitted Br atom supports the model that negative charge at the surface limits the energy available for Br desorption. We propose that divacancies on the surface are interacting with photoemitted electrons in a dynamic process of electron escape and replenishment by the electron flux emitted from the metal substrate, and that these electrons stabilise divacancies at the surface, leading to a surface characterised by numerous negatively charged divacancy sites, in contrast to the uncharged surface where we expect divacancies to diffuse easily and coalesce into larger clusters.

Subsequent desorption from divacancy sites is energetically unfavourable and inhibited by electron trapping at the defect sites. As a result, if divacancies are the most numerous electron traps at the surface, we would expect desorption to diminish in terms of absolute number of Br atoms and their kinetic energy as the experiment progresses, until the surface is saturated with negatively-charged divacancy sites, and desorption ceases. Consequently, irradiated CsBr films on Cu should degrade at a slower rate than those grown on insulating substrates. This suggests that CsBr films on Cu are robust and resistant to material degradation during ultraviolet laser exposure, and that desorption should significantly decrease after desorption of the surface layer. These results provide new insights into the mechanisms of structural evolution of alkali halide films on metal substrates, and the activation and function of metal photocathodes that have been coated with CsBr protective films.

In conclusion, we have extended models of desorption from CsBr grown on insulators to desorption from CsBr grown on a metal substrate. A model for Cs desorption has been outlined. Electrons photoemitted from the metal may trap at low-coordinated sites and defects on the surface, inhibiting hyperthermal relaxation by Br desorption, and reducing the energy available for desorbing Br atoms. The trapping of electrons at divacancy sites acts to minimise atomic desorption, such that the films grown on a metal are predicted to degrade less than films grown on insulating substrates.

Chapter 7

CsBr films and their effect on the work function of Cu

The aim of this chapter is to gain insight into how the work function of bulk Cu is altered by CsBr thin films, with particular attention to the reduction of work function as a function of coverage and thickness of film. The effects of including van der Waals forces are examined, as is the effect of interfacial separation between film and metal on the work function. Br and Cs vacancies and divacancies at and around the interface are also examined. A mechanism of laser activation (LA) is proposed, whereby the creation of divacancies on the CsBr surface, their diffusion into and around the bulk, and their subsequent segregation to the interface leads to a reduction of work function after a period of irradiation.

7.1 Introduction

As discussed in detail in the introduction to this thesis, CsBr coatings films applied to Cu photocathodes have been widely observed to increase the QE of the photocathodes by many orders of magnitude, with estimates ranging from around 50 to 77 times increased yield with respect to uncoated Cu. The increase in QE is widely believed to result from a reduction of the work function of the film, reducing the energy required to extract electrons from the metal. This assumption is partly based on Spicer's three-step model for photocathodes, and is discussed further here[219]. CsBr/Cu photocathodes therefore have the potential to greatly reduce the operating costs of XFEL facilities. Despite the extensive experimental research into the physical characteristics (including efficacy under irradiation, transverse momenta of emitted electron, emittance etc.) of

such photocathodes, the origin of the initial increase in QE and the further increase measured following so-called laser activation (LA) remain unknown, and theoretical models of photocathodes is non-existent in the literature.

The dearth of theoretical models is the case in spite of the large amount of experimental research into the viability of CsBr/Cu as a future photocathode material, although experimental measurements of the work function reduction due to the application of thin films vary widely. A study in high vacuum conditions of CsBr thin films (7 nm) deposited on Cu in an effusion cell at 425°C has measured the work function using XPS as 3.75 and 3.45 eV initially and after the activation period, respectively[54]. The same study measured the work function of bare Cu as 4.2 eV, which is 0.4 eV off the widely accepted literature value of 4.6 eV[220]. The underestimation has been ascribed to contamination of Cu with air, leading to formation of CuO on the surface. These measurements suggest a change in the work function of approximately 0.8 - 1.2 eV. The discrepancy may be due to the high vacuum conditions used in the experiment (as opposed to ultra-high vacuum conditions), which may lead to background contaminants penetrating the insulating films. CsBr is well-known to be a highly hygroscopic material[57].

Other studies have estimated the maximum change in work function following film deposition to be of the order of 2 eV[221]. It is perhaps significant that these studies have subjected the Cu films to an extensive cleansing process with HCl prior to experiment in order to clean contaminants from the metal. It seems probable that the wide discrepancy between measured work function of CsBr/Cu can be attributed to contamination/structural differences at the interface. In the light of the ambiguous experimental information we conclude that a work function reduction of 1 - 2 eV is possible following deposition of CsBr films on Cu(100).

A study of CsI deposited on Cu has by contrast measured an extremely large reduction of the work function, of 2.85 eV, and a QE enhancement factor of 2700 following laser activation[56]. The large work function reduction has been attributed to metal formation at the interface. As CsBr is chemically similar to CsI one might expect similar behaviour for CsBr/Cu photocathodes, however this is not the case. It appears that the LA of CsBr and CsI corresponds to qualitatively different transformations of the atomic structure of the underlying materials. Both the formation of a defective inter-

face and formation of metal have been suggested as being responsible for work function change during LA, although neither experiment nor theoretical calculations have been published which provide direct evidence to support either conjecture.

As the variation of the change in work function following film deposition is large, insight can be gained by theoretical modelling into the underlying mechanisms which contribute to work function reduction. The structure at and around the interface is likely to effect the work function reduction. Insulating films are well understood to reduce the work function of substrate metals in two distinct ways; firstly, by compression of the surface electronic wavefunctions in the metal by Pauli repulsion of the insulating films[222, 223], which consequently raises the kinetic energy of the electrons occupying surface states, and thus the Fermi energy. Insulating films may also induce charge transfer from film to metal, creating a dipole across the interface which reduces the energy barrier to electron escape[224]. In addition, modification of the structure at the interface following film deposition may affect the work function.

The aim of this chapter is to gain insight into the mechanisms by which various structural factors, such as film thickness, coverage and interfacial separation between film and metal affect the work function of the CsBr/Cu system, using DFT calculations. We then proceed to outline models of photo-induced creation of Br and Cs vacancies in CsBr/Cu, which diffuse towards and segregate at the interface. We provide evidence for the proposition that film depletion at the interface due to defect diffusion is the origin of LA.

7.2 Experimental Background

Experimental studies have examined the change in photoemission characteristics of Cu with and without a thin film coating of CsBr. A graph of the variation of QE after irradiation with a 266 nm laser (4.66 eV) of CsBr films deposited on Cu as a function of time is illustrated in Figure 7.1.

There are two major effects on the QE due to the deposited film: (1) a step change increase at time zero, and (2) a further increase after a prolonged period of irradiation over a period of hours. A theoretical study has derived an expression for electron emittance of a photocathode which identifies the work function as of particular importance[225] and suggests a reduction of the work function will result in increased

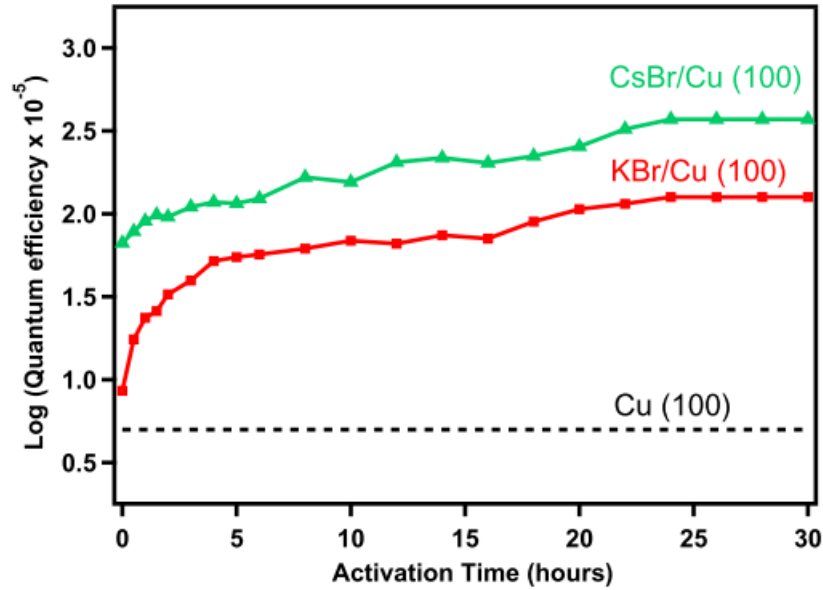


Figure 7.1: The variation of the logarithm of QE with time during irradiation with 4.66 eV light. The quantum efficiency of bare Cu is included for reference. Copyright of AIP publishing[5].

	CsBr/Cu(100)			CsI/Cu(100)	
Film thickness (nm)	1.8	3	6	3	8
Cs lost after activation	31%	2.5%	1.5%	11%	3.6%
Br/I lost after activation	49%	5.0%	4.0%	36%	5.4%
Cs remaining/Br or I remaining	1.35	1.03	1.01	1.39	1.02

Figure 7.2: Relative depletion of Cs and Br after LA for films of various thicknesses. Copyright of AIP publishing[5].

QE.

Following these studies, if we assume the work function change is responsible for the increase in QE of the photocathodes, these results suggest that the work function of the CsBr/Cu film undergoes processes which have the effect of further reducing the work function during LA. Moreover, this secondary effect, distinct from the work function reduction induced by compression of the electronic wavefunctions at the surface, is a relatively slow process that takes approximately twenty four hours to reach the maximum shift (see Fig. 7.1), after which an equilibrium QE is attained.

Another study of thin films of CsBr and CsI deposited on Cu has measured an increase in the QE and decrease in the work function for both alkali halide films with

respect to the bare Cu photocathode[56]. XPS core level spectra of the UV-irradiated thin films, ranging from 1.8 nm to 6 nm, suggest depletion of both Cs and Br from the films. The depletion of Br is however larger than Cs, and the discrepancy increases as the thickness of the film decreases (see Fig. 7.2). These results suggest atomic depletion occurs most readily at or close to the interface with UV-irradiated thin films, however how the surface and interface of CsBr/Cu evolves with insulating films of increased thickness remains unclear.

7.3 Methodology

In order to model the hybrid CsBr/Cu system, a slab model with two dimensional PBCs has been used. Two 4-layer surfaces of (8 x 8) and (10 x 10) surface unit cells (288 and 392 atoms) have been constructed to model the Cu(100) surface, with clusters of CsBr placed above the structure. The exchange-correlation energy has been calculated using the PBE (GGA) functional as implemented in the CP2K code. Pseudopotentials have been used to model the core electrons, with double zeta Gaussian basis sets (DZVP-MOLOPT-SR-GTH) used to describe the valence electrons of the Cs($4s^2 4p^6 5s^1$), Br($4s^2 4p^5$) and Cu($3d^{10}$) ions, with a 200 Ry plane wave cutoff for the auxiliary grid. Large Cu surfaces have been used so as to give a large degree of freedom to place clusters of various sizes and orientations on the surface and are necessary in order to correctly reproduce the band structure of the metal. The CP2K calculations have been conducted at the Γ -point, which also necessitates a large number of atoms. As the calculation of HF exact exchange scales as $O(N^4)$, and the number of atoms in the system is large, standard GGA semi-local functionals have been utilised instead of hybrid functionals[80]. Moreover, hybrid functionals are known to have problems representing metallic systems, they may for example distort the band structure of metals, and consequently incorrectly describe the screening behaviour[99]. We note that previous studies[81, 82] of the MgO/Ag system found little difference in the interfacial separation as calculated under the semi-local PBE functional, and the hybrid functional HSE06[226].

Grimme's dispersion correction (PBE + D2) has been used in some calculations in order to estimate the effect of including van der Waals forces. The inclusion of dispersion forces has been shown to have a crucial effect on, for example, the adhesion

energy of organic molecules at metal surfaces[227]. Although there have been recent developments in functionals which include van der Waals forces[87, 88, 89], these remain largely untested for metal-insulator systems. As such, the D2 correction has been tested, although it is known to have a tendency to overbind between metals and insulators[228, 229]. This is probably a partial consequence of the D2 parameters having been derived from insulator-insulator interactions. Parameters for the Br^- and Cu^+ ions have been taken from Grimme's original paper[90], with those for Cs^+ taken from a recent study[230].

The lattice parameter of bulk CsBr has been calculated as 4.365 Å in the PBE description, marginally larger than 4.336 Å under the PBE0 description, 1.6% and 0.9% off the experimental value of 4.295 Å, respectively. A VASP plane-wave model of bulk CsBr with the PBE functional calculates the lattice parameter as 4.358 Å, suggesting the basis set is sufficiently large. The geometry of the bare Cu(100) surface with and without clusters of CsBr have been calculated by full relaxation of all ions. The lattice parameter of bulk Cu was calculated as 3.61 Å, in agreement with the experimental measurement of 3.61 Å[231].

The work function has been estimated by constructing a 1D-averaged potential in the z-direction, that is, by taking an average of the potential at each point in the x-y plane. The reduction of the work function is then calculated as the difference between the potential at each interface with the vacuum of the CsBr/Cu system, i.e. the potential at the bottom of the slab below the Cu surface, and the potential at the top layer of the CsBr surface. The 1D-averaged electrostatic potential of a 2ML CsBr film placed on the Cu surface is depicted in Figure 7.3.

In addition to the CsBr/Cu model, a model of bulk CsBr has also been constructed in order to calculate the barriers to divacancy diffusion in the bulk. A 216-atom unit cell has been constructed using CP2K with the electronic structure calculated using the PBE0 + D2 functional. The climbing-image nudged elastic band (CI-NEB) method[232, 233] has been used to construct the minimum energy pathway for divacancy diffusion via both Br and Cs ion motion. The barrier has been estimated as the difference in energy between the highest and lowest points along the potential energy surface.

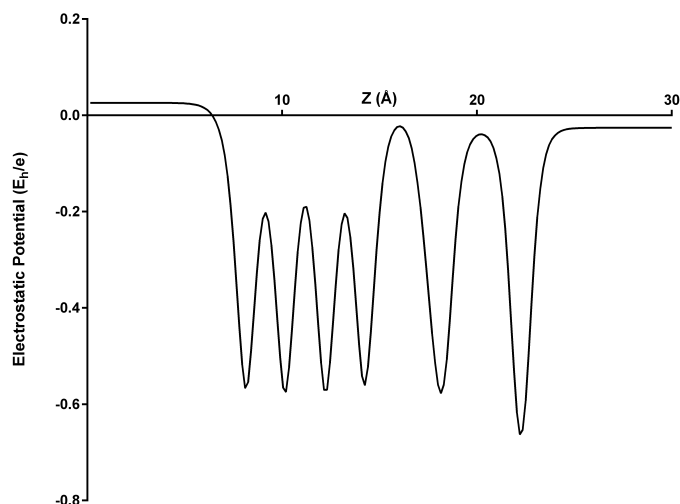


Figure 7.3: The 1D-averaged electrostatic potential across the CsBr(2ML)/Cu slab, where z denotes the displacement in the z -direction and the electrostatic potential is on the y -axis given in units of Hartrees per the charge of an electron. The work function is estimated as the difference in the potential at the minimum and maximum values of z .

7.4 Results

7.4.1 CsBr Films and Reduction the Cu Work Function

The work function of the 288- and 392-atom Cu(100) surfaces have been calculated as 4.47 and 4.53 eV, respectively, close to the literature value of 4.59 eV[220]. In order to test the effect of the size of the Cu surfaces on the relevant energetics of the system, the formation energy of a Cu vacancy at the surface has been calculated as 3.91 and 3.90 eV on the 288 and 392 atom systems, respectively. The adsorption energy of a Cs atom was calculated as 1.78 eV on both surfaces. Due to the close agreement between calculated formation energies and work function between the two surfaces, the 288 atom surface was regarded as sufficiently large to reflect real film results for most purposes, and has been used for all calculations unless otherwise specified. The calculated density of states (DOS), with the experimental XPS determined DOS inset is illustrated in Figure 7.4.

As CP2K is restricted to making calculations at the Γ -point, a very large number of atoms are required in order to produce smooth DOS plots. The calculated spectrum is rough, however it reproduces the pertinent features of the experimental DOS. There is a large asymmetric peak, with a small shoulder close to the vacuum level energy. The gradient of the peak increases sharply as the energy of the states decreases. Con-

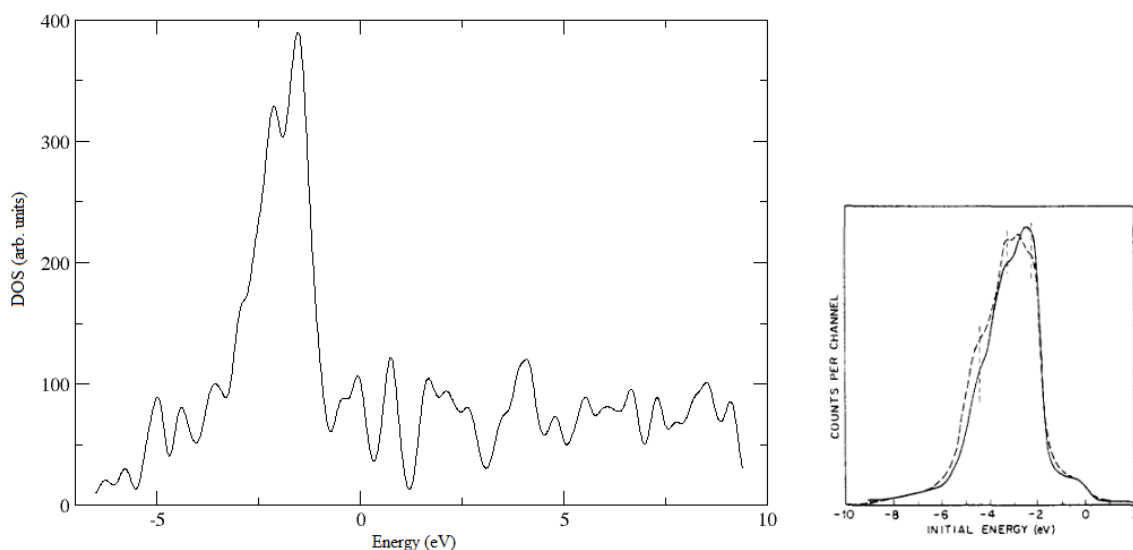


Figure 7.4: The calculated DOS for the Cu(100) surface is displayed on the left, with the experimental XPS density of states inset on the right. Copyright of Elsevier[6].

sequently, a reduction of the work function of the order of 1 - 1.5 eV will dramatically raise the number of electronic states of the bulk accessible to incident photons, and consequently lead to an exponential increase in QE of the photocathode with respect to bare Cu. This is one possible explanation of the observed increase in QE following the application of thin CsBr film coatings. This is based on the Spicer three-step model[219] and is discussed further in the introduction.

The 288-atom surface has been used to calculate CsBr films of full coverage, i.e. the perfect interface. CsBr films of 2, 3, 4 and 5 molecular layers (MLs) have been placed on the Cu(100) surface, and allowed to relax. The geometry of the CsBr(2ML)/Cu films is displayed in Figure 7.5.

The interfacial separation is defined as the difference in the average z-coordinate of atoms composing the top layer of the Cu(100) surface, and the average of the Br and Cs atoms composing the interface layer in CsBr. The calculated interfacial separation and reduction in work function of the CsBr/Cu films as a function of the number of MLs is in Table 7.1.

The 2ML film has an interfacial separation of 3.45 Å, which decreases by a few hundredths of an Angstrom for thicker films. The work function reduction is about 1.4 eV for the 2ML films, rising to 1.5 eV with thicker films. The thin films converge to thick film values for interfacial separation and work function reduction by 2 and 3MLs, respectively. The sensitivity of the measured work function with respect

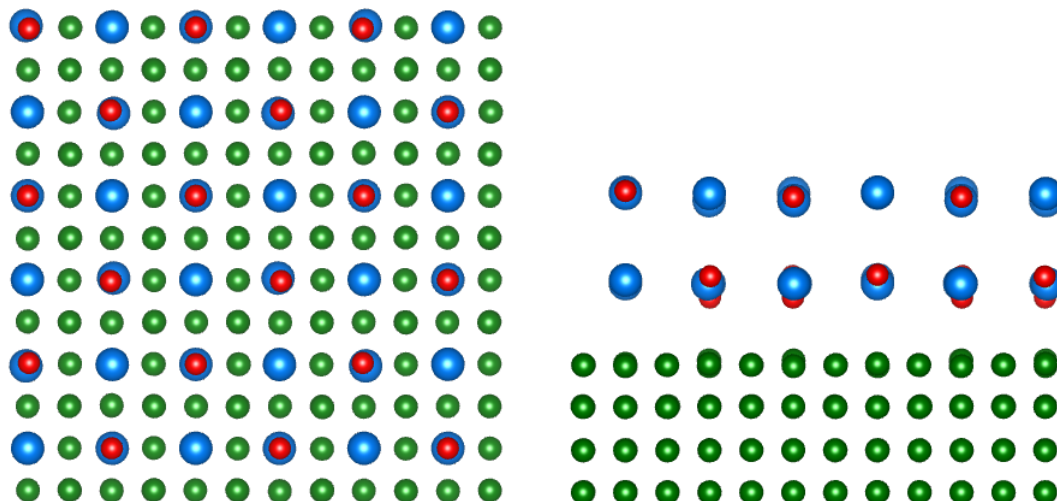


Figure 7.5: The unit cell of CsBr(2ML)/Cu(100). The Cs ions are depicted in blue, Br ions in red, and Cu ions in green.

	MLs	d (Å)	$\Delta\phi$
CsBr/Cu(100)	2	3.45	1.41
	3	3.42	1.48
	4	3.42	1.51
	5	3.42	1.51

Table 7.1: The change in the work function as a function of thickness of CsBr film, where d represents the interfacial separation and $\Delta\phi$ the reduction of the work function in eV.

to interfacial separation is well attested in the literature, and is a consequence of the increase/reduction of the surface dipole[222, 223]. As a result of these calculations, 4ML films were considered sufficiently thick to represent the thicker films used in experiment (which range from 3 - 7 nm) from which the work function reduction has been measured[54, 56].

In order to explicitly examine the relationship between work function and interfacial separation, a series of single point calculations have been conducted, from a minimum of 2.5 Å to a maximum of 4 Å, in increments of 0.1 Å. A graph of the variation of the work function reduction as a function of interfacial separation is depicted in Figure 7.6. The relationship appears linear to a good approximation. The range of experimental estimates corresponding to a reduction of the work function in the range 1 - 2 eV is equivalent to interfacial separation values between film and metal in the range 3 - 4 Å.

Previous studies of metal-oxide interfaces have found a better agreement with ex-

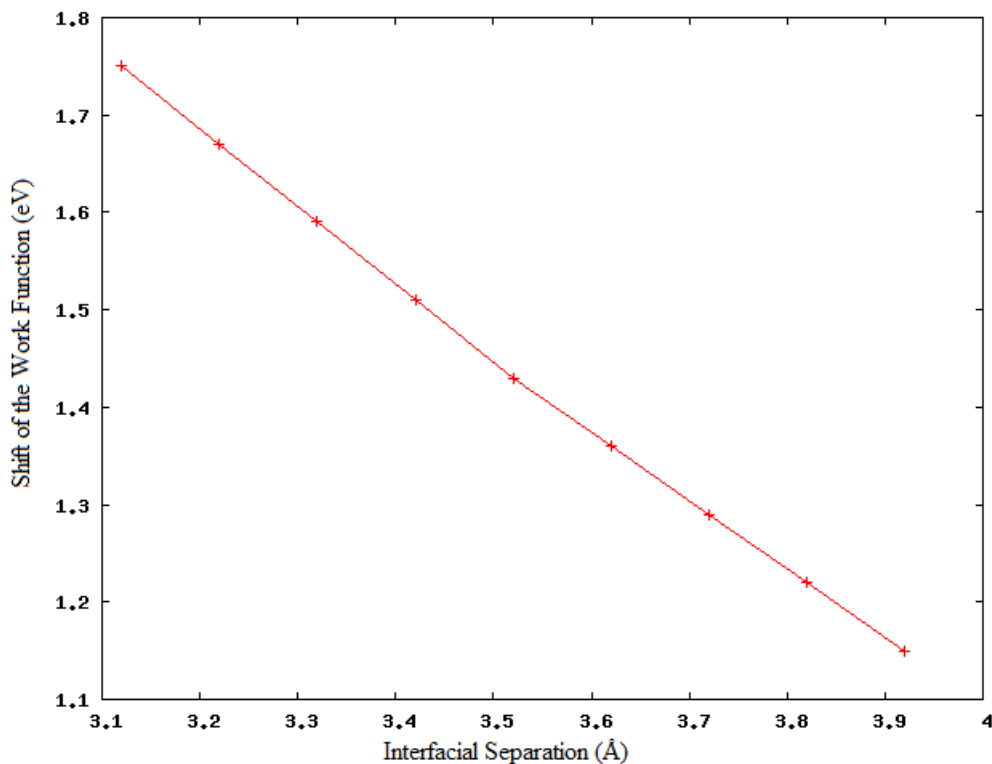


Figure 7.6: The variation of the work function shift for 4ML films as a function of interfacial separation.

	MLs	d (Å)	$\Delta\phi$ (eV)
CsBr/Cu(100)	2	3.00	1.76
	3	2.99	1.93
	4	2.99	1.89

Table 7.2: The change in the work function as a function of thickness of CsBr film with the inclusion of van der Waals forces, where d represents the interfacial separation, and $\Delta\phi$ the reduction of the work function.

perimental interfacial separation with the inclusion of van der Waals forces[82]. In order to include dispersion forces in these calculations, Grimme's D2 dispersion correction has been included. Although there are more complex dispersion corrections, such as the D3 correction[234], which has less empirical parameters, the performance of D2 has been shown to yield metal-insulator interfacial distances closer to experiment[81], as well as having the advantage of being relatively conceptually simple.

The inclusion of van der Waals forces decreases the interfacial separation of the metal and substrate as expected, which amplifies the compression effect of the electronic wavefunctions at the surface of the metal. The reduction is about 0.45 \AA . This leads to a further reduction in the wave function in all cases, of approximately 0.25

eV. The change in work function as a function of layers of complete coverage with the inclusion of D2 forces is in Table 7.2.

Although it is expected that this effect should be slightly mitigated by the reduction of rumpling of the CsBr films at the interface, comparison with the variation of work function reduction as a function of interfacial separation (see Fig. 7.6) suggests that films calculated without dispersion forces (i.e. PBE instead of PBE + D2) should yield a similar reduction at this decreased interfacial separation.

The inclusion of Grimme's D2 correction raises the calculated work function shifts to the higher end of experimentally reported values after the activation period of photocathodes. As noted in the methodology section of this current chapter (section 7.3) D2 forces are known to have a tendency to overbind, particularly in cases where the parameters that have been defined for insulator-insulator interactions are used to model metal-insulator interactions. As the inclusion of D2 dispersion forces can be seen to reduce the work function to the same degree as PBE calculated films (i.e. without D2 forces) at a similar interfacial separation, and there is some uncertainty as to the accuracy of the D2 correction, they have not been included in all other calculations, as they do not add greatly to the physical understanding of the real CsBr/Cu system.

7.4.2 CsBr Films of Partial Coverage

A study of CsBr grown on KBr(100), which has a similar lattice parameter to Cu(100), has examined the structure of film growth using reflection high energy electron diffraction (RHEED) techniques. Growth was found to be predominantly layer-by-layer in character (i.e. Frank-van der Merwe-type growth), although initial nucleation appeared to include imperfections at the interface[2] (see Chapter 4). It is possible that the large variation in experimentally measured reduction of the work function (1 - 2 eV) of CsBr coating films may reflect a difference in film quality between those measured in different experiments.

In order to simulate films of different coverages, or films with a depleted interface, clusters of 2, 3, and 4 ML thickness have been placed on the 392-atom Cu(100) surface and the resulting change in the work function tabulated. The calculated geometry of the clusters is displayed in Figure 7.7, and the shifts of the work function are in Table 7.3.

The shift of the work function increases with both coverage and the thickness of

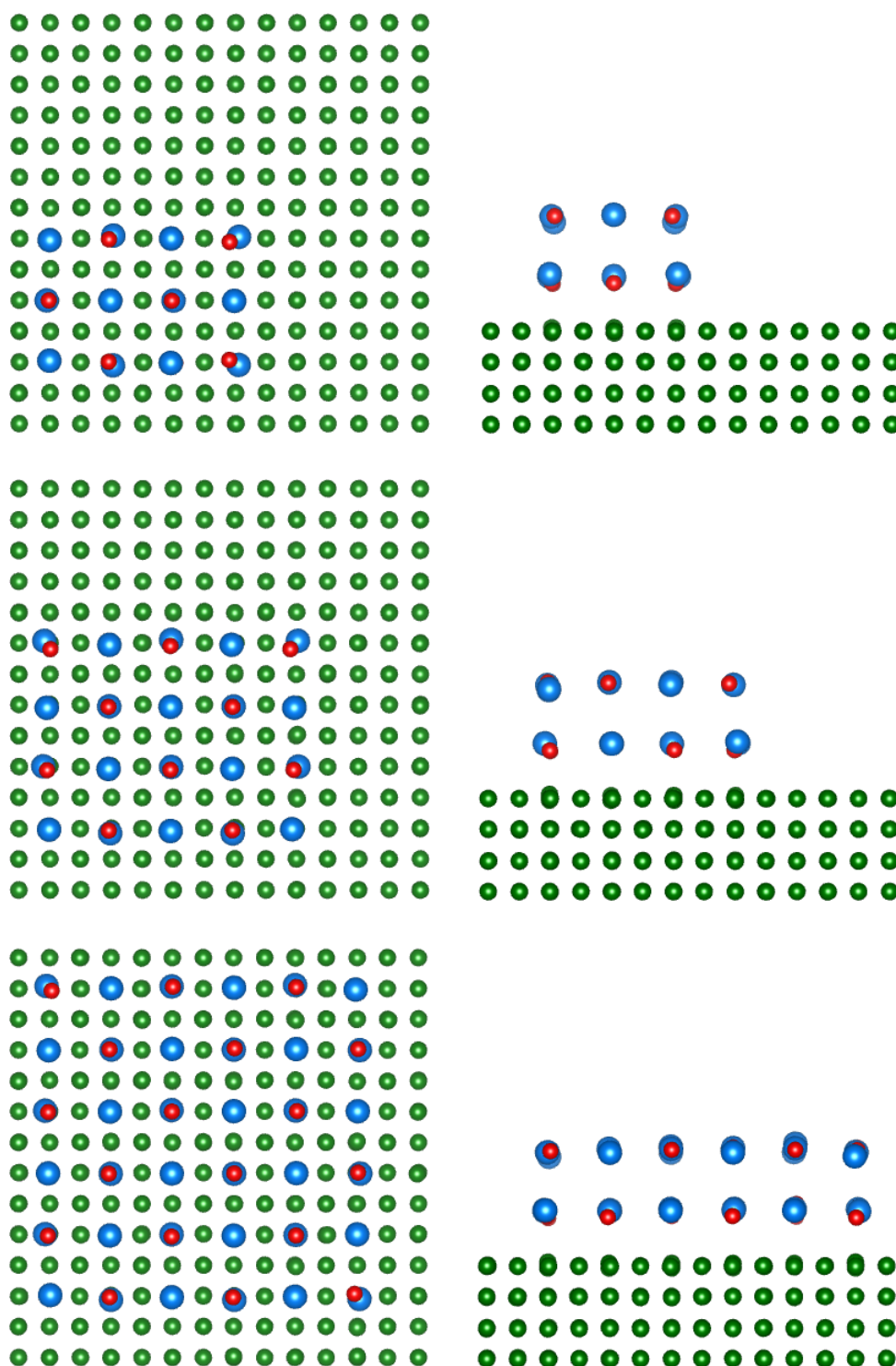


Figure 7.7: The geometry of 24-, 40- and 72-atom 2ML clusters of β -CsBr, from top descending, corresponding to coverages of 21%, 36% and 75%, respectively.

	Coverage	MLs	ϕ	$\Delta\phi$
CsBr/Cu(100)	21%	2	3.44	1.09
		3	3.29	1.24
		4	3.23	1.30
	36%	2	3.11	1.42
		3	3.03	1.50
		4	2.95	1.58
	75%	2	3.03	1.50
		3	2.95	1.58
		4	2.93	1.60

Table 7.3: The change in the work function as a function of CsBr cluster size and molecular layers. All energies are in eV. The work function of bare Cu is calculated as 4.53 eV.

deposited clusters. The change is most dramatic with initial CsBr coverage, with the work function reducing at a slower rate than coverage. 4ML clusters of 21% and 75% coverage have calculated work function shifts of 1.3 and 1.6 eV, respectively. The change from 3 to 4 MLs is also less than a tenth of an electron volt in all cases, similar to the results for CsBr films of full coverage (c.f. Table 7.1).

The reduction in work function as a result of the CsBr clusters at the higher end of coverage is actually larger than those calculated for perfect films, i.e. films nominally of 100% coverage. This is partially explicable to the dipoles which exist at the corners of CsBr clusters. The clusters also in general have a smaller interfacial separation than the perfect films, of the order of 0.1 Å, which will act to further decrease the work function. In theory there will also be residual spurious interactions between dipoles of other periodically repeated cells. Attempts were made to estimate the magnitude of this interactions, although due to the complexity of the situation, no analogous corrections could be found in the literature, and investigating this further was considered beyond the scope of this study.

7.4.3 Mechanisms of Laser Activation

The LA of a photocathode refers to the phenomenon of the increase in QE following a period of laser irradiation with 4.66 eV photons. The QE steadily increases until an equilibrium QE is attained. It has been suggested that LA is due to defect formation in the films, and their behaviour at and around the interface. F-centres have been selected as candidates for so-called intra-band-gap adsorption states (IBASs), the existence of which has been posited as being responsible for the increase in QE in CsBr/Cr photo-

	Layer	E_{Form}	$\Delta\phi$
CsBr(4ML)/Cu(100)	1	3.58	-1.57
	2	3.98	-1.66
	3	3.95	-1.65
	4	4.34	-2.04

Table 7.4: The calculated formation energy (E_{Form}) of an F-centre in different layers of the deposited CsBr, where 1 represents the layer at the interface, 2 the 2nd layer from the interface and so forth, with the corresponding shift of the work function ($\Delta\phi$). Formation energies have been calculated with reference to a Br atom, as specified in the text. All energies are in eV.

cathodes, by functioning as electron injectors.

The irradiation with 4.66 eV laser energies, which is below both the surface and bulk exciton thresholds, is such that defects can only be created as a result of two-photon processes. The fact that any LA is a result of two-photon processes may partially explain the long activation period (~ 24 hrs). Excitation of the surface has been shown to result in F-centres on the surface in Chapter 4. Exciton creation in the bulk should also lead to the creation of F-H pairs, leading to depletion of Br atoms in the bulk, and F-centres in the bulk of the film, as suggested by models outlined in Chapter 4.

Calculations in Chapter 5, concerning desorption experiments from CsBr/Cu films suggest the irradiation of the films leads to desorption of Cs atoms from the surface, via a model of F-centres excited by photoemitted electrons. This leads to the creation of dimer anion-cation vacancies at the surface (divacancies). Below we examine the effect of F-centres, cation vacancies and divacancies on the work function reduction of the Cu(100) surface.

7.4.3.1 F-centres at the CsBr/Cu Interface

F-centres have been modelled in the 4-layer CsBr films at the interface, and in the 2nd, 3rd and 4th layers, by removing a Br atom, and allowing the system to relax. The formation energy has been defined as the difference in energy between the system with an F-centre, and the defect-less interface and a Br atom at infinite separation. Table 7.4 shows the calculated formation energies for F-centres at these positions and in a 216-atom β -CsBr bulk unit cell.

The F-centre formation energies in the thin film are smaller than the calculated bulk formation energy by approximately 2 eV. The lowest energy site is at the interface,

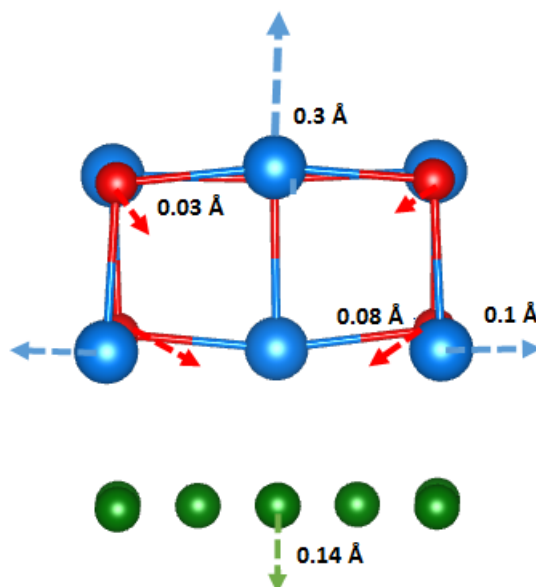


Figure 7.8: The local geometry of an anion vacancy at the interface, with the nearest neighbour displacements, where the length of the arrow is approximately proportional to the magnitude of displacement. Anions are red, cations blue, and the Cu ions depicted in green.

which is 0.4 eV lower in energy than the 2nd layer configuration. A spin density plot of the F-centre in the interface layer shows that the unpaired electron is donated to the metal and is fully delocalised over the surface. The local geometry of the defect is displayed in Figure 7.8.

The reduction in work function due to the F-centre at the interface before relaxation is calculated as 1.70 eV, such that the relaxation acts as to minimise the work function reduction induced by the charge transfer. As a result of the electron donation to the metal, the defect is formally positively charged, such that it resembles an F⁺-centre, with neighbouring anions relaxing towards and cations away from the defect. The positive charge of the defect is consistent with our understanding of F-centres in the bulk, (see Chapter 3), where the occupied energy level of the (neutral) F-centre is approximately 2 eV below the vacuum level, whereas the Fermi energy of the metal following deposition of the film is approximately $(4.6 - 1.5) = 3.1$ eV below the vacuum level (see Table 7.1), i.e. lower than the F-centre level, such that we expect electron donation from F⁰-centres to the metal when the vacancy is close enough to the interface. Spin density plots of the F-centre in all layers of the films show that the electron is donated to the metal in all cases.

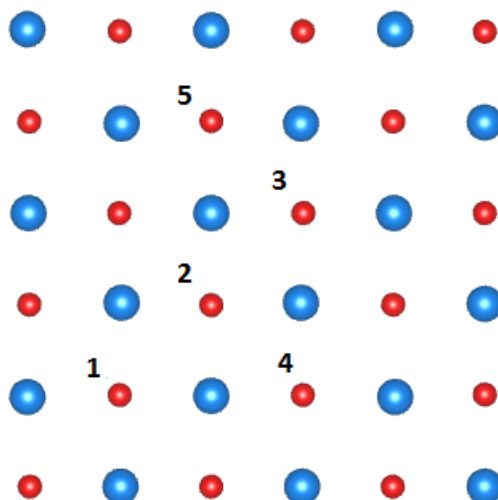


Figure 7.9: All unique combinations of two F-centres at the interface in the unit cell. F-centres have been modelled at site 1 and 2, 3 and 4.

	Position	E_{Form} (eV)	$\Delta\phi$ (eV)
CsBr(4ML)/Cu(100)	2	7.15	1.53
	3	7.12	1.54
	4	7.14	1.54
	5	7.08	1.54

Table 7.5: The calculated formation energy (E_{Form}) of a pair of F-centres, where the positions are indicated in Figure 7.9, with position 1 always a vacant site. The corresponding shift of the work function ($\Delta\phi$) is in the column on the right.

The migration energy of an F^+ -centre has been estimated as 0.3 eV in bulk α -CsBr in Chapter 3. If we assume a similar barrier here, we can expect F^+ -centres to be mobile at experimental temperatures. As the defect is positively charged, this induces polarisation of the metal, which gives rise to a force on the defect in the direction of the interface. Furthermore, the interface layer has been identified as the lowest energy configuration for the defect, such that F-centres in the vicinity of the metal should migrate towards the interface. The work function of the system reduces by approximately 0.07 eV due to the vacancy.

In order to simulate a high concentration of F-centres at the interface, two F-centres have been modelled in various configurations in the interface layer. Figure 7.9 displays the vacancy sites, with the corresponding formation energies in Table 7.5.

As the defects are positively charged, they experience mutual Coloumbic repulsion with each other, and the most energetically favourable configurations correspond to positions where the separation between the two F^+ -centres is maximised (i.e. a pair of

F^+ -centres at positions 1 and 5 are of lower energy than at positions 1 and 2). Despite this, all combinations are very close in energy, suggesting that this effect is to some extent diminished as the energy cost due to movement of ions neighbouring the defects is small as a result of shared relaxation. As the size of the unit cell restricts modelling of F^+ -centres at larger distances from each other, we conclude that these calculations are either at or above saturation density of Br vacancies at the interface, as the repulsive electrostatic forces inhibit higher densities of charged vacancies. The work function further reduces by approximately 0.05 eV with respect to the isolated F^+ -centre case. Based on these calculation it can be concluded that high densities of F^+ -centres at the interface induce a reduction of the work function by a maximum of 0.1 - 0.15 eV with respect to the clean CsBr/Cu interface, smaller than the reduction that takes place due to LA.

7.4.3.2 Divacancies and Cation Vacancies in CsBr Films on Cu(100)

In Chapter 5 calculations have been conducted which suggest photon-induced cation desorption can proceed via a model of excitation of F-centres at the surface via scattering processes involving photemitted electrons. Here we model a cation vacancy at the interface to investigate the structure of such defects, and the effect they have on the work function. A cation vacancy at the interface has been modelled by the removal of a cation from a 4ML thick CsBr film on the Cu(100) surface. The system has been allowed to relax under the influence of forces. A diagram of the local geometry of the cation vacancy after relaxation is displayed in Figure 7.10a).

The cation vacancy is slightly negatively charged, causing neighbouring cations to relax towards and anions away from the vacancy site. The major asymmetry with respect to the relaxation of the anion vacancy is the minor relaxation of neighbouring Br anions towards Cu(100) surface. As a result of the vacancy the anions are slightly less negatively charged than other anions in the film. The Br anions are consequently less repelled by the slightly negatively charged Cu(100) surface. The change in the work function due to the 4ML film with a cation vacancy is calculated as 1.46 eV, close to the shift in the absence of a cation vacancy (1.51 eV), but slightly smaller. Although the cation vacancy induces a small dipole across the interface, thus repelling electrons, this is ameliorated to some extent by the relaxation of the local anions, such that the net

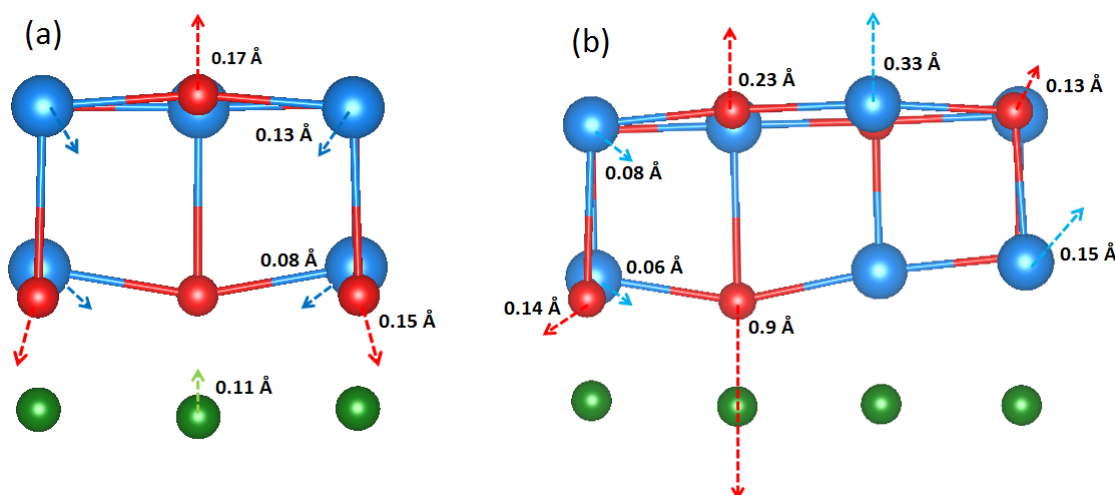


Figure 7.10: The local geometry of a) a cation vacancy and b) a divacancy at the interface, with the nearest neighbour displacements, where the length of the arrow is approximately proportional to the magnitude of displacement.

reduction in work function shift is small.

As argued in Chapter 5, the CsBr/Cu surface should be rich in divacancies whose motion is inhibited by the electron flux travelling through the photocathode. Electrons will trap and discharge from divacancy sites in a dynamic process of electron escape and replenishment.

Divacancies can diffuse through the bulk by a series of 90° rotations due to the motion of neighbouring Cs and Br ions into the vacant sites. The barriers to diffusion via Br and Cs motion have been estimated by using the climbing-image nudged elastic band (CI-NEB) technique, as implemented in CP2K. The barrier has been estimated by calculating the geometry of the initial and final states, and by making an initial guess of the geometry at the barrier point. The minimum energy pathway has been found using a chain of 5 replicas, with the barrier to diffusion then calculated as the difference between the highest and lowest energy replicas along the pathway.

The initial, final and (calculated) geometry at the transition point is illustrated in Figure 7.11. The barriers to motion due to Cs and Br motion are calculated as 0.65 and 0.55 eV, respectively. At these energies we can expect divacancies to move through the lattice, but at a slower rate than H-centres or F^+ -centres, which have barriers of approximately 0.05 and 0.3 eV, respectively.

In order to examine the behaviour of divacancies close to the interface, the divacancy has been modelled in three different configurations: in the interface layer and

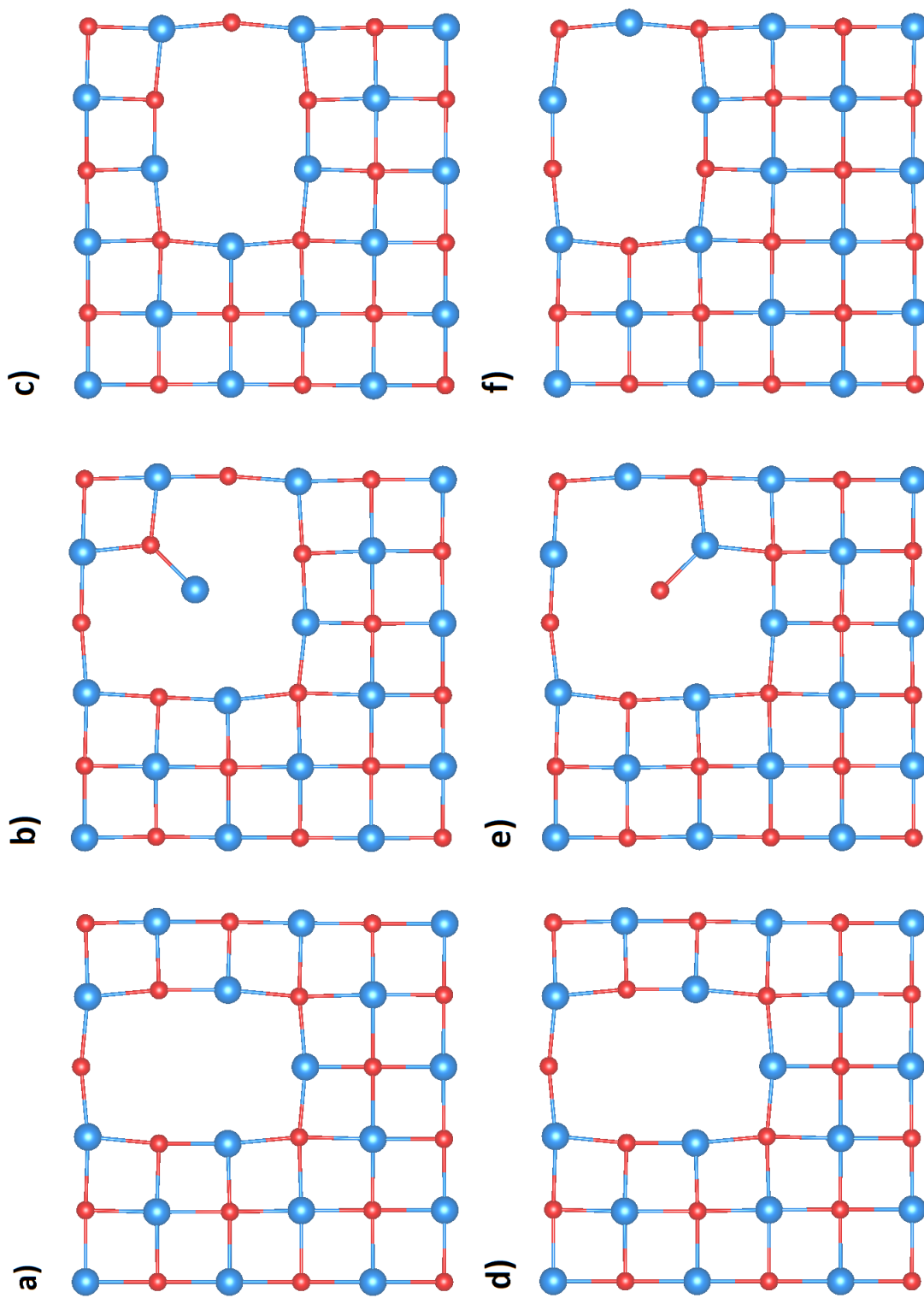


Figure 7.11: The diffusion of a divacancy. The top of the figure shows a) the initial b) saddle point and c) final state towards motion via Cs motion. The bottom shows a) the initial b) saddle point and c) final state towards motion via Br motion. Anions are depicted in red, and cations in blue.

parallel to the interface, and perpendicular to the interface with both the Cs vacancy and the Br vacancy in the interface layer. The lowest energy arrangement was in the interface layer (parallel). The perpendicular arrangement with the Cs vacancy in the interface layer is higher in energy by 0.1 eV, and that with the Br vacancy in the interface layer higher again by 0.6 eV. At the temperatures of experiment (~ 300 K) we can expect divacancies at the interface to alternate between the two lower energy arrangements, with a preponderance of the parallel configuration.

The work function reduction due to the divacancy parallel to the interface is calculated as 0.16 eV with respect to the perfect interface. The shift occurs due to the relaxation of neighbouring ions. The configurations perpendicular to the interface increase or decrease the dipole across the interface in the case of divacancies with the Cs and Br vacancies in the interface layer, respectively. The low energy perpendicular orientation, with the Br vacancy in the interface layer, decreases the work function shift to 1.41 eV, a decrease of around 0.1 eV. The relatively high energy configuration increases the work function shift to 1.68 eV.

The geometry of the divacancy parallel to the interface is depicted in Figure 7.10b). Two Br anions neighbouring the cation vacancy are displaced towards the metal to a large extent (0.9 Å), with the Cu atoms immediately below the Br ions rising out of the surface by 0.3 Å. The Mulliken charge of the Br ions reduces by 0.6e, suggesting bond formation between the Br and Cu ions of the surface, with the Br 4s electron donated to the Cu ions immediately below the anions. Thus a divacancy at the interface effectively induces a charge transfer of two electrons to the metal, as opposed two the transfer of a single electron in the case of the F^+ -centre.

Two adjacent divacancies have been modelled in the interface layer in a square formation, such that they form a tetra-vacancy. The resulting reduction of the work function is calculated as 0.28 eV. The divacancy and tetra-vacancy correspond to ionic depletion at the interface of 5.5% and 11%, respectively. These results suggest that divacancy aggregation at the interface reduces the work function to a similar degree witnessed during LA of the CsBr/Cu photocathode. F-centres by contrast induce a work function shift about half as large.

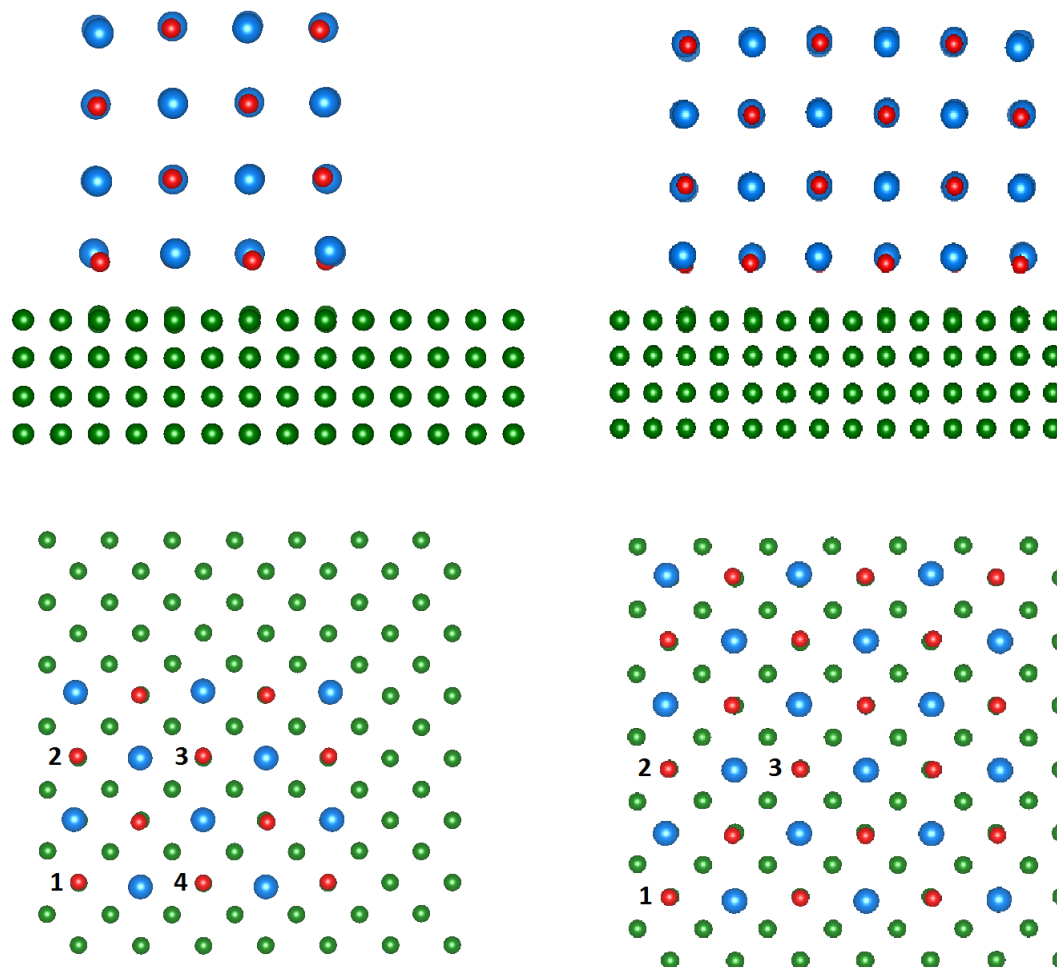


Figure 7.12: The geometry of relaxed 4ML CsBr clusters of 21% and 75% coverage on the Cu(100) surface.

7.4.3.3 F-centres in CsBr Clusters

F-centres have been modelled at various sites on 4ML CsBr clusters of 21% and 75% coverage in order to find preferential sites and gauge their effect on the work function. Figure 7.12 shows the relaxed geometry of the defect-less clusters, where the indices refer to the sites where vacancies have been modelled.

The Br ions tend to relax towards and the Cs ions away from the cluster. This effect is most pronounced at the corners, where Br ions at corner interface sites (position 1 in Figure 7.12) relax by 0.3 \AA , and Cs corner interface ions by 0.35 \AA .

The calculated formation energies of F-centres placed at the indicated sites in the clusters, and the resulting reductions of the work function with respect to bare Cu are displayed in Table 7.6.

The F-centres have a preference to form at the site of lowest coordination, i.e. at

	Coverage	Site	E_{Form}	$\Delta\phi$
CsBr/Cu(100)	21%	None	-	1.30
		1	3.38	1.43
		2	3.45	1.43
		3	3.52	1.41
		4	3.61	1.44
	75%	None	-	1.60
		1	3.38	1.68
		2	3.49	1.66
		3	3.60	1.64

Table 7.6: The formation energies (E_{Form}) of F-centres at positions at the interface, and their corresponding change in the work function ($\Delta\phi$) with respect to the bare Cu(100) surface. All energies are in eV.

corner sites, with sites in the centre of the cluster having the highest formation energies. The calculated energies are very similar for both clusters, with the difference between corner and cluster centre sites being approximately 0.2 eV. The formation energy of F-centres in the centre of the cluster is close to the calculated formation energy of F-centres at the interface layer for clusters of full coverage (3.58 eV). The change in work function as a result of the F-centres is of the order of around 0.1 - 0.15 eV, with the effect decreasing as the cluster becomes larger. Thus vacancies in films with a depleted interface will have a larger effect on the work function than in films with a clean interface, where the reduction for a single F^+ -centre has been calculated as 0.07 eV.

7.5 Discussion

The effect of perfect and rough CsBr thin films on the bulk Cu work function has been investigated as a function of coverage and film thickness. The effect of including approximations to van der Waals forces has also been examined. F-centres and divacancies have been modelled at various positions in the film, and mechanisms which will act as to reduce the work function during irradiation have been proposed which provide possible explanations of the phenomenon of photocathode LA.

Calculations predict a work function shift of around 1.5 - 1.7 eV for smooth CsBr films, which may shift further by around 0.1 eV as a result of F-centres created in the films as a by-product of irradiation. Films of partial coverage placed on Cu are predicted to shift the work function to a similar degree for film coverages over 50%.

Indeed clusters of coverage around 75% actually induce a larger work function reduction than films of full coverage. This is not inconsistent with existing models of insulating films deposited on metals. Experimentally, it has been observed that films of partial Cs coverage induce a work function reduction larger than films of 1ML thickness and above[235, 236, 237]. One study has measured maximum photoemission for Cs deposited on Au(111) at a coverage of between 0.2-0.25 ML[238]. This suggests that the deposition of ions may decrease the work function to a larger extent than bulk-like clusters or perfect films, and that the charge transfer from ion to metal can induce a larger shift than the effect due to compression of the electronic wavefunctions in the metal due to the insulating films.

The inclusion of van der Waals forces leads to a further reduction in the interfacial separation and consequently the work function of the films. The additional reduction in work function is consistent with the predicted shift for films where dispersion forces are not included. This again suggests interfacial separation is the primary factor in determining work function reduction.

CsBr films which have been used to measure the work function reduction in experiment range from thicknesses of 3 - 7 nm[54, 56]. The films have been irradiated with 266 nm lasers (4.66 eV), i.e. at energies below the bulk and surface exciton thresholds. As such, defects created in the films must be a result of two-photon processes. As the cross-section with the bulk is larger than the surface, the creation of F-H pairs and their subsequent separation should let to thermally desorbing Br atoms and largely immobile F-centres within the bulk, as proposed in Chapter 5. F-centres should remain immobile due to the large migration barrier (calculated as 1 eV in Chapter 4), unless their proximity to the interface is close enough such that an electron is transferred to the metal, whereby the F^+ -centre, which has a relatively small migration barrier (0.3 eV, see Chapter 4), should be mobile, and feel a force in the direction of the interface due to the image charge in the metal. As a result F^+ -centres should preferentially diffuse towards the interface, however the mutual repulsive Coulombic forces between the defects limits their aggregation. Calculations here at or above equilibrium density predict a maximum shift of the work function of 0.15 eV due to these defects, about half as large as the shift normally associated with LA (0.3 eV).

Calculations of F-centres in clusters, which imitate rough films, suggest they will

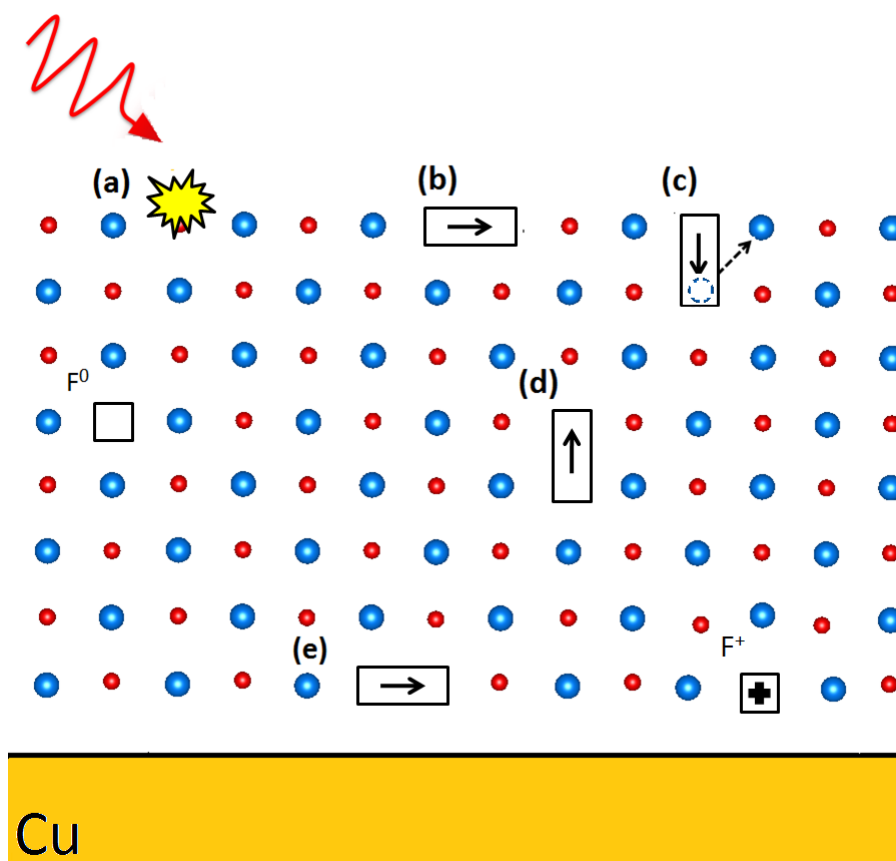


Figure 7.13: The proposed mechanism corresponding to laser activation of the photocathode.

gravitate to low-coordinated sites, with corner sites having the lowest formation energy. The reduction of the work function due to these defects is again calculated as a maximum of 0.15 eV. These calculations suggest the activation period cannot be explained simply as F-centre creation and aggregation at the interface.

As argued in Chapter 6, divacancies will be created at the surface as a result of laser irradiation. Figure 7.13 shows a schematic of divacancy creation and diffusion in CsBr thin films. Photons incident on the surface, as Fig. 7.13a), can create an exciton on the surface, which by the mechanisms outlined in Chapter 6, will lead to divacancies on the CsBr surface, as Fig. 7.13b). Although divacancy motion is inhibited by trapped electrons, the barrier to electron escape is small, (~ 0.3 eV, as calculated in Chapter 6), and in the neutral charge state some divacancies may rotate into the bulk, as in Fig. 7.13c). The barrier to divacancy motion is such that they can diffuse through the bulk at room temperature by a series of 90° rotations, according to CI-NEB calculations above. Divacancies near the interface, as Fig. 7.13d), will induce an image charge

in the metal such that there exists a driving force on the divacancy in the direction of the metal. Finally, the divacancy will move to the interface, to the most thermodynamically favourable configuration parallel to the interface, and Br-Cu bond formation involving the charge transfer of two electrons from Br ions neighbouring the Cs vacancy act to reduce the work function of Cu. The work function reduction due to a divacancy and a tetra-vacancy is calculated as 0.16 and 0.28 eV, respectively. These calculations suggest that the photo-induced creation and aggregation of Br vacancies *and* Br-Cs dimer vacancies at the interface can explain laser activation.

To summarise we have examined various features of perfect and rough CsBr films, including coverage, film thickness and interfacial separation, and analysed how these affect the reduction of the Cu work function. A mechanism has been proposed whereby defects created in the film migrate to and aggregate at the interface, which further reduces the work function of a photocathode in operation, and is responsible for observed laser activation.

Chapter 8

General Conclusions

This thesis has presented theoretical calculations of point defects in CsBr and CsBr/Cu in order to explain experimental results of desorption from insulator- and metal-grown CsBr thin films, optical absorption spectra and the changes in QE of Cu photocathodes following the deposition of CsBr thin film coatings.

Calculations of charged vacancies (F^- , F^0 - and F^+ -centres), trapped holes (V_k -centres), interstitial atoms (H- and I-centres) and the self-trapped exciton have been presented. While some of these defects have been calculated previously, using classical or DFT methods, in CsBr and other alkali halides, here state-of-the-art calculations have been conducted of all primary defects using the same model. As well as providing valuable information on the characteristics of the defects themselves, this analysis, together with experimental data, allows for an assessment of the accuracy of the underlying analytical methods. In particular, the calculations provide strong support for the practice of increasing the HF exchange with functionals such as PBE0 and B3LYP as being an effective way of obtaining an accurate band gap without impairing the functionals' quantitative predictive power.

The methodology used here also serves to provide a reliable scheme by which one can model a family of different point defects in similar wide-band gap insulating materials, such as oxides, which have numerous industrial applications, and provide a benchmark for the accuracy which can be expected from TD-DFT calculations. This allows for the production of reliable data for the optical properties of defects in the absence of experimental data.

The fact that α - and β -CsBr are energetically close has allowed for an investigation into excitons at these surface and to examine the influence of the atomic surface

structure on their electronic structure. Models of hyperthermal and thermal desorption has been extended to CsBr from the rocksalt alkali halides. Calculations of excitons at the surface successfully explained the disparity between desorption distributions from UV-irradiated CsBr/LiF and CsBr/KBr films. Furthermore, explicit calculations of relating to thermal desorption have been conducted, providing support for the proposed mechanism.

The model of hyperthermal desorption has been further extended to explain desorption results from irradiated CsBr/Cu films. The trapping of electrons photoemitted from the Cu substrate at CsBr surface defects and low-coordinated sites leads to a reduction in energy of excitons at the surface due to interaction with the electric field. A model of electron-mediated Cs desorption from CsBr films subsequent to Br desorption via an analogue of the Franck-Hertz effect has been presented. This model suggests CsBr/Cu films should be rich in divacancies at the surface, whose diffusion is inhibited by the trapping of photo-emitted electrons, leading to attenuated hyperthermal desorption energies. This is in contrast to desorption from insulator-grown films, where surface defects are expected to freely diffuse and coalesce, forming large pits, as is evident in post-experiment AFM images of alkali halides such as KBr after high energy irradiation. In addition low-coordinated sites have been modelled at the CsBr surface, with and without trapped electrons, and their electron trapping characteristics have been examined.

Finally the various factors which contribute towards a reduction in the work function of Cu after the application of CsBr films have been examined, both before and after a period of irradiation. In particular, the activation period of CsBr/Cu photocathodes has been explained as resulting from a minority of divacancies created at the surface rotating and diffusing into the bulk, diffusing towards the metal due to attraction between the dipole and the induced image charge, and their subsequent segregation at the CsBr/Cu interface.

In order to extend the work on desorption from CsBr/Cu films Monte Carlo simulations of the evolving surface would be of interest. The migration barriers to defect motion have largely been calculated here. Calculations of the barriers to diffusion on CsBr surfaces for defects such as F-centres and divacancies, as well as the barriers towards diffusion into the bulk would provide a full set of barriers from which one could

begin to construct Monte Carlo stochastic probabilities. This extension from the atomic scale to a slightly larger nanoscopic scale would allow for a greater understanding of the evolution of irradiated films by giving an understanding of the relative proportions of defects which coalesce or remain isolated on the surfaces, and the defects which diffuse through the bulk and segregate at the interface. In particular it would be enlightening to gain greater understanding of the simultaneous evolution at the surface and at the interface.

Excitons created at the interface by incident photons could also be modifying the atomic structure at the interface. In order to accurately model these excitons, a hybrid functional description would be required. As calculations with hybrid functionals are expensive, and a large number of atoms was required to model CsBr/Cu films in this thesis, a major challenge would be how to make such calculations tractable.

In addition, interfacing GUESS with Gaussian09, which includes TD-DFT with forces, opens up the possibilities of looking at the excited potential energy surfaces of defects such as the F-centre, and examine phenomena such as F-centre luminescence, at the surface and in the bulk. Calculations comparing singlet and triplet excitons would also be of general interest.

The results in this thesis increase our understanding of the functioning and degradation of CsBr/Cu photocathodes. Moreover the understanding of how lasers in the UV range interact with insulating films grown on metal and insulator substrates contribute to the general scientific understanding of these systems, and help predict combinations of these materials with desirable characteristics.

Bibliography

- [1] T. Suzuki and R. Souda. Structure analysis of CsCl deposited on the MgO(001) surface by coaxial impact collision atom scattering spectroscopy (CAICASS). *Surf. Sci.*, 442:283, 1999.
- [2] M Kiguchi, S. Entani, K. Saiki, and A. Koma. Atomic and electronic structure of CsBr film grown on LiF and KBr(001). *Surf. Sci.*, 523:73, 2003.
- [3] B. V. R. Chowdari and N. Itoh. Interstitial halogen centers in X-irradiated CsBr. *J. Phys. Chem. Solids*, 33:1773, 1971.
- [4] R. Bennewitz, S. Schaer, V. Barwich, O. Pfeiffer, E. Meyer, F. Krok, B. Such, J. Kolodziej, and M. Szymonksi. Atomic-resolution images of radiation damage in KBr. *Surf. Sci.*, 474:L197, 2001.
- [5] W. He, S. Vilayurganapathy, A. G. Joly, T. C. Droubay, S. A. Chambers, J. R. Maldonado, and W. P. Hess. Comparison of CsBr and KBr covered Cu photocathodes: Effects of laser irradiation and work function changes. *App. Phys. Lett.*, 102:071604, 2013.
- [6] S. Huefner, G. K. Wertheim, N. V. Smith, and M. M. Traum. XPS density of states of copper, silver, and nickel. *Sol. Stat. Comms.*, 11:323, 1972.
- [7] U. Bach, D. Lupo, P. Comte, J. E. Moser, F. Wiesoertel, J. Salbeck, H. Spreitzer, and M. Graetzel. Solid-state dye-sensitized mesoporous TiO₂ solar cells with high photon-to-electron conversion efficiencies. *Nature*, 395:583, 1998.
- [8] J. T. M. d. Haas and P. Dorenbos. Advances in yield calibration of scintillators. *IEEE Trans. Nucl. Sci.*, 55:1086, 2008.
- [9] C. W. E. van Eijk. Inorganic scintillators in medical imaging. *Phys. Med. Biol.*, 47:R85, 2002.

- [10] A. Einstein. Ueber einen der Erzeugung und Verwandlung des Lichtes betreffenden heuristischen Gesichtspunkt. *Annal. Phys.*, 17:132, 1905.
- [11] E. D. Bloom, D. H. Coward, H. DeStaebler, J. Drees, G. Miller, L. W. Mo, R. E. Taylor, M. Breidenbach, J. I. Friedman, G. C. Hartmann, and H. W. Kendall. High-energy inelastic $e - p$ scattering at 6° and 10° . *Phys. Rev. Lett.*, 23:930, 1969.
- [12] M. Breidenbach, J. I. Friedman, H. W. Kendall, E. D. Bloom, D. H. Coward, H. DeStaebler, J. Drees, L. W. Mo, and R. E. Taylor. Observed behavior of highly inelastic electron-proton scattering. *Phys. Rev. Lett.*, 23:935, 1969.
- [13] M. L. Perl, G. S. Abrams, A. M. Boyarski, M. Breidenbach, D. D. Briggs, F. Bulos, W. Chinowsky, J. T. Dakin, G. J. Feldman, C. E. Friedberg, D. Fryberger, G. Goldhaber, G. Hanson, F. B. Heile, B. Jean-Marie, and et al. Evidence for anomalous lepton production in e^+e^- annihilation. *Phys. Rev. Lett.*, 35:1489, 1975.
- [14] J. E. Augustin, A. M. Boyarski, M. Breidenbach, F. Bulos, J. T. Dakin, G. J. Feldman, G. E. Fischer, D. Fryberger, G. Hanson, B. Jean-Marie, R. R. Larsen, V. Lüth, H. L. Lynch, D. Lyon, C. C. Morehouse, J. M. Paterson, M. L. Perl, B. Richter, P. Rapidis, R. F. Schwitters, W. M. Tanenbaum, F. Vannucci, G. S. Abrams, D. Briggs, W. Chinowsky, C. E. Friedberg, G. Goldhaber, R. J. Hollebeek, J. A. Kadyk, B. Lulu, F. Pierre, G. H. Trilling, J. S. Whitaker, J. Wiss, and J. E. Zipse. Discovery of a narrow resonance in e^+e^- annihilation. *Phys. Rev. Lett.*, 33:1406, 1974.
- [15] T. R. M. Barends, L. Foucar, S. Botha, R. B. Doak, R. L. Shoeman, K. Ness, J. E. Koglin, G. J. Williams, S. Boutet, M. Messerschmidt, and I. Schlichting. De novo protein crystal structure determination from X-ray free-electron laser data. *Nature*, 505:244, 2014.
- [16] H. S. Pratisto, S. R. Uhlhorn, M. Copeland, and E. Duco Jansen. Clinical beam delivery of the Vanderbilt FEL: design and performance of a hollow-waveguide-based handheld probe for neurosurgery. In *Proc. SPIE 3595, Specialty fiber optics for medical applications*, volume 55, 1999.

- [17] S. M. Aldoshin, A. I. Zenchuk, B. Feldman, and M. A. Yurishchev. On the way to creation of materials for quantum computers. *Russ. Chem. Rev.*, 81:91, 2012.
- [18] J. D. Bozek. AMO instrumentation for the LCLS X-ray FEL. *Eur. Phys. J. Spec. Topics*, 169:129, 2009.
- [19] Y. Seimiya, M. Kuriki, A. Yokota, R. Kaku, T. Konomi, M. Yamamoto, and T. Miyajima. CsKSb photocathode R and D with high quantum efficiency and long lifetime. In *Proceedings of IPAC2015, VA, USA*.
- [20] I. V. Bazarov, B. M. Dunham, Y. Li, X. Liu, D. G. Ouzounov, C. K. Sinclair, F. Hannon, and T. Miyajima. Thermal emittance and response time measurements of negative electron affinity photocathodes. *J. Appl. Phys.*, 103:054901, 2008.
- [21] X. Guo, X. Wang, B. Chang, Y. Zhang, and P. Gao. High quantum efficiency of depth grade doping negative-electron-affinity GaN photocathode. *Appl. Phys. Lett.*, 97:063104, 2010.
- [22] F. Machuca, Z. Liu, Y. Sun, R. Pianetta, W. E. Spicer, and R. F. W. Pease. Oxygen species in Cs/O activated GaN negative electron affinity photocathodes. *J. Vac. Sci. Technol. B*, 21:1863, 2003.
- [23] O. Siegmund, J. Vallerger, J. McPhate, J. Malloy, A. Tremsin, A. Martin, M. Ulmer, and B. Wessels. Development of GaN photocathodes for UV detectors. *Nucl. Instr. and Meth. in Phys. Res. A*, 567:89, 2006.
- [24] L. E. Bourree, D. R. Chasse, P. L. S. Thamban, and R. Glosser. MBE-grown InGaAs photocathodes. *Proc. SPIE*, 4796:1, 2003.
- [25] Y. Sun, R. E. Kirby, T. Maruyama, G. A. Mulhollan, J. C. Bierman, and P. Pianetta. The surface activation layer of GaAs negative electron affinity photocathode activated by Cs, Li and NF_3 . *Appl. Phys. Lett.*, 95:174109, 2009.
- [26] Y. Zhang, J. Niu, J. Zhao, J. Zou, B. Chang, F. Shi, and H. Chang. Influence of exponential-doping structure on photoemission capability of transmission-mode GaAs photocathodes. *J. Appl. Phys.*, 108:093108, 2010.

- [27] N. Yamamoto, M. Yamamoto, M. Kuwahara, R. Sakai, T. Morino, K. Tamagaki, A. Mano, A. Utsu, S. Okumi, T. Nakanishi, M. Kuriki, C. Bo, T. Ujihara, and Y. Takeda. Thermal emittance measurements for electron beams produced from bulk and superlattice negative electron affinity photocathodes. *J. Appl. Phys.*, 102:024904, 2007.
- [28] O. H. W. Siegmund. High-performance microchannel plate detectors for UV/visible astronomy. *Nucl. Instr. and Meth. in Phys. Res. A*, 525:12, 2004.
- [29] V. V. Bakin, K. V. Toropetsky, H. E. Scheibler, A. S. Terekhov, L. B. Jones, B. L. Militsyn, and T. C. Q. Noakes. p-GaAs(Cs,O)-photocathodes: Demarcation of domains of validity for practical models of the activation layer. *Appl. Phys. Lett.*, 106:183501, 2015.
- [30] S. H. Kong, J. Kinross-Wright, D. C. Nguyen, R. L. Sheffield, and M. E. Weber. Performance of cesium telluride photocathodes as an electron source for the Los Alamos advanced FEL. *Nucl. Instr. and Meth. in Phys. Res. A*, 358:284, 1995.
- [31] S. H. Kong, J. Kinross-Wright, D. C. Nguyen, and R. L. Sheffield. Cesium telluride photocathodes. *J. Appl. Phys.*, 77:6031, 1995.
- [32] D. Sertore, S. Schreiber, K. Floettmann, F. Stephan, K. Zapfe, and P. Michelato. First operation of cesium telluride photocathodes in the TTF injector RF gun. *Nucl. Instr. and Meth. in Phys. Res. A*, 445:422, 2000.
- [33] D. Bisero, B. M. van Oerle, G. J. Ernst, J. W. J. Verschuur, and W. J. Witteman. High efficiency photoemission from Cs-K-Te. *Appl. Phys. Lett.*, 70:1491, 1997.
- [34] E. Shefer, A. Breskin, R. Chechik, A. Buzulutskov, B. K. Singh, and M. Prager. Coated photocathodes for visible photon imaging with gaseous photomultipliers. *Nucl. Instr. and Meth. in Phys. Res. A*, 433:502, 1999.
- [35] A. Lyanshenko, A. Breskin, R. Chechik, and T. H. V. T. Dias. Ion-induced secondary electron emission from K-Cs-Sb, Na-K-Sb and Cs-Sb photocathodes and its relevance to the operation of gaseous avalanche photomultipliers. *J. Appl. Phys.*, 106:044902, 2009.

- [36] H. Jeong, K. Keller, and B. Culklin. Electron emission properties of Cs₃Sb photocathode emitters in a panel device. *J. Vac. Sci. Technol. B*, 33:031214, 2015.
- [37] A. H. Sommer. Bialkali (K₂ CsSb) photocathode as a high-gain secondary electron emitter. *J. Appl. Phys.*, 43:2479, 1972.
- [38] S. Kasap. *Principles of electronic materials and devices, second edition*. McGraw-Hill, 2002.
- [39] A. Villegas, Y. Kudriavtsev, A. Godines, and R. Asomoza. Work function change caused by alkali ion sputtering. *Appl. Surf. Sci.*, 203:94, 2003.
- [40] N. D. Lang. Theory of work function changes induced by alkali adsorption. *Phys. Rev. B*, 4:4234, 1971.
- [41] A. H. Sommer. *Photoemissive materials*. Krager, Huntington, 1980.
- [42] A. Breskin, A. Buzulutskov, R. Chechik, R. Prager, and E. Shefer. Evidence for thin-film protection of visible photocathodes. *Appl. Phys. Lett.*, 69:1008, 1996.
- [43] A. Buzulutskov, A. Breskin, R. Chechik, M. Prager, and E. Shefer. Protection of cesium-antimony photocathodes. *Nucl. Instr. and Meth. in Phys. Res. A*, 387:176, 1997.
- [44] A. Buzulutskov, A. Breskin, and R. Chechik. Photoemission through thin dielectric coating films. *J. Appl. Phys.*, 81:466, 1997.
- [45] E. Shefer, A. Breskin, A. Buzulutskov, R. Chechik, and M. Prager. Composite photocathodes for visible photon imaging with gaseous photomultipliers. *Nucl. Instr. and Meth. in Phys. Res. A*, 419:612, 1998.
- [46] A. Buzulutskov, E. Shefer, A. Breskin, R. Chechik, and M. Prager. The protection of K-Cs-Sb photocathodes with CsBr films. *Nuc. Inst. Meth. in Phys. Res. A*, 400:173, 1997.
- [47] T. Boutboul, A. Breskin, R. Chechik, E. Klein, A. Braem, G. Lion, and P. Mine. On the surface morphology of thin alkali halide photocathode films. *Nucl. Instr. Meth. in Phys. Res. A*, 438:409, 1999.

- [48] Z. Liu, J. Maldonado, Y. Sun, P. Pianetta, and R. F. W. Pease. CsBr photocathode at 257 nm: A rugged high current density electron source. *Appl. Phys. Lett.*, 89:111114, 2006.
- [49] J. R. Maldonado, Z. Liu, Y. Sun, P. Pianetta, and F. W. Pease. Photoelectron emission studies in CsBr at 257 nm. *J. Vac. Sci. Tech. B*, 24:2886, 2006.
- [50] J. Maldonado, Y. Sun, Y. Liu, X. Liu, S. Tanimoto, P. Pianetta, and F. Pease. Evaluation of electron energy spread in CsBr based photocathodes. *J. Vac. Sci. and Tech.*, 26:2085, 2008.
- [51] J. R. Maldonado, P. Pianetta, D. H. Dowell, J. Smedley, and P. Kneisel. Performance of a CsBr coated Nb photocathode at room temperature. *J. Appl. Phys.*, 107:013106, 2010.
- [52] J. Maldonado, Z. Liu, R. Kirby, Y. Sun, P. Pianetta, and F. Pease. Robust CsBr/Cu photocathodes for the linac coherent light source. *Phys. Rev. Spec. Topics - Acc. and Beams*, 11:060702, 2008.
- [53] J. R. Maldonado, Z. Liu, D. H. Dowell, R. E. Kirby, Y. Sun, P. Pianetta, and F. Pease. Electron sources utilizing thin CsBr coatings. *Microelec. Eng.*, 86:529, 2009.
- [54] W. He, S. Vilayurganapathy, T. C. Droubay, S. A. Chambers, W. P. Hess, and J. R. Maldonado. Comparison of KBr coated Cu photocathodes: Laser irradiation and work function changes. *J. Appl. Phys. Lett.*, 102:071604, 2013.
- [55] J. R. Maldonado, P. Pianetta, D. H. Dowell, J. Corbett, S. Park, J. Schmerge, A. Trautwein, and W. Clay. Experimental verification of the 3-step model of photoemission for energy spread and emittance measurements of copper and CsBr-coated copper photocathodes suitable for free electron laser applications. *Appl. Phys. Lett.*, 101:231103, 2012.
- [56] L. Kong, A. G. Joly, T. C. Droubay, Y. Gong, and W. P. Hess. Enhanced quantum efficiency from hybrid cesium halide/copper photocathodes. *Appl. Phys. Lett.*, 104:171106, 2014.

- [57] B. K. Singh, E. Shefer, A. Breskin, R. Chechik, and N. Avraham. CsBr and CsI UV photocathodes: new results on quantum efficiency and aging. *Nuc. Inst. Meth. in Phys. Res. A*, 454:364, 2000.
- [58] T. Vecchione, J. R. Maldonado, S. Gierman, J. Corbett, N. Hartmann, P. A. Pianetta, L. Hesselink, and J. F. Schmerge. High gradient rf gun studies of CsBr photocathodes. *Phys. Rev. ST Accel. Beams*, 18:040701, 2015.
- [59] M. Born and R. Oppenheimer. Zur Quantentheorie der Molekeln. *Annal. Phys.*, 389:457, 1927.
- [60] A. Szabo and N. S. Ostlund. *Modern quantum chemistry: Introduction to advanced electronic structure theory*. Dover publications, 1996.
- [61] J. C. Slater. A simplification of the Hartree-Fock method. *Phys. Rev.*, 81:385, 1951.
- [62] W. Ritz. Ueber eine neue methode zur loesung gewisser variationsprobleme der mathematischen physik. *J. Fuer Rein. und Angew. Math.*, 135:1, 1909.
- [63] P. Hohenberg and W. Kohn. Inhomogenous electron gas. *Phys. Rev.*, 136:B864, 1964.
- [64] M. Head-Gordon, J. A. Pople, and M. J. Frisch. MP2 energy evaluation by direct methods. *Chem. Phys. Lett.*, 153:503, 1988.
- [65] E. H. Lieb and B. Simon. The Thomas-Fermi theory of atoms, molecules and solids. *Adv. in Math.*, 23:22, 1977.
- [66] W. Kohn and L. J. Sham. Self consistent equations including exchange and correlation effects. *Phys. Rev.*, 140:A1133, 1965.
- [67] D. M. Ceperley and B. J. Alder. Ground state of the electron gas by a stochastic method. *Phys. Rev. Lett.*, 45:566, 1980.
- [68] S. H. Vosko, L. Wilk, and M. Nusair. Accurate spin-dependent electron liquid correlation energies for local spin density calculations: a critical analysis. *Can. J. Phys.*, 58:1200, 1980.

- [69] S. Kurth, J. P. Perdew, and P. Blaha. Molecular and solid-state tests of density functional approximations: LSD, GGAs, and meta-GGAs. *Int. J. Quan. Chem.*, 75:889, 1999.
- [70] J. P. Perdew and M. Levy. Physical content of the exact Kohn-Sham orbital energies: Band gaps and derivative discontinuities. *Phys. Rev. Lett.*, 51:1884, 1983.
- [71] D. Becke. Density-functional thermochemistry. III. the role of exact exchange. *J. Chem. Phys.*, 98:5648, 1993.
- [72] J. P. Perdew and Y. Wang. Accurate and simple analytic representation of the electron-gas correlation energy. *Phys. Rev. B*, 45:13244, 1992.
- [73] J. P. Perdew, K. Burke, and M. Ernzerhof. Generalised gradient approximation made simple. *Phys. Rev. Lett.*, 77:3865, 1996.
- [74] A.D. Becke. Density-functional exchange-energy approximation with correct asymptotic behavior. *Phys. Rev. A*, 38:3098, 1988.
- [75] C. Lee, W. Yang, and R. Parr. Development of the Colle-Salvetti correlation-energy formula into a functional of the electron density. *Phys. Rev. B*, 37:785, 1988.
- [76] A. D. Becke. A new mixing of Hartree-Fock and local density-functional theories. *J. Chem. Phys.*, 98:1372, 1993.
- [77] M. Ernzerhof and G. E. Scuseria. Assessment of the Perdew Burke Ernzerhof exchange-correlation functional. *J. Chem. Phys.*, 110:5029, 1999.
- [78] C. Adamo and V. Barone. Toward reliable density functional methods without adjustable parameters: The PBE0 model. *J. Chem. Phys.*, 110:6158, 1999.
- [79] C. Adamo and V. Barone. Exchange functionals with improved long-range behavior and adiabatic connection methods without adjustable parameters: The mPW and mPW1PW models. *J. Chem. Phys.*, 108:664, 1998.

- [80] M. Guidon, J. Hutter, and J. VandeVondele. Auxiliary density matrix methods for Hartree-Fock exchange calculations. *J. Chem. Theory and Comp.*, 6:2348, 2010.
- [81] S. Ling, M. B. Watkins, and A. L. Shluger. Effects of atomic scale roughness at metal/insulator interfaces on metal work function. *Phys. Chem. Chem. Phys.*, 15:19615, 2013.
- [82] S. Ling, M. B. Watkins, and A. L. Shluger. Effects of oxide roughness at metal oxide interface: MgO on Ag(001). *J. Phys. Chem. C*, 117:5075, 2013.
- [83] E. Runge and E. K. U. Gross. Density-functional theory for time-dependent systems. *Phys. Rev. Lett.*, 52:997, 1984.
- [84] R. Bauernschmitt and R. Ahlrichs. Treatment of electronic excitations within the adiabatic approximation of time dependent density functional theory. *Chem. Phys. Lett.*, 256:454, 1996.
- [85] M. E. Casida. Time-dependent density-functional theory for molecules and molecular solids. *J. Molec. Struct.*, 914:3, 2009.
- [86] S. Hirata and M. Head-Gordon. Time-dependent density functional theory within the Tamm-Dancoff approximation. *Chem. Phys. Lett.*, 314:291, 1999.
- [87] J. F. Dobson and T. Gould. Calculations of dispersion energies. *J. Phys. Condens. Matt.*, 24:073201, 2012.
- [88] T. Bjorkman, A. Gulans, A. V. Krasheninnikov, and R. M. Nieminen. Are we van der Waals ready? *J. Phys.: Condens. Matt.*, 24:424218, 2012.
- [89] J. Klimes and A. Michaelides. Perspective: Advances and challenges in treating van der Waals dispersion forces in density functional theory. *J. Chem. Phys.*, 137:120901, 2012.
- [90] S. Grimme. Semiempirical GGA-type density functional constructed with a long-range dispersion correction. *J. Comput. Chem.*, 27:1787, 2006.

- [91] H. J. Monkhorst and J. D. Pack. Special points for brillouin-zone integrations. *Phys. Rev. B*, 13:5188, 1976.
- [92] Relative energies of surface and defect states: ab initio calculations for the MgO (001) surface. *Surf. Sci.*, 450:153, 2000.
- [93] P. V. Sushko and I. V. Abarenkov. General purpose electrostatic embedding potential. *J. Chem. Theory and Comp.*, 6:1323, 2010.
- [94] R. A. Buckingham. The classical equation of state of gaseous Helium, Neon and Argon. *Proc. Royal. Soc. A*, 168:264, 1938.
- [95] R. Dovesi, V. Saunders, C. Roetti, C. Zicovich-Wilson, F. Pascale, B. Civalleri, K. Doll, Harrison N., I. Bush, P. D'Arco, and M. Llunell. *CRYSTAL09*. University of Torino, 2009.
- [96] J. Hutter, M. Iannuzzi, F. Schiffmann, and J. VandeVondele. CP2K: atomistic simulations of condensed matter systems. *Wiley Int. Rev: Comp. Mol. Sci.*, 4:15, 2014.
- [97] M. Towler, I. Bush, and N. Harrison. <http://www.tcm.phy.cam.ac.uk/mdt26/crystal.html>.
- [98] P. Haas, F. Tran, and P. Blaha. Calculation of the lattice constant of solids with semilocal functionals. *Phys. Rev. B*, 79:085104, 2009.
- [99] J. Paier, M. Marsman, and G. Kresse. Why does the B3LYP hybrid functional fail for metals? *J. Chem. Phys.*, 127:024103, 2007.
- [100] T. Bredow and A. R. Gerson. Effect of exchange and correlation on bulk properties of MgO, NiO, and CoO. *Phys. Rev. B*, 61:5194, 2000.
- [101] F. Birch. Finite elastic strain of cubic crystals. *Phys. Rev.*, 71:809, 1947.
- [102] J. L. Tallon. The thermodynamics of elastic deformation - I. Equation of state for solids. *J. Phys. Chem. Solids*, 41:837, 1980.
- [103] P. Vinet, J. H. Rose, J. Ferrante, and J. R. Smith. Universal features of the equation of state of solids. *J. Phys.: Condens. Matt.*, 1:1941, 1989.

- [104] Z. P. Chang, G. R. Barsch, and D. L. Miller. Pressure dependence of elastic constants of cesium halides. *Phys. Stat. Sol. (b)*, 23:577, 1967.
- [105] C. W. F. T. Pistorius. Phase relations and structures of solids at high pressures. *Prog. in Sol. Stat. Chem.*, 11, Part 1, 1976.
- [106] R. P. Singh, G. G. Agrawal, and J. Shanker. Evaluation of the van der Waals dipole-dipole potential in CsCl, CsBr and CsI crystals. *Sol. Stat. Comms.*, 25:173, 1978.
- [107] N.C. Pyper. The relative stability of the six- and eight-fold co-ordinated structures of cesium chloride. *Chem. Phys. Lett.*, 220:70, 1994.
- [108] F. Zhang, J. D. Gale, B. P. Uberuaga, C. R. Stanek, and N. A. Marks. Importance of dispersion in density functional calculations of cesium chloride and its related halides. *Phys. Rev. B*, 88:054112, 2013.
- [109] A. A. Gavini and M. Cardona. Reflectivity spectra of CsBr and CsI in the rock-salt structure. *Phys. Lett.*, 27A:112, 1968.
- [110] S. Satpathy. Electron energy bands and cohesive properties of CsCl, CsBr, and CsI. *Phys. Rev. B*, 33:8706, 1985.
- [111] A. M. Stoneham. *Theory of Defects in Solids - Electronic structure of defects in insulators and semiconductors*. Oxford University Press, 1975.
- [112] F. C. Brown, B. C. Cavenett, and W. Hayes. Magneto-optical properties of defect centres in alkali halide crystals. *Proc. Roy. Soc. A*, 300:78, 1967.
- [113] T. Pawlik, V. Dierolf, and J-M. Spaeth. An electron-nuclear double-resonance study of the F centre in CsBr. *J. Phys.: Condens. Matter*, 9:1857, 1997.
- [114] R. K. Dawson and D. Pooley. F band absorption in alkali halides as a function of temperature. *phys. stat. sol. (b)*, 35:95, 1969.
- [115] E. Vasil'chenko, N. Luschik, and C. Luschik. Migrations of excitons and holes in luminescent crystals of CsBr. *J. Lumin.*, 5:117, 1971.

- [116] M. Itoh, K. Tanimura, and N. Itoh. Optical studies of self-trapped excitons in CsCl and CsBr. *J. Phys. Soc. Japan*, 62:2904, 1993.
- [117] M. J. Marrone, F. W. Patten, and M. N. Kabler. EPR in triplet states of the self-trapped exciton. *Phys. Rev. Lett.*, 31:467, 1973.
- [118] J. Zimmermann, S. Hesse, H. von Seggern, M. Fuchs, and W. Knuepfer. Radiation hardness of CsBr:Eu²⁺. *J. Lumin.*, 114:24, 2005.
- [119] J. Carrasco, N. Lopez, C. Sousa, and F. Illas. First-principles study of the optical transitions of F centers in the bulk and on the (0001) surface of α -Al₂O₃. *Phys. Rev. B*, 72:054109, 2005.
- [120] K. Raghavachari, D. Ricci, and G. Pacchioni. Optical properties of point defects in SiO₂ from time-dependent density functional theory. *J. Chem. Phys.*, 116:825, 2002.
- [121] J. Carrasco, C. Sousa, F. Illas, P. V. Sushko, and A. L. Shluger. Optical absorption and luminescence energies of F centers in CaO from ab initio embedded cluster calculations. *J. Chem. Phys.*, 125:074710, 2006.
- [122] V. B. Sulimov, P. V. Sushko, A.H. Edwards, A. L. Shluger, and A. M. Stoneham. Assymetry and long-range character of lattice deformation by neutral oxygen vacancy in α -quartz. *Phys. Rev. B*, 66:024108, 2002.
- [123] S. Mukhopadhyay, P. V. Sushko, A. M. Stoneham, and A. L. Shluger. Modeling of the structure and properties of oxygen vacancies in amorphous silica. *Phys. Rev. B*, 70:195203, 2004.
- [124] M. J. Frisch, G. W. Trucks, H. B. Schlegel, G. E. Scuseria, M. A. Robb, J. R. Cheeseman, G. Scalmani, V. Barone, B. Mennucci, G. A. Petersson, H. Nakatsuji, M. Caricato, X. Li, H. P. Hratchian, A. F. Izmaylov, J. Bloino, G. Zheng, J. L. Sonnenberg, M. Hada, M. Ehara, K. Toyota, R. Fukuda, J. Hasegawa, M. Ishida, T. Nakajima, Y. Honda, O. Kitao, H. Nakai, T. Vreven, J. A. Montgomery, Jr., J. E. Peralta, F. Ogliaro, M. Bearpark, J. J. Heyd, E. Brothers, K. N. Kudin, V. N. Staroverov, R. Kobayashi, J. Normand, K. Raghavachari, A. Rendell, J. C. Burant, S. S. Iyengar, J. Tomasi, M. Cossi, N. Rega, J. M. Millam,

- M. Klene, J. E. Knox, J. B. Cross, V. Bakken, C. Adamo, J. Jaramillo, R. Gomperts, R. E. Stratmann, O. Yazyev, A. J. Austin, R. Cammi, C. Pomelli, J. W. Ochterski, R. L. Martin, K. Morokuma, V. G. Zakrzewski, G. A. Voth, P. Salvador, J. J. Dannenberg, S. Dapprich, A. D. Daniels, . Farkas, J. B. Foresman, J. V. Ortiz, J. Cioslowski, and D. J. Fox. Gaussian09 Revision D.01. Gaussian Inc. Wallingford CT 2009.
- [125] W. P. Hess, A. G. Joly, D. P. Gerrity, K. M. Beck, P. V. Sushko, and A. L. Shluger. Selective laser desorption of ionic surfaces: resonant surface excitation of KBr. *J. Chem. Phys.*, 115:9463, 2001.
- [126] P. V. Sushko, J. L. Gavartin, and A. L. Shluger. Electronic properties of structural defects at the MgO(001) surface. *J. Phys. Chem. B*, 106:2269, 2002.
- [127] P. V. Sushko and I. V. Abarenkov. General purpose electrostatic embedding potential. *J. Chem. Theory Comput.*, 6:1323, 2009.
- [128] L. V. Szentpaly, P. Fuentealba, H. Preuss, and H. Stoll. Pseudopotential calculations on Rb^{+2} , Cs^{+2} , RbH^+ , CsH^+ and the mixed alkali dimer ions. *Chem. Phys. Lett.*, 93:555, 1982.
- [129] J. Gavartin, P. Sushko, and A. Shluger. Modeling charge self-trapping in wide-gap dielectrics: Localization problem in local density functionals. *Phys. Rev. B*, 67:035108, 2003.
- [130] A. Kimmel, P. Sushko, and A.L. Shluger. Structure and properties of trapped holes in silica. *J. Non-Cryst. Solids*, 353:599, 2009.
- [131] G. Pacchioni, F. Frigoli, D. Ricci, and J. A. Weil. Theoretical description of hole localization in a quartz Al center: The importance of exact exchange. *Phys. Rev. B*, 63:054102, 2000.
- [132] H. Stoll, B. Metz, and M. Dolg. Relativistic energy-consistent pseudopotentials - recent developments. *J. Comput. Chem.*, 23:767, 2002.

- [133] V. Ganesan and K. Girirajan. Lattice parameter and thermal expansion coefficient of CsCl and CsBr by X-ray powder diffraction. II. Thermal expansion of CsBr from room temperature to 78.2 K. *Pramana*, 27:475, 1986.
- [134] M. Lipp, C. Yoo, D. Strachan, and W. Daniels. Band structure parameters and Fermi resonances of exciton-polarons in CsI and CsBr under hydrostatic pressure. *Phys. Rev. B*, 73:085121, 2005.
- [135] M. J. L. Sangster, U. Schroeder, and R. M. Atwood. Interionic potentials for alkali halides. *J. Phys. C: Solid State Phys.*, 11:1523, 1977.
- [136] A. E. Reed, R. B. Weinstock, and F. Weinhold. Natural population analysis. *J. Chem. Phys.*, 83:735–746, 1985.
- [137] N. Zema, M. Piacentini, P. Czuba, J. Kolodziej, P. Piatkowski, Z. Postawa, and M. Szymonski. Spectroscopic behavior of halogen photodesorption from alkali halides under UV and VUV excitation. *Phys. Rev. B*, 55:5448, 1997.
- [138] J. J. Pilloud and C. Jaccard. Dynamic properties of [X-2] centres in cesium halides. *Phys. Stat. Sol.*, 10:233, 1979.
- [139] B.V.R. Chowdari, M. Ikeya, and N. Itoh. Optical absorption spectra of the H center in CsBr. *Sol. Stat. Comms.*, 9:689, 1971.
- [140] K. S. Song and R. T. Williams. *Self-trapped Excitons*. Springer Series in Solid State Physics. Springer, 1993.
- [141] P. Reineker. Equations of motion for the moments of the coupled coherent and incoherent motion of triplet and singlet excitons. *Zeit. für Phys.*, 261:187, 1973.
- [142] W. P. Hess, A. G. Joly, K. M. Beck, P. V. Sushko, and A. L. Shluger. Determination of surface exciton energies by velocity resolved atomic desorption. *Surf. Sci.*, 564:62, 2004.
- [143] W. Hess, A. Joly, K. Beck, M. Henyk, P. Sushko, P. Trevisanutto, and A. Shluger. Laser control of desorption through selective surface excitation. *J. Phys. Chem. B*, 109:19563, 2005.

- [144] F. Seitz. Color centres in alkali halide crystals. *Rev. of Mod. Phys.*, 26:7, 1954.
- [145] T. Iida and R. Monnier. The V_k center in cesium halides. *J. Phys. Coll.*, 37:C7, 1976.
- [146] T. Sidler, J. P. Pellaux, Nouailhat. M., and M. A. Aegerter. Study of V_k centres in CsI crystal. *Sol. Stat. Comms.*, 13:479, 1973.
- [147] R. Monnier, K. Song, and A. Stoneham. The self-trapped hole caesium halides. *J. Phys. C*, 10:4441, 1977.
- [148] R. A. Johnson and A. N. Orlov, editors. *Physics of Radiation effects in crystals*. North-Holland, 1986.
- [149] Z. Postawa, J. Kolodziej, G. Baran, P. Czuba, P. Piatkowski, M. Szymonksi, I. Plavina, and A. Popov. ESD of nonthermal halogen atoms from In-doped (001) KBr. *Nucl. Inst. Meth. in Phys. Res. B*, 100:228, 1995.
- [150] M. Saidoh and Itoh. N. Ionic size effect on the radiation-induced dynamic motion of interstitial halogen in alkali halides. *Phys. Stat. Sol. (b)*, 72:709, 1975.
- [151] N. Itoh, B. S. H. Royce, and R. Smoluchowski. Recombination of vacancies and interstitials in KBr at low temperatures. *Phys. Rev.*, 137:A1010, 1965.
- [152] H. Rabin and J. Schulman. Color centers in CsCl-type alkali halides. *Phys. Rev.*, 125:1584, 1962.
- [153] F. Van de Wiele and G. Jacobs. Color centers in CsBr single crystals irradiated at liquid-helium temperature. *Phys. Rev.*, 139:A924, 1965.
- [154] H. Rabin and J. Schulman. Color centers in CsCl-type alkali halides. *Phys. Rev.*, 125:1584, 1961.
- [155] F. Van De Wiele and G. Jacobs. Optical and thermal properties of color centres in CsBr single-crystals irradiated at liquid helium temperature. *Phys. Stat. Sol.*, 12:177, 1966.
- [156] R. S. Knox. Excited states of cesium halides. *Phys. Rev.*, 133:A498, 1964.

- [157] K. S. Song and C. Fu. Relaxation of excitons in ionic halides: a molecular dynamics study. *J. Phys.: Condens. Matt.*, 13:2355, 2000.
- [158] A. L. Shluger, V. E. Puchin, T. Suzuki, K. Tanimura, and N. Itoh. Optical transitions of the H centers in alkali halides. *Phys. Rev. B*, 52:4017, 1995.
- [159] L. G. Grigorjeva, E. A. Kotomin, D. K. Millers, and R. I. Eglitis. The decay kinetics of excitonic luminescence in AgCl crystals. *J. Phys.: Condens. Matt.*, 7:1483, 1995.
- [160] A. L. Shluger, N. Itoh, V. E. Puchin, and E. N. Heifets. Two types of self-trapped excitons in alkali halide crystals. *Phys. Rev. B*, 44:1499, 1991.
- [161] A. L. Shluger, V. E. Puchin, T. Suzuki, K. Tanimura, and N. Itoh. Optical transitions of the H centers in alkali halides. *Phys. Rev. B*, 52:4017, 1995.
- [162] P. Schrey, R. Balzer, and H. Peisl. Release of stored energy of X-irradiated KCl and CsBr. *Phys. Stat. Sol. (b)*, 85:553, 1978.
- [163] J. D. Comins. Production of vacancies and other defects in KBr at low temperatures. *Phys. Stat. Sol.*, 33:445, 1964.
- [164] P. Schrey, R. Balzer, and H. Peisl. Measurement of stored energy of KBr after X-irradiation at low temperature. 1977.
- [165] A. Luschik, E. Feldbach, A. Frorip, K. Ibragimov, I. Kuusmann, and C. Luschik. Relaxation of excitons in wide-gap CsCl crystals. *J. Phys.: Condens. Matter*, 6:2357, 1993.
- [166] R. I. Eglitis, A. I. Popov, and E. A. Kotomin. Computer simulation of I-center annealing in KCl and KBr crystals. *Phys. Stat. Sol.*, 190:353, 1995.
- [167] M. Szymoski, J. Koodziej, Z. Postawa, P. Czuba, and P. Piatkowski. Electron-stimulated desorption from ionic crystal surfaces. *Prog. in Surf. Sci.*, 48:83, 1995.
- [168] A. Alexandrov, M. Piacentini, N. Zema, A. C. Felici, and T. M. Orlando. Role of excitons in electron- and photon-stimulated desorption of neutrals from alkali halides. *Phys. Rev. Lett.*, 86:536, 2001.

- [169] C. Bandis, S. C. Langford, and J. T. Dickinson. Desorption of positive ions from ionic crystals accompanying 248 nm laser irradiation. *Appl. Phys. Lett.*, 76:421, 2000.
- [170] V. Puchin, A. Shluger, and N. Itoh. Theoretical studies of atomic emission and defect formation by electronic excitation at the (100) surface of NaCl. *Phys. Rev. B*, 47:10760, 1993.
- [171] T. Kubo, A. Okano, J. Kanasaki, K. Ishikawa, Y. Nakai, and N. Itoh. Emission of Na atoms from undamaged and slightly damaged NaCl (100) surfaces by electronic excitation. *Phys. Rev. B*, 49:4931, 1994.
- [172] C. B. Lushchik and A. C. Lushchik. *Decay of Electronic Excitations with Defect Formation in Solids*. Nauka: Moscow, 1989.
- [173] V. Puchin, A. Shluger, Y. Nakai, and N. Itoh. Theoretical study of Na-atom emission from NaCl (100) surfaces. *Phys. Rev. B*, 49:11364, 1994.
- [174] A. Alexandrov, M. Piacentini, N. Zema, A. Felici, and T. Orlando. Role of excitons in electron- and photon-stimulated desorption of neutrals from alkali halides. *Phys. Rev. Lett.*, 86:536, 2001.
- [175] L. Hudson, N. Tolk, C. Bao, P. Nordlander, D. Russell, and J. Xu. Electron- and photon-stimulated desorption of atomic hydrogen from radiation-modified alkali halide surfaces. *Phys. Rev. B*, 62:10535, 2000.
- [176] K. Beck, A. Joly, and W. Hess. Evidence for a surface exciton in KBr via laser desorption. *Phys. Rev. B*, 63:125423, 2001.
- [177] W. P. Hess, A. G. Joly, D. P. Gerrity, K. M. Beck, P. V. Sushko, and A. L. Shluger. Control of laser desorption using tunable single pulses and pulse pairs. *The Journal of Chemical Physics*, 116:8144, 2002.
- [178] T. Tomiki, T. Miyata, and H. Tsukamoto. Urbach rule for the sodium- and potassium-halides. *Z. Naturforsch.*, 29a:145, 1974.

- [179] W. Hess, A. Joly, D. Gerrity, K. Beck, P. Sushko, and A. Shluger. Selective laser desorption of ionic surfaces: resonant surface excitation of KBr. *J. Chem. Phys.*, 115:9462, 2001.
- [180] A. G. Joly, K. M. Beck, M. Henyk, W. P. Hess, P. V. Sushko, and A. L. Shluger. Surface electronic spectra detected by atomic desorption. *Surf. Sci.*, 544:L683, 2003.
- [181] A. Alexandrov, M. Piacentini, R. G. Tonkyn, M. T. Sieger, N. Zema, and T. M. Orlando. Electron-stimulated desorption of iodine atoms from KI(100): an energy- and temperature-dependent study. *Surf. Sci.*, 451:208, 2000.
- [182] M. Szymonski, J. Kolodziej, B. Such, P. Piatkowski, P. Struski, P. Czuba, and F. Krok. Nano-scale modification of ionic surfaces induced by electronic transitions. *Prog. in Surf. Sci.*, 67:123, 2001.
- [183] J. J. Kolodziej and M. Szymonski. Hot-carrier transport processes in stimulated desorption of alkali halides. *Phys. Rev. B*, 58:13204–13211, 1998.
- [184] J.J. Kolodziej, B. Such, P. Czuba, F. Krok, P. Piatkowski, P. Struski, M. Szymonski, R. Bennowitz, S. Schr, and E. Meyer. Frenkel defect interactions at surfaces of irradiated alkali halides studied by non-contact atomic-force microscopy. *Surf. Sci.*, 482:903, 2001.
- [185] J. J. Kolodziej, B. Such, P. Czuba, F. Krok, P. Piatkowski, P. Struski, M. Szymonski, R. Bennowitz, S. Schaer, and E. Meyer. Frenkel defect interactions at surfaces of irradiated alkali halides studied by non-contact atomic-force microscopy. *Surf. Sci.*, 482:903, 2001.
- [186] J. Kolodziej and M. Szymonski. Hot-carrier transport processes in stimulated desorption of alkali halides. *Phys. Rev. B*, 58:13204, 1998.
- [187] K. Shibuya, H. Saito, M. Koshimizu, and K. Asai. Outstanding timing resolution of pure CsBr scintillators for coincidence measurements of positron annihilation radiation. *Appl. Phys. Ex.*, 3:086401, 2010.

- [188] E. A. Kotomin, V. E. Puchin, and P. W. M. Jacobs. A theoretical study of H-centre migration in alkali halide crystals KCl and NaCl. *Phil. Mag. A*, 68:1359, 1993.
- [189] I. S. Lim, P. Schwerdtfeger, B. Metz, and H. Stoll. All-electron and relativistic pseudopotential studies for the group 1 element polarizabilities from K to element 119. *J. Chem. Phys.*, 122:104103, 2005.
- [190] P. J. Hay and W. R. Wadt. Ab initio effective core potentials for molecular calculations. Potentials for main group elements Na to Bi. *J. Chem. Phys.*, 82:284, 1985.
- [191] P. J. Hay and W. R. Wadt. Ab initio effective core potentials for molecular calculations. Potentials for K to Au including the outermost core orbitals. *J. Chem. Phys.*, 82:299, 1985.
- [192] M. C. C. Wobbe and M. A. Zwijnenburg. Chemical trends in the optical properties of rocksalt nanoparticles. *Phys. Chem. Chem. Phys.*, 17:28892, 2015.
- [193] A. S. Mysovsky, P. Sushko, E. A. Radzhabov, M. Reichling, and A. Shluger. Structure and properties of oxygen centers in CaF₂ crystals from ab initio embedded cluster calculations. *Phys. Rev. B*, 84:064133, 2011.
- [194] R. Poole, J. Jenkin, J. Liesegang, and R. Leckey. Electronic band structure of the alkali halides. I. Experimental parameters. *Phys. Rev. B*, 11:5179, 1975.
- [195] J. Shanker and K. Singh. Analysis of crystal binding and Gruneisen parameter in cesium halides, silver halides, and alkaline earth oxides. *Phys. Stat. Sol. B*, 113:737, 1982.
- [196] J. Shanker and S. Sharma. Evaluation of electronic dielectric constant and fractional ionic character of mixed alkali halide crystals. *Phys. Stat. Sol. B*, 136:505, 1986.
- [197] R. Huffman, J. Larrabee, and Y. Tanaka. New absorption series and ionization potentials of atomic fluorine, bromine, and iodine. *J. Chem. Phys.*, 47:856, 1967.

- [198] C. Blondel, P. Cacciani, C. Delsart, and R. Trainham. High-resolution determination of the electron affinity of fluorine and bromine using crossed ion and laser beams. *Phys. Rev. A*, 40:3698, 1989.
- [199] A. J. Fisher, W. Hayes, and A. M. Stoneham. Theory of the structure of the self-trapped exciton in quartz. *J. Phys.: Condens. Matter*, 2:6707, 1990.
- [200] P. V. Sushko and A. L. Shluger. Exciton-driven highly hyperthermal O-atom desorption from nanostructured CaO. *J. Phys. Chem. C*, 115:692, 2011.
- [201] V. E. Puchin, A. L. Shluger, and N. Itoh. The excitonic mechanism of Na-atom desorption from the (100)NaCl surface. *J. Phys.: Condens. Matter*, 7:L147, 1995.
- [202] K. Teegarden and G. Baldini. Optical absorption spectra of the alkali halides at 10 K. *Phys. Rev.*, 155:896, 1966.
- [203] K. M. Beck, A. G. Joly, N. F. Dupuis, P. Perozzo, W. P. Hess, P. V. Sushko, and A. L. Shluger. Laser control of product electronic state: Desorption from alkali halides. *J. Chem. Phys.*, 120:2456, 2004.
- [204] K. M. Beck, A. G. Joly, O. Diwald, S. Stankic, P. E. Trevisanutto, and P. V. Sushko. Energy and site selectivity in O-atom photodesorption from nanostructured MgO. *Surf. Sci.*, 602:1968, 2008.
- [205] J. VandeVondele, M. Krack, F. Mohamed, M. Parrinello, T. Chassaing, and J. Hutter. Quickstep: Fast and accurate density functional calculations using a mixed Gaussian and plane waves approach. *Comp. Phys. Comms.*, 167:103, 2005.
- [206] S. Goedecker, M. Teter, and J. Hutter. Separable dual-space gaussian pseudopotentials. *Phys. Rev. B*, 54:1703, 1996.
- [207] C. Hartwigsen, S. Goedecker, and J. Hutter. Relativistic separable dual-space gaussian pseudopotentials from H to Rn. *Phys. Rev. B*, 58:3641, 1998.
- [208] M. Krack. Pseudopotentials for H to Kr optimized for gradient-corrected exchange-correlation functionals. *Theor. Chem. Accs.*, 114:145, 2005.

- [209] J. VandeVondele and J. Hutter. Gaussian basis sets for accurate calculations on molecular systems in gas and condensed phases. *J. Chem. Phys.*, 127:114105, 2007.
- [210] U. Gerhardt and E. Dietz. Angular distribution of photoelectrons emitted from copper single crystals. *J. Appl. Phys.*, 26:1477, 1971.
- [211] T. Boutboul, A. Akkerman, A. Breskin, and R. Chechik. Escape length of ultraviolet induced photoelectrons in alkali iodide and CsBr evaporated films: Measurements and modeling. *J. Appl. Phys.*, 84:2890, 1998.
- [212] E. Shefer, A. Breskin, T. Boutboul, R. Chechik, B. K. Singh, H. Cohen, and I. Feldman. Photoelectron transport in CsI and CsBr coating films of alkali antimonide and CsI photocathodes. *J. Appl. Phys.*, 92:4758, 2002.
- [213] J. Franck and G. Hertz. Ueber zusammenstoesse zwischen Elektronen und Molekuelen des Quecksilberdampfes und die Ionisierungsspannung desselben. *Verhand. der Deut. Phys. Gesell.*, 16:457, 1914.
- [214] A. Lushchik, Ch. Lushchik, P. Liblik, A. Maaros, V. N. Makhov, F. Savikhin, and E. Vasil'chenko. Luminescent protection against radiation damage in wide-gap materials. *J. Lumin.*, 129:1894, 2009.
- [215] E. Feldbach, M. Kamada, M. Kirm, A. Lushchik, Ch. Lushchik, and I. Martinson. Direct excitation of Tl impurity ions by hot photoelectrons in wide-band gap crystals. *Phys. Rev. B*, 56:13908, 1997.
- [216] A. Lushchik, M. Kamada, M. Kirm, Ch. Lushchik, and I. Martinson. Direct excitation of impurity centres by hot photoelectrons in ionic crystals. *Rad. Meas.*, 29:229, 1998.
- [217] J. N. Wilson and R. M. Curtis. Dipole polarizabilities of ions in alkali halide crystals. *J. Phys. Chem.*, 74:187, 1970.
- [218] K. P. McKenna and A. L. Shluger. First-principles calculations of defects near a grain boundary in MgO. *Phys. Rev. B*, 79:224116, 2009.

- [219] W. E. Spicer. Photoemissive, photoconductive, and optical absorption studies of alkali-antimony compounds. *Phys. Rev.*, 112:114, 1958.
- [220] P. O. Gartland, S. Berge, and B. J. Slagsvold. Photoelectric work function of a copper single crystal for the (100), (110), (111), and (112) faces. *Phys. Rev. Lett.*, 28:738, 1972.
- [221] D. H. Dowell, I. Bazarov, B. Dunham, K. Harkay, C. Hernandez-Garcia, R. Legg, H. Padmore, T. Rao, J. Smedley, and W. Wan. Eu-doped CsBr phosphor as a new optically-stimulable phosphor material for medical X-ray imaging sensor. *Radiat. Prot. Dosim.*, 119:398, 2010.
- [222] S. Prada, U. Martinez, and G. Pacchioni. Work function changes induced by deposition of ultrathin dielectric films on metals: A theoretical analysis. *Phys. Rev. B*, 78:235423, 2008.
- [223] L. Giordano, F. Cinquini, and G. Pacchioni. Tuning the surface metal work function by deposition of ultrathin oxide films: Density functional calculations. *Phys. Rev. B*, 73:045414, 2006.
- [224] H. Geistlinger, I. Eisele, B. Flietner, and R. Winter. Dipole and charge transfer contributions to the work function change of semiconducting thin films: experiment and theory. *Sens. and Act. B*, 34:499, 1996.
- [225] D. H. Dowell and J. F. Schmerge. Quantum efficiency and thermal emittance of metal photocathodes. *Phys. Rev. Spec. Top. - Acc. and Beams*, 12:074201, 2009.
- [226] A. V. Krukau, O. A. Vydrov, A. F. Izmaylov, and G. E. Scuseria. Influence of the exchange screening parameter on the performance of screened hybrid functionals. *J. Chem. Phys.*, 125:224106, 2006.
- [227] S. V. Aradhya, M. Frei, M. S. Hybertson, and L. Venkataraman. Van der Waals interactions at metal/organic interfaces at the single-molecule level. *Nature Mat.*, 11:872, 2012.

- [228] S. Ehrlich, J. Moellmann, W. Reckien, T. Bredow, and S. Grimme. System-dependent dispersion coefficients for the DFT-D3 treatment of adsorption processes on ionic surfaces. *Chem. Phys. Chem.*, 12:3414, 2011.
- [229] P. L. Silvestrelli and A. Ambrosetti. van der Waals corrected DFT simulation of adsorption processes on transition-metal surfaces: Xe and graphene on Ni(111). *Phys. Rev. B*, 91:195405, 2015.
- [230] F. Zhang, J. D. Gale, B. P. Uberagua, C. R. Stanek, and N. A. Marks. Importance of dispersion in density functional calculations of cesium chloride and its related halides. *Phys. Rev. B*, 88:054112, 2013.
- [231] M. E. Straumanis and L. S. Yu. Lattice parameters, densities, expansion coefficients and perfection of structure of Cu and of Cu-In α phase. *Acta. Cryst.*, A25:676, 1969.
- [232] G. Henkelman, B. P. Uberuaga, and H. Jónsson. A climbing image nudged elastic band method for finding saddle points and minimum energy paths. *J. Chem. Phys.*, 113:9901, 2000.
- [233] G. Henkelman and H. Jónsson. Improved tangent estimate in the nudged elastic band method for finding minimum energy paths and saddle points. *J. Chem. Phys.*, 113:9978, 2000.
- [234] S. Grimme, S. Ehrlich, and L. Goerigk. Effect of the damping function in dispersion corrected density functional theory. *J. Comput. Chem.*, 32:1456, 2011.
- [235] S. Yun, Z. Liu, and P. Pianetta. Surface dipole formation and lowering of the work function by Cs adsorption on InP(100) surface. *J. Vac. Sci. and Tech. A*, 25:1351, 2007.
- [236] J. Lee, C. Lin, and A. A. Demkov. Metal-induced charge transfer, structural distortion, and orbital order in SrTiO₃ thin films. *Phys. Rev. B*, 87:165103, 2013.
- [237] V. N. Ageev, Yu. A. Kuznetsov, and N. D. Potekhina. Electron-stimulated desorption of cesium atoms from cesium layers deposited on a germanium-coated tungsten surface. *Phys. of the Sol. Stat.*, 47:1784, 2005.

- [238] J. L. LaRue, J. D. White, N. H. Nahler, Z. Liu, P. A. Pianetta, D. J. Auerbach, and A. M. Wodtke. The work function of submonolayer cesium-covered gold: A photoelectron spectroscopy study. *J. Chem. Phys.*, 129:024709, 2008.